Universidade Nova de Lisboa
OMNIS CIVITAS CONTRA SE DIVISA NON STABIT
Faculdade de Ciências e Tecnologia

PABLO JAVIER GONZÁLEZ

PERIPLASMIC NITRATE REDUCTASES: STRUCTURAL AND SPECTROSCOPIC STUDIES

LISBOA, 2006

PABLO JAVIER GONZÁLEZ

PERIPLASMIC NITRATE REDUCTASES: STRUCTURAL AND SPECTROSCOPIC STUDIES

DISSERTAÇÃO APRESENTADA PARA A OBTENÇÃO DO GRAU DE DOUTOR EM BIOQUIMICA, ESPECIALIDADE BIOQUIMICA-FISICA, PELA FACULDADE DE CIÊNCIAS E TECNOLOGIA DA UNIVERSIDADE NOVA DE LISBOA.

LISBOA, 2006

- Nº DE ARQUIVO

- COPYRIGHT

…no hay asunto, por complicado que sea, que estudiado con paciencia e inteligencia no se complique aun más…

Anónimo

ACKNOWLEDGEMENTS

I would like to express firstly my gratefulness to Prof. José J.G. Moura, my advisor, for receiving me and accepting me to carry out my PhD work in his research group and for his unconditional support and confidence in the development of the work performed during these four years. I would like to thanks also for his friendship and encouragement to pursue the objectives of this research work.

Prof. Isabel Moura, very special thanks for let me work at your lab and for teaching me all the secrets about protein purification. This work would not have been possible without your support and motivation to face the hard work. The discussions, encouragement and critiques were of essence to the progress of this work.

Prof. Carlos Brondino (El Jefe), it is difficult to emphasize my gratitude taking into account how *bárbaro* you are… you did not introduce me in the field… but you were my mentor-like. I thank your great efforts to explain the things beyond my understanding but more important to study the subjects beyond yours! …that helped to make this to progress. I acknowledge you for guiding me through the course of this thesis work and the writing of the published papers, and for the critiques (constructives and destructives also!) which improve all the work I have made this last years.

Prof. María João Romão, thank you for your help and constant interest with the work developed with the nitrate reductases and for invite me and trust me the work with the Nap from *Ralstonia*.

Many many thanks the people who *"tilt the scale"*: Alberto Rizzi, Laura Felice (*por la paciencia*), Sofia Pauleta, Ana Teresa Lopes, Jorge Dias, Marta Carepo, Pedro Cabrito, Jorge Martinho, Simone Dell'acqua (and Francesca), Ines Cabrito, Teresa SSS, Joana, Cristina Correia, Stephane Besson (Katy, Prisca and Tom), Celia Silveira, Cristiano Mota…I hope did not forgot someone.

I am totally indebted to Maria João Baleizão, who performed the tough work of molecular biology with the *nap* operon of *Desulfovibrio desulfuricans*. All these results, although not conclusive yet, will be very useful for the future work.

I would like to thank Dr. Sergey Bursakov for the help at the starting of this PhD work and the tips for the purification of Nap from *Desulfovibrio desulfuricans*. In this line I would like to thank also Sandro Soares, Ana Sofia Cruz and Angelo.

My special gratitude goes to Roeland Boer, who starts the crystallization of the reacted samples of *Dd* NapA, and obviously to Shabir Najmudin who crystallized, solved the structures reported in this work, and helped me in the writing of the crystallography sections. I would like to thank also Jose Trincão and Catarina Coelho for the collaboration with the Nap from *Ralstonia*.

Many thanks to Mario Passeggi for his friendship and help with "dark side" of the EPR spectroscopy.

Jose Luis Capelo and Carlos Lodeiro, thank you very much for your friendship and for all the help and advices…the time spent in Portugal would have been very different without you.

Thanks the colleagues of *Bioin*, *Bioprot*, and the people from *X-tal*.

Thanks Eng. Lucia, Isabel Rodrigues and Maria Jose Carapinha for all the help with the burocracy.

Thanks Fundação para a Ciência e a Tecnologia (SFRH/BD/10825/2002) for financial support.

Finally, I would like to thank those closest to me; they are very important to me and their presence helped to complete every goal I planned.
My family, *Gonza, Cristy, Malu, Diego y Sergio*, I am grateful for your absolute support and confidence in every moment. My grandmother *Sarita*, thank you for giving me a home in Santa Fe and for being the person you are. *Mabel, Alicia, Florencia, Ale, Marcelo, Ruben y Juan*…you have been there since I remember…
My best best friends *Cano y Nilson*, your unconditional friendship is one of my treasures in this life.

Lastly and more important, I would like to express my gratitude to my beloved wife, Gaby, you give me love, friendship, total support, encouragement and patient companionship since the time of the university.

To all of you, I dedicate this thesis.

RESUMO

A redução do nitrato é um processo levado a cabo nas células com o objectivo de incorporar azoto em biomoléculas (amonificação asimilatoria), consumir os equivalentes de redução no crescimento anaeróbio das bactérias (desnitrificação/ amonificação disimilatoria), e/ou eliminar o excesso de energia produto do metabolismo duma determinada fonte de carbono (amonificação disimilatoria). As redutases do nitrato são enzimas que catalisam a conversão do nitrato ao nitrito. Estas enzimas são proteínas que contem um centro mononuclear de molibdénio e outros cofactores redox tais como centros ferro-enxofre e hemos do tipo *b* ou *c*, que medeiam a transferência de electrões desde o doador até o nitrato. As redutases do nitrato foram classificadas em quatro grupos: (1) redutases do nitrato de eucariontes (Euk-NR), (2) redutases do nitrato asimilatorias (Nas), (3) redutases do nitrato respiratórias (Nar), (4) redutases do nitrato periplasmáticas (Nap). As redutases do nitrato periplasmáticas isoladas de *Desulfovibrio desulfuricans* (*Dd*), *Paracoccus pantotrophus* (*Pp*) e *Rhodobacter sphaeroides* (*Rs*) constituem as Nap melhor estudadas na actualidade. A estrutura cristalográfica da Nap de *Dd* em condições aeróbias foi a primeira estrutura publicada destas enzimas. O sítio activo no estado oxidado está formado pelo ion de molibdénio (Mo^{6+}) hexacoordenado aos quatro átomos de enxofre dos dois cofactores pterínicos, o enxofre gamma da Cys_{140}, e um Hidroxilo/Agua na sexta posição de coordenação.

Nesta tese são reportados estudos realizados nas redutases do nitrato periplasmáticas isoladas a partir das bactérias *Desulfovibrio desulfuricans* ATCC 27774 e *Cupriavidus necator* H16. Ambas enzimas foram purificadas até homogeneidade electroforética.

A Nap purificada a partir de células de *D. desulfuricans* ATCC 27774 crescidas em anaerobiose e em presença de nitrato foi isolada como uma proteína monómerica solúvel de ~80 kDa. Estudos cinéticos indicam que, a diferença com as Naps diméricas, esta enzima possui promiscuidade pelo substrato devido a que pode reduzir não só o nitrato como também outros aniões de estrutura similar. As titulações redox monitorizados por espectroscopia de EPR realizadas na ausência e presença do nitrato na escala de +200 a -500 mV (*vs*. NHE), e os estudos de EPR da enzima em condições catalíticas ou em presença de inibidores, revelam diversas espécies de Mo(V) activas no EPR, o que sugere que o sitio activo possui uma importante flexibilidade de coordenação. Estes estudos demonstram também que o substrato modula as propriedades redox do Mo mas não o do centro ferro-enxofre.

A Nap purificada a partir de celúlas de *Cn* H16 crescidas em aerobiose na ausência de nitrato foi isolada como uma proteína heterodimérica solúvel com subunidades grande e pequena de ~90 e ~15 kDa, respectivamente. Estudos preliminares são reportados para esta proteina. As propriedades bioquímicas, estruturais e espectroscópicas de ambas enzimas são discutidas em comparação com outras proteínas relacionadas.

ABSTRACT

Nitrate reduction occurs in the cell in order to incorporate nitrogen into biomolecules (assimilatory ammonification), as the final electron acceptor when bacteria are grown in anaerobic conditions (denitrification/dissimilatory ammonification) and to eliminate energy excess generated by the cell metabolism (dissimilatory ammonification). Nitrate reductases are enzimes that catalize the conversion of nitrate to nitrite. Most nitrate reductases are mononuclear molybdenum-containing enzymes that have, besides the Mo-pterin cofactor, additional metallic centers such as iron-sulfur clusters and *b*- or *c*-type hemes that mediate electron transfer reactions between the electron donor and the nitrate. Nitrate reductases have been classified into four groups: (1) eukaryotic nitrate reductases (Euk-NR), (2) assimilatory nitrate reductases (Nas), (3) respiratory nitrate reductases (Nar) and (4) periplasmic nitrate reductases (Nap). Naps isolated from *Desulfovibrio desulfuricans* (*Dd*), *Paracoccus pantotrophus* (*Pp*) and *Rhodobacter sphaeroides* (*Rs*) constitute the best-characterized Naps, so far. The 3D X-ray structure of *Dd* NapA in its oxidized form was the first reported structure for these enzymes. The active site in the oxidized state is made up by a distorted Mo^{6+} ion hexacoordinated by four sulfurs from the two pterin cofactors, the γ-sulfur from a cysteine (Cys_{140}), and a hydroxo/water ligand.

This thesis deals with the study of the nitrate reductases isolated from *Desulfovibrio desulfuricans* ATCC 27774 and *Cupriavidus necator* H16. Both enzymes were purified up to electrophoretic homogeinity.

Nap purified from *D. desulfuricans* ATCC 27774 cells grown in anaerobeosis and in the presence of nitrate was isolated as a soluble monomeric protein of ~80 kDa. Kinetic studies show that, in contrast to dimeric Naps, this enzyme presents substrate promiscuity since it is able to reduce not only nitrate but also other anions of similar structure. EPR-monitored redox titrations, carried out with and without nitrate in the potential range from 200 to -500 mV (*vs*. NHE), and EPR studies in both catalytic and inhibiting conditions, reveal distinct types of Mo(V) EPR-active species, which indicates that the Mo site shows a high coordination flexibility. These studies show that nitrate modulates the redox properties of the active site, but not those of the iron-sulfur cluster.

Nap purified from *Cn* H16 cells grown in aerobic conditions in the absence of nitrate was isolated as a soluble heterodimeric protein with large and small subunits of ~90 and ~15 kDa, respectively. Preliminary results are reported for this protein. The biochemical,

structural, and spectroscopic properties of both enzymes are discussed in comparison with those of other closely related proteins.

ABBREVIATIONS

A	value of the hyperfine coupling
Å	Angstrom
A_{av}	average of the mean A-values
AMP	adenosine monophosphate
ANAMOX	anaerobic ammonium oxidation
APS	adenylyl-phospho sulfate
APSr	APS reductase
ATCC	American Type Culture Collection
ATP	adenosine triphosphate
ATPs	ATP sulfurylase
B.	*Bradyrhizobium*
C.	*Cupriavidus*
ccNir/NrfAH	multihemic nitrite reductase
Cn	*Cupriavidus necator*
Cu-Nir	cooper-containing nitrite reductase
Cyt cd_1	Cytochrome cd_1 nitrite reductase
D	axial distortion of the ZFS
D.	*Desulfovibrio*
Dd	*Desulfovibrio desulfuricans*
DEAE	diethyl-aminoethyl
DFT	density functional theory
Dg	*Desulfovibrio gigas*
DMSO	dimethylsulfoxide
Dsr	dissimilatory sulfite reductase
E	rhombic distortion of the ZFS
E.	*Escherichia*
Ec	*Escherichia coli*
E_{cat}	midpoint redox potential of the catalytic current
EDTA	ethylenediamine tetra-acetic acid
E^o	standard midpoint redox potential
EPR	electron paramagnetic resonance
Euk-NR	eukaryotic nitrate reductase
EXAFS	extended X-ray absorption fine structure
Fdh	formate dehydrogenase
Fdh-H	Fdh of the formate-hydrogen lyase complex
Fdh-N	membrane anchored Fdh induced by nitrate
g	g-factor
G	Gauss
g_{av}	average of the mean g-values
GOGAT	glutamine-oxoglutarate aminotransferase
GS	glutamine synthase
I	nuclear spin
K	kelvin
K.	*Klebsiella*
MAD	multi-wavelength anomalous dispersion
MCD	molybdopterin cytosine dinucleotide
MES	morpholine-ethano-sulphonic acid
MGD	molybdopterin guanosine dinucleotide
MQH_2	menaquinone
mV	millivolts
MV	methyl viologen

N_2	dinitrogen
N_2H_4	hydrazine
N_2O	nitrous oxide
Nap	periplasmic nitrate reductase
Nar	respiratory nitrate reductase
Nas	assimilatory nitrate reductase
NH_2OH	hydroxilamine
NH_4^+	ammonium
NHE	normal hydrogen electrode
NirB	NADH-dependent nitrite reductase
NO	nitric oxide
NO_2^-	nitrite
NO_3^-	nitrate
NR	nitrate reductase
P.	*Paracoccus*
PAPS	phospho-adenylyl-phospho sulfate
PEG	polyethyleneglycol
PMF	proton motive force
Pn	*Pseudomonas nautica*
Pp	*Paracoccus pantotrophus*
QH_2	quinone
R.	*Rhodobacter*
RMSD	root-mean square deviation
Rs	*Rhodobacter sphaeroides*
S	total spin
S^{2-}	sulfide
$S_2O_3^{2-}$	thiosulfate
SAD	single-wavelength anomalous dispersion
S_n	elemental sulfur
SO	sulfite oxidase
SO_3^{2-}	sulfite
SO_4^{2-}	sulfate
SOR	sulfur oxigenase-reductase
Sox	multienzymatic sulfur oxidizing system
SRB	sulfate-reducing bacteria
UQH_2	ubiquinone
v	rhombic distortion
W.	*Wolinella*
ZFS	zero field splitting
Δ	axial distortion
ε	UV-Vis extinction coefficient

TABLE OF CONTENTS

FIGURES INDEX

INTRODUCTION

I.1 Molybdenum in nature

Molybdenum (Mo, element 42) is a transition metal belonging to the group 6 of the periodic table of the elements located at the 5th period. Molybdenum does not occur free in nature and is usually found in molybdenite (MoS_2) and wulfenite ($PbMoO_4$) ores or recovered as a by-product of copper and tungsten mining. Molybdenum has seven naturally occurring isotopes, which are listed in table I.1 together with their respective abundances and nuclear spins. As shown in this table, only the isotopes ^{95}Mo and ^{97}Mo have non-zero nuclear spins.

Table I.1: naturally occurring isotopes of Mo together with their atomic masses, natural abundances, nuclear spins, and magnetic moments.

Isotope	Atomic mass (m_a/u)	Natural abundance (atom %)	Nuclear spin (I)	Magnetic moment (μ/μ_N)
^{92}Mo	91,9068090	14.84	0	
^{94}Mo	93,9050853	9.25	0	
^{95}Mo	94,9058411	15.92	5/2	-0.9142
^{96}Mo	95,9046785	16.68	0	
^{97}Mo	96,9060205	9.55	5/2	-0.9335
^{98}Mo	97,9054073	24.13	0	
^{100}Mo	99,9074770	9.63	0	

Molybdenum is relevant in biology because of its presence in the active site of a wide number of enzymes with key roles in the metabolism of both organic and inorganic compounds [1, 2]. The best characterized examples of Mo-containing proteins correspond to the enzyme nitrogenase [3], CO dehydrogenase [4] and several enzymes which have been grouped in the big family of the mononuclear Mo-enzymes [1, 2].

Molybdenum is present in the active site of the nitrogenase as part of a complex heterometalic cluster (Figure I.1, bottom). In the case of the mononuclear enzymes, Mo is bonded to one or two pyranopterin molecules and to a variable number of ligands such as oxygens (oxo, hydroxo, water, serine, and aspartate), sulfur (sulfido and cysteine) and selenium (selenocysteine) atoms (Figure I.1).

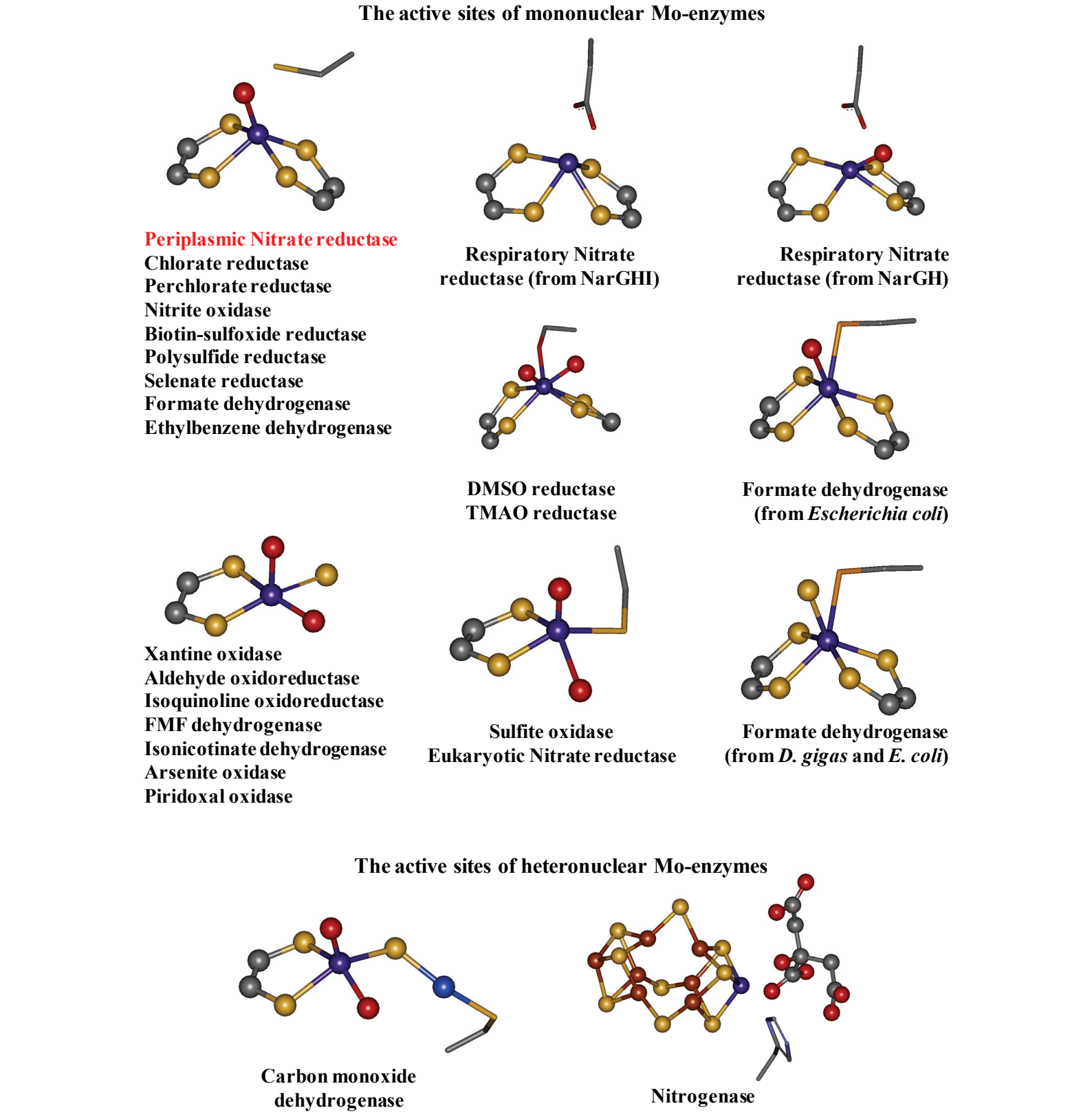

Figure I.1: The active sites of Mo-containing enzymes. Heteroatoms are depicted as balls and aminoacid sidechains as stick. Element color code: grey: carbon, red: oxygen, blue: nitrogen, yellow: sulfur, orange: selenium, violet: molybdenum, cyan: copper, brown: iron. FMF stands for Formylmethanofuran.

The pyranopterin molecule is an organic ligand that can be either in the monophosphate form (R=H) or with a nucleotide molecule attached by a pyrophosphate link (Figure I.2). This type of Mo-site is also present in CO dehydrogenase but, in addition, the Mo is bound to a Cu ion via a sulfur bridge (Figure I.1, bottom). There are other examples of proteins containing Mo included in heterometalic cluster whose role and structures has not been established yet.

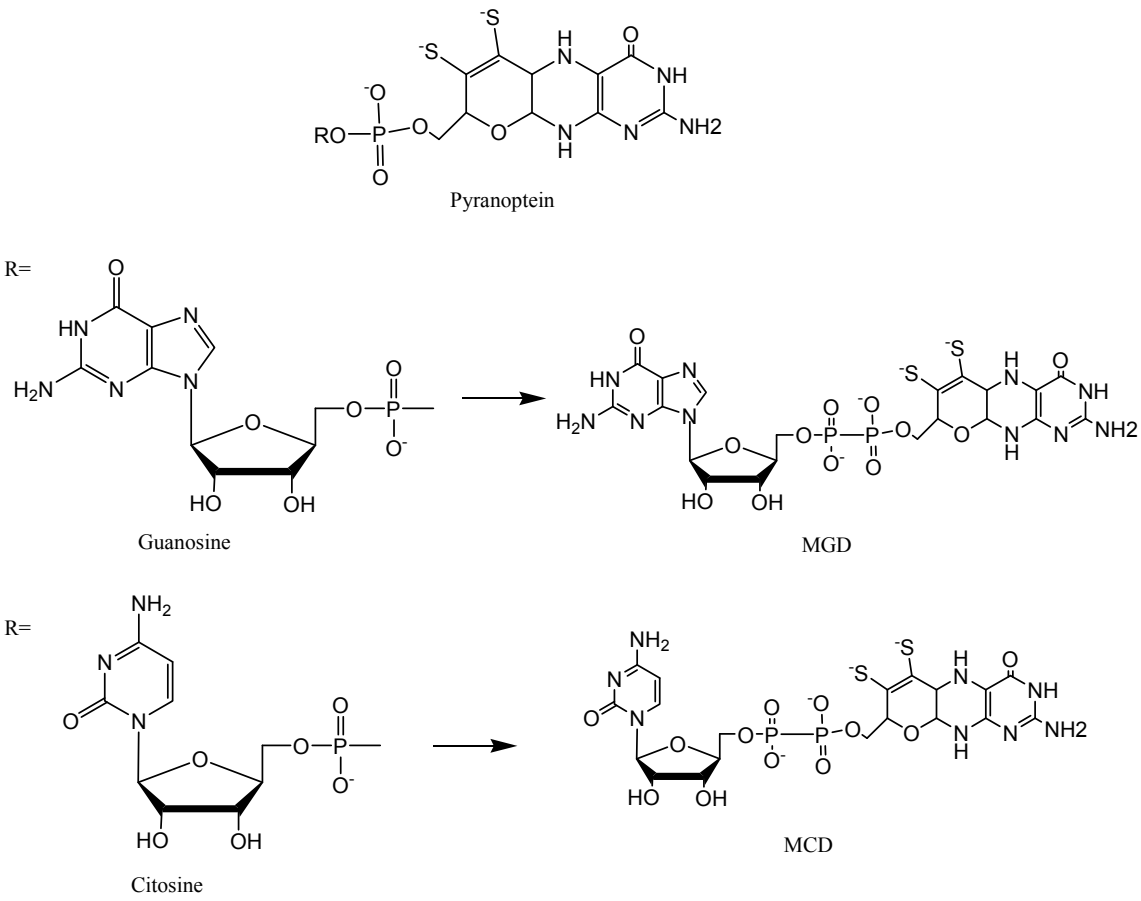

Figure I.2: The pterin cofactor present in mononuclear Mo-containing enzymes and CO dehydrogenase. The pyranopterin molecule (upper) can attach either a guanosine (middle) or a cytosine (lower) nucleoside via a pyrophosphate link. Adapted from reference [5].

All the Mo-containing enzymes shown in Figure I.1 catalyze a huge variety of both oxidative and reductive reactions which are crucial in many biological processes occurring in nature such as the nitrogen, sulfur and carbon metabolisms. Most of these reactions are catalyzed by mononuclear Mo-enzymes. With a few exceptions, these enzymes catalyze the transfer of an oxygen atom from water to the substrate (or *vice versa*) in reactions that imply a

net exchange of two electrons between the enzyme and the substrate and in which the metal ion cycles between the redox states +4 and +6 (Figure I.3).

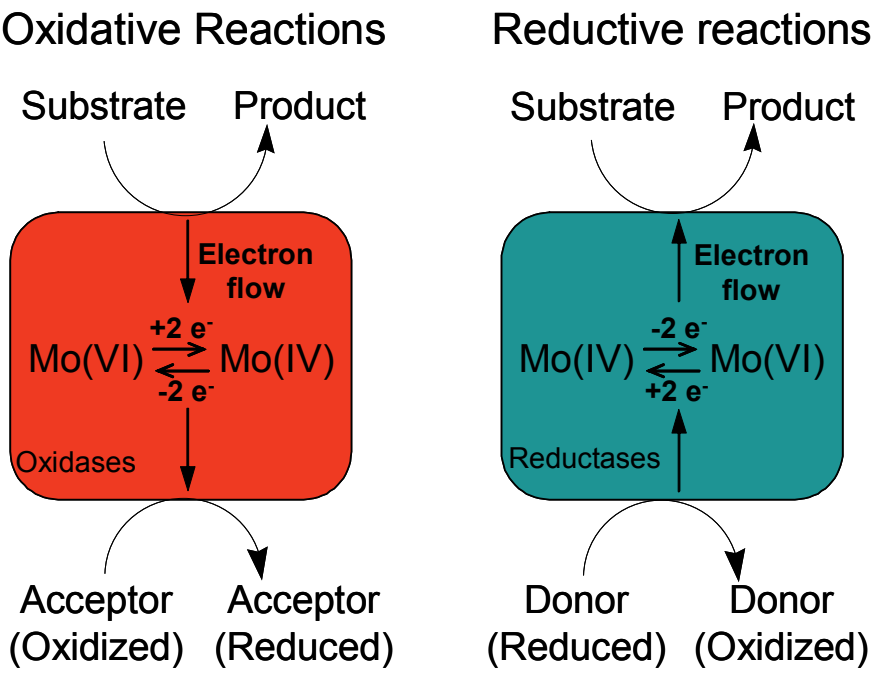

Figure I.3: General mechanism for oxidative (left) and reductive (right) reactions catalyzed by mononuclear Mo-containing enzymes. Adapted from reference [5].

This work will be devoted to the study of the mononuclear Mo-containing enzyme nitrate reductase isolated from the periplasm of *Desulfovibrio desulfuricans* ATCC 27774 and *Cupriavidus necator* H16. *Desulfovibrio desulfuricans* is a sulfate reducing bacterium that produces a periplasmic nitrate reductase when grown in denitrifying conditions. *Cupriavidus necator* is a chemolithotrophic facultative bacterium that produces a periplasmic nitrate reductase when aerobic cultures reach the late death-phase of growth. In the following pages, it will be discussed briefly the main metabolic routes in which these enzymes participate, the molecular and structural properties of the best characterized nitrate reductases, including the current knowledge on molecular biology aspects which are essential to understand their specific function in the cell. Since one of the NRs studied here belong to a sulfate reducing organism, the biogeochemical cycle of the sulfur is also outlined despite this enzyme is not directly involved in this cycle. Furthermore, as an important part of this work is pointed to the

characterization of the Mo ion and 4Fe-4S cluster by EPR spectroscopy, it is briefly analyzed the electronic configuration of both metallic centers in the relevant redox states necessary to understand this work.

I.2 The N-cycle

Nitrogen is a vital component of essential biomolecules such as proteins and nucleic acids. In the biosphere, nitrogen cycles between the oxidation states +V and –III producing many species that constitute the biogeochemical cycle of nitrogen (N-cycle). This cycle involves a number of redox reactions in which prokaryotes play the main role since only they have the enzymes carrying out these processes [6].

The N-cycle involves a number of redox processes, which are shown schematically in Figure I.4. These processes are completely independent in some cases but share some steps in others.

The dissimilatory processes involve the conversion of nitrate into N_2 (respiration/denitrification) or into ammonia (respiration/ammonification) [6-10]. Denitrification is performed by a group of enzymes used by the cell to generate the proton motive force (PMF) across the cytoplasmic membrane [11]. Dissimilatory ammonification is also started with the reduction of nitrate to nitrite, but then nitrite is reduced to ammonia. Both denitrification and dissimilatory ammonification are energy conserving and can be used as an electron sink, *i.e.*, to remove the excess of reducing power in the cell. In addition, ammonification may play an important role in cell detoxification.

The assimilatory process, which also involves the conversion of nitrate to ammonia, starts with the reduction of nitrate in the cytoplasm and is used by the cell to incorporate nitrogen into biomolecules [6, 10, 12-14]. The process called nitrification is the only one that involves oxidative reactions, and is attributed exclusively to bacteria from the *Nitrosomonas* and *Nitrobacter* genus [15, 16].

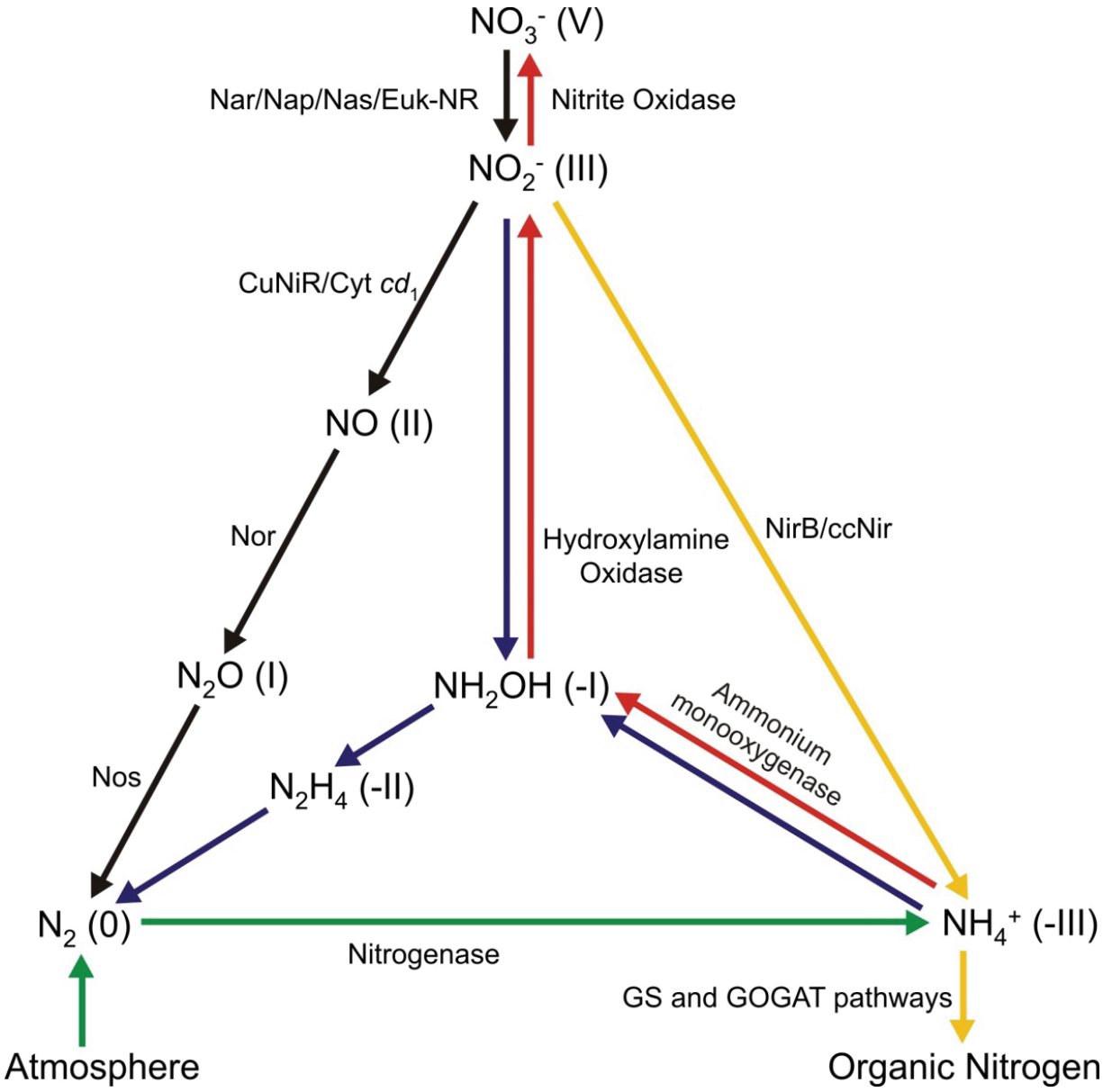

Figure I.4: The inorganic nitrogen cycle including the enzymes responsible for each step. The oxidation state of each compound is indicated between parentheses. The pathways are identified as follow: black arrows, respiratory pathway (denitrification); yellow arrows, dissimilatory and assimilatory ammonification (note that nitrate reduction is indicated only as black arrow); green arrow, nitrogen fixation; red arrows, nitrification; blue arrows, ANAMOX. Adapted from reference [17].

The N-cycle is completed with nitrogen fixation, in which the enzyme nitrogenase reduces nitrogen from both the atmosphere and denitrification to ammonia [14]. A fifth less characterized process named ANAMOX (anaerobic ammonium oxidation), which involves

both oxidative and reductive reactions, is used for bacteria to grow in chemolithoautotrophic conditions (*i.e.* organisms that use carbon dioxide from the environment as carbon source for metabolic processes and use inorganic compounds such as nitrogen, iron, or sulfur for the energy to power these processes) using ammonia as electron donor and nitrite as electron acceptor [6, 18, 19].

I.3 The sulfur metabolism in SRB: the *Desulfovibrio* genus

The Sulfur, an essential component of life, is a ubiquitous element of the earth that cycles between the +VI and -II oxidation states, and is mostly present as elemental sulfur, sulfide and sulfate salts. The various inorganic and organic states of the sulfur in nature constitute the biogeochemical sulfur cycle (S-cycle). This cycle includes reductive and oxidative reactions, which are mainly carried out by microorganisms of archaea and bacteria, and much less by eukaryotes. A simplified version of the S-cycle is schematized in Figure I.5.

The oxidative reactions of sulfur are carried out by microorganisms such as *Acidianus*, *Paracoccus*, *Thiobacillus*, green and purple sulfur bacteria, among others [20]. These microorganisms use the reduced sulfur species (sulfide, elemental sulfur, thiosulfate) to gain electrons for energetic purposes and produce sulfate as the major final product. These reactions are catalyzed by a huge variety of enzymes. For example, the thermo- and acidophilic archaeon *Acidianus ambivalens* [21], can metabolize elemental sulfur in a reaction catalyzed by the sulfur oxygenase-reductase (SOR), leading to its disproportionation to sulfide, sulfite and thiosulfate (Figure I.5, yellow arrows). Thiosulfate can be further oxidized to sulfate by the multienzymatic system called Sox (Figure I.5, red arrow), an enzyme that was already isolated from microorganisms such as *Paracoccus pantotrophus*, green, and purple sulfur bacteria [20].

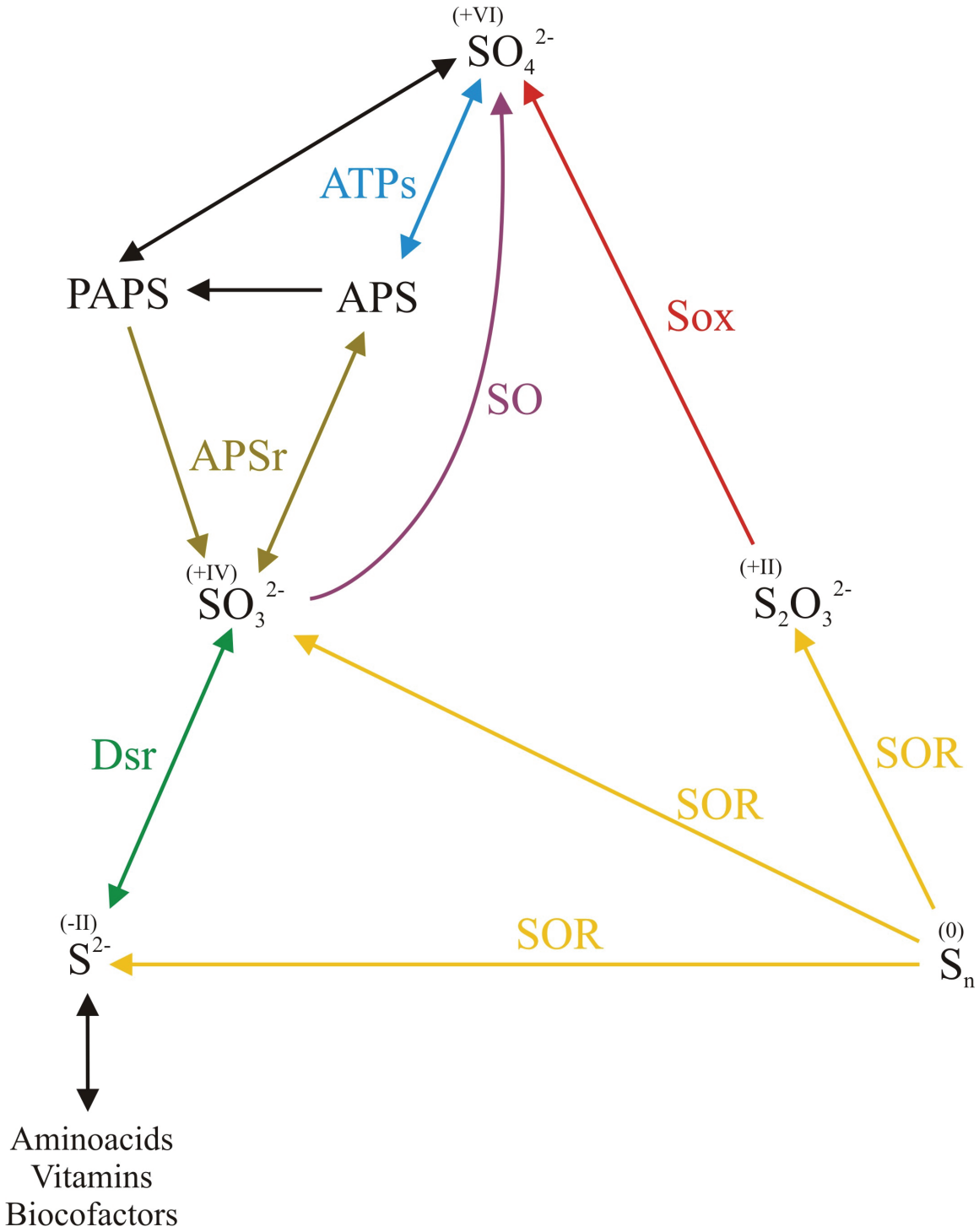

Figure I.5: Simplified biogeochemical S-cycle, including the enzymes responsible for each step. The oxidation state of each compound is indicated between parentheses. The pathways are identified as follow: yellow arrows, elemental sulfur disproportionation; red arrow, thiosulfate oxidation; purple arrow, sulfite oxidation; blue, brown and green arrows, sulfate-reducing and sulfide-oxidizing pathways. There are many other sulfur species that comprise the cycle of sulfur which were omitted for simplicity.

Another oxidative reaction is carried out by the sulfite oxidase (SO) [22]. This is a molybdenum- and heme-containing enzyme belonging to the mononuclear Mo-enzymes (Figure I.2) that catalyzes the oxidation of sulfite to sulfate (Figure I.5, purple arrow). In mammals, this is the terminal step in the oxidative degradation of cysteine, methionine, and membrane components such as sulfatides. Deficiency of this enzyme in humans leads to the accumulation of sulfite producing major neurological abnormalities and early death [23]. Bacterial sulfite oxidases have been purified from *Thiobacillus*, *Starkeya novella*, among others and the main difference with respect to the eukaryotic enzymes is that they lack the heme cofactor [24]. Direct oxidation of sulfite to sulfate occurs in various photo- and chemotrophic sulfur oxidizing microorganisms as the final step in the oxidation of reduced sulfur compounds to obtain reducing equivalents for energetic balance [25].

The reductive pathway (reduction of sulfate to sulfide) is carried out by the sulfate reducing bacteria, yeasts and green plants. They can use sulfate as sulfur source (assimilatory process) to synthesize amino acids, vitamins, and cofactors, among others. Furthermore, sulfate reducing bacteria of genus such as *Desulfobacter*, *Desulfotomaculum* and *Desulfovibrio* utilize sulfate as the acceptor of the reducing equivalents generated during metabolism. This means that sulfate is used as an oxidizing agent for the dissimilation of the organic matter (dissimilatory process), as oxygen does in aerobic organisms during the respiration process.

As sulfate is a molecule with low reactivity, the first step of the dissimilatory sulfate reduction is the activation of the sulfate anion by ATP in a reaction catalyzed by the ATP sulfurylase (ATPs, Figure I.5, blue arrow). The product of this reaction is the Adenylyl-Phospho-Sulfate (APS), which is the substrate of the APS reductase (APSr), which catalyzes the two-electron reduction of APS to sulfite and releasing AMP. In the assimilatory process, the bi-phosphorilated form, Phospho-Adenylyl-Phospho-Sulfate (PAPS), is formed instead of APS, which is the substrate of an APS reductase as well (brown arrows). The sulfite thus

produced is directly reduced to sulfide in a six-electron reaction catalyzed by the dissimilatory sulfite reductase (Dsr - Desulfoviridin, Desulforubidin, Desulfofuscidin and P-582 - green arrows). Dsr can also produce trithionate and thiosulfate; however, the production of these intermediates is an irreversible process and may not ocurr in intact cells. In contrast, the assimilatory sulfite reductases do not produce these free intermediates [26].

ATPs, APSr and Dsr can catalyze also the inverse reactions, and are used by chemolithotrophic aerobic bacteria to oxidize sulfide to sulfate.

The best characterized sulfate reducing bacteria belong to the *Desulfovibrio* genus [27]. About 60 *Desulfovibrio* species have been identified and the genomes of *D. vulgaris* Hildenborough and *D. desulfuricans* G20 (to be reclassified as *D. alaskensis*) have been already annotated [28, 29]. All the strains of the *Desulfovibrio* genus are gram negative bacteria that grow under anaerobic conditions using lactate, pyruvate and/or formate as carbon source. As explained above, the reducing equivalents produced during the metabolism of carbon sources are transferred to the electron acceptors using the Cobalt/Zinc-containing ATPs [30], the heterodimeric APSr that contains a Flavin and two 4Fe-4S cofactors [31], and the tetrameric Dsr (dimer of dimers - Desulfoviridin), which holds a FAD and two sirohemic cofactors [32].

I.4 The nitrogen metabolism in *D. desulfuricans* ATCC 27774 and *C. necator* H16

Formerly, *Desulfovibrio* species and SRB in general were assumed to be microorganisms using only a limited spectrum of organic substrates, in which sulphate is used as terminal electron acceptor. Currently, SRB appear to be the microorganisms that reduce the largest number of electron acceptors, including inorganic sulfur compounds and various other organic and inorganic compounds like nitrate and nitrite [33-35]. Specifically, *Desulfovibrio desulfuricans* ATCC 27774 can grow using nitrate/nitrite as the electron acceptors under anaerobic conditions. The dissimilatory reduction of nitrate and nitrite (called dissimilatory

ammonification) can function as the sole energy-conserving process in a few *Desulfovibrio* species such as *D. desulfuricans*, *D. furfuralis*, *D. profundus*, *D. oxamicus*, *D. simplex*, *D. multispirans* and *D. termitidis* [34, 36-43]. A dissimilatory nitrate reduction has been also reported more recently with *Desulfotomaculum thermobenzoicum* [44], *Desulfobacterium catecholicum* [45], *Desulforhopalus singaporenssi* [46], *Thermodesulfovibrio islandicus* [47], *Thermodesulfobium narugense* [48] and *Desulfobulbus propionicus* [45]. Dissimilatory nitrite reduction by SRB is widespread, but strains capable of nitrate ammonification are far less common [40, 41].

Desulfovibrio desulfuricans subsp. desulfuricans ATCC 27774 (DSM 6949) is the best studied ammonifying strain of a sulfate reducer from a physiological and a biochemical point of view. The growth yield of *D. desulfuricans* ATCC 27774 grown in lactate/nitrate medium is higher when compared with cultures where sulfate is the terminal electron acceptor [33]. The free energy change *per* hydrogen oxidized is about four times higher with nitrate than with sulfate. *Desulfovibrio desulfuricans* ATCC 27774 is also active in the bidirectional transformation of aromatic aldehydes (such as benzaldehyde, 3-hydroxybenzaldehyde) under nitrate-respiring conditions and the direction of transformation (*i.e.* oxidation or reduction) is mainly regulated by reductant availability [49].

In *D. desulfuricans* ATCC 27774, nitrate reduction is carried out exclusively by the soluble enzyme periplasmic nitrate reductase (NapA). The reduction of nitrite to ammonia is carried out by the multihemic cytochrome *c* Nir (NrfAH) which is a heterodimeric membrane-bound enzyme. These processes would be coupled to the translocation of protons to the periplasm, generating an electrochemical gradient for the synthesis of ATP.

In *Cupriavidus necator* H16, three types of prokaryotic nitrate reductases were found (Nas, Nar and Nap), which are expressed under different culture conditions. Nas is expressed in the presence of nitrate independently of the presence of oxygen, and is repressed when the intracellular ammonia level is high, which is in agreement with its assimilative role. However,

expression of Nar is induced in the presence of nitrate under strict anaerobic conditions. The enzymes Cu-Nir, Nor and Nos, needed to complete the denitrification pathway (see Figure I.4), are also expressed under this conditions. Unexpectedly, Nap expression is not directly linked to the nitrogen metabolism since Nar defective mutants of *Cn* H16 are unable to grow under denitrifying conditions. Nap activity is detected when *Cn* H16 cells cultured in aerobic conditions reach stationary phase of growth, and is maximally accumulated in the late death phase [50]. Maximal expression of Nap, as judged by the purification yield, is achieved when cultures are carried out in chemolithotrophic conditions, using fructose and ammonia as carbon and nitrogen sources, respectively. This indicates that the role of *Cn* Nap is different to that attributed to the *Dd* NapA as explained in the next paragraphs.

I.5 Nitrate reductases: classification and structural properties

All the reductive branches of the N-cycle involve the conversion of nitrate to nitrite. This step is performed by distinct enzymes that catalyze the unique reaction

$$NO_3^- + 2\,H^+ + 2e^- \rightarrow NO_2^- + H_2O \qquad E^o = 420\ mV\ vs.\ NHE$$

Nitrate reductases (EC 1.7.99.4) have been classified by taking into consideration source, localization of the enzyme in the cell, molecular properties of the catalytic center, and function. Several nitrate reductases have been obtained from both prokaryotic and eukaryotic organisms.

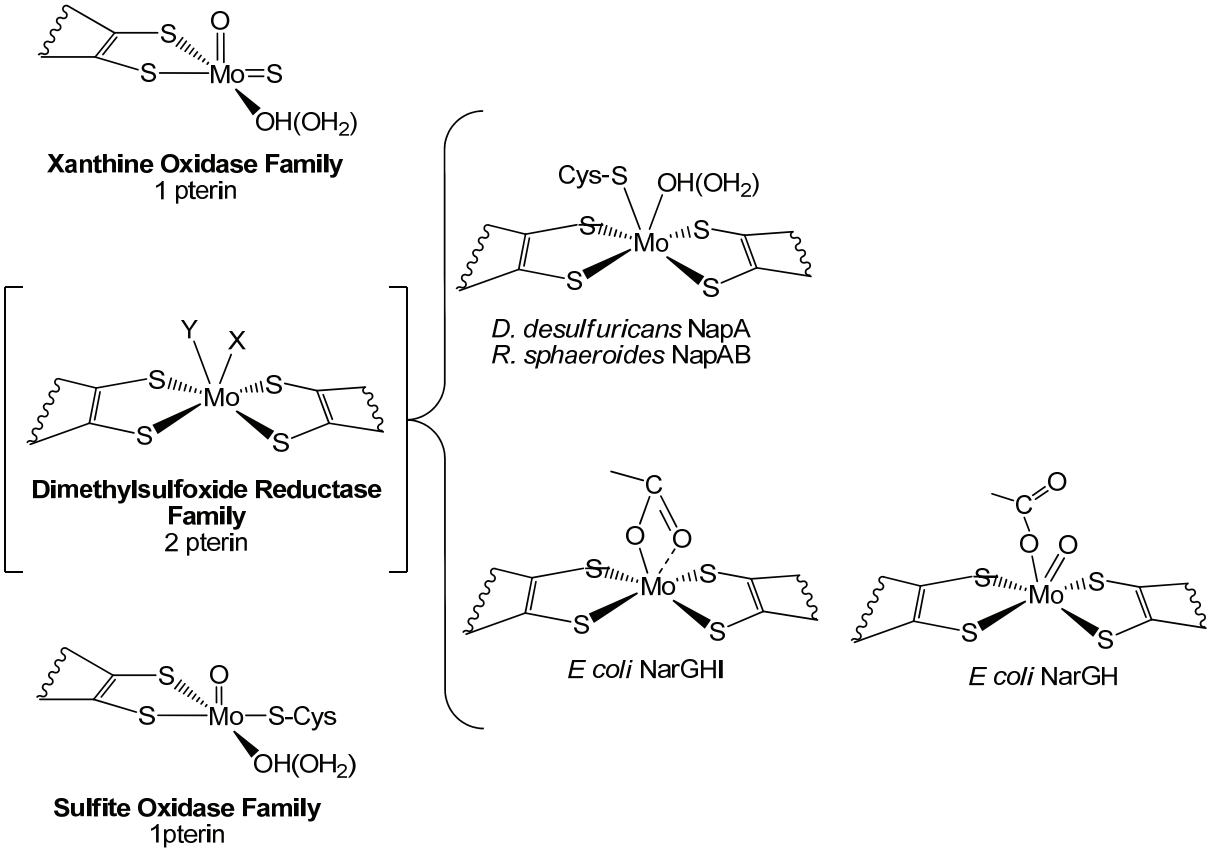

Figure I.6: Left: Active site structure of the three families of mononuclear of mononuclear Mo-containing enzymes. Right: active site structure of the periplasmic *Dd* NapA and *Rs* NapAB enzymes, and membrane-bound *Ec* NarGH and *Ec* NarGHI. X and Y represent ligands such as oxygen (oxo, hydroxo, water, serine, aspartate), sulfur (cysteine) and selenium (selenocysteine) found in the several enzymes of the dimethylsulfoxide reductase family. Reproduced from reference [17].

All of them are mononuclear Mo-containing enzymes that, according to the Hille´s classification [1], belong to the dimethyl sulfoxide (DMSO) reductase family with the only exception being eukaryotic nitrate reductases, which belong to the sulfite oxidase (SO) family (Figure I.6). The prokaryotic enzymes can be also sub-grouped as respiratory nitrate reductase (Nar), periplasmic nitrate reductases (Nap) and assimilatory nitrate reductases (Nas) [51]. Their characterization has allowed gaining considerable information on the molecular basis of nitrate reduction involved in all the branches of the N-cycle.

I.5.1 Respiratory Nitrate Reductases (Nar)

I.5.1.1 Molecular and spectroscopic properties. The Nar enzyme has been isolated from many nitrate-respiring and denitrifying bacteria [52-58]. All the Nars isolated so far are heterotrimeric enzymes composed of the subunits NarG (112-140 kDa), NarH (52-64 kDa) and NarI (19-25 KDa). NarG and NarH are placed in the cytoplasm anchored to the membrane through NarI (Figure I.7). The crystal structures of the oxidized forms of NarGH [59] and NarGHI [60] were reported at resolutions of 2.0 Å and 1.9 Å, respectively. NarGHI has a flower-like arrangement with dimensions of 90×128×70 $Å^3$. The NarI subunit, which is completely immersed in the membrane, is associated with the NarGH dimer through a hydrophobic patch present in NarH. The global arrangement of the catalytic subunit NarG is similar to those from other enzymes belonging to the DMSO reductase family [61], having four domains with α/β type folding. In this sense, it presents high homology with *Dd* Nap, *Ec* Fdh-N, *Ec* Fdh-H and *Dg* Fdh [59-61]. As shown in Figure I.7, NarG contains the active site, a Mo-*bis*MGD cofactor, and an iron-sulfur center of the [4Fe-4S] type (FS0). NarH contains one [3Fe-4S] (FeS4) and three [4Fe-4S] clusters (FeS1-3), whereas NarI contains two *b*-type hemes responsible for the QH_2 oxidation and proton translocation. These eight redox centers are separated by 12-14 Å giving an electron transfer pathway of about 90 Å.

Furthermore, all these metal cofactors are present in all the Nars isolated so far with the only exception of the membrane bound Nar from *Pseudomonas nautica* 617 (*Pn* NarGHI), in which biochemical studies suggest that one of the haems *b* of the NarI subunit is replaced by a *c*-type heme (Correia et al., *to be published*).

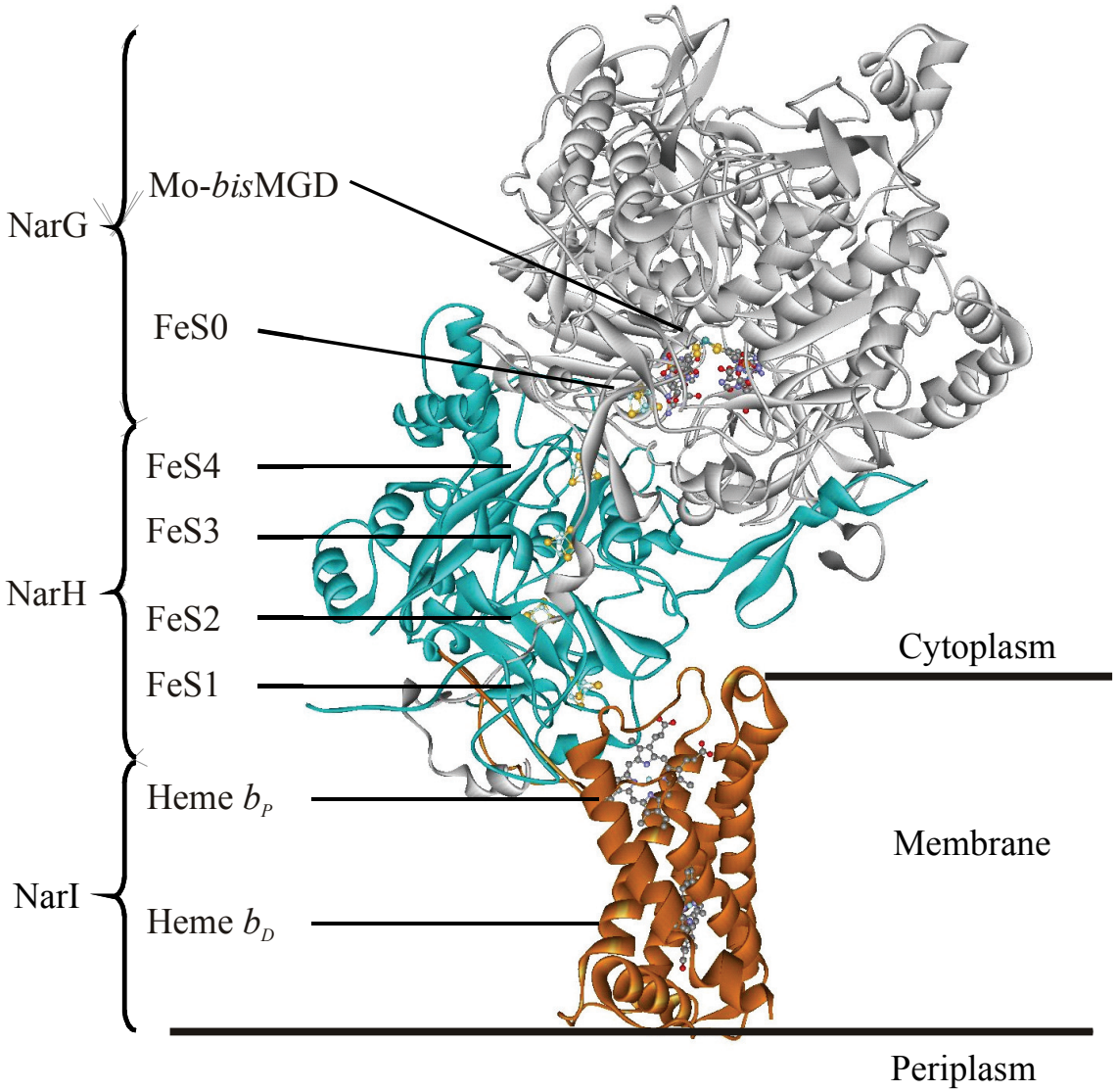

Figure I.7: Overall three-dimensional structure of NarGHI from *E. coli* K12. The names of the respective subunits together with the metal cofactors are indicated. Reproduced from reference [17].

The structure of NarGHI reveals that the active site is composed of a molybdenum atom coordinated to four sulfur atoms from two pterin cofactors, as found in all the members of the DMSO reductase family, and a bidentate coordination with the oxygen atoms from the

side chain carboxylate group of an aspartate molecule (Asp_{222}) (Figure I.6) [60], which had been not observed in a mononuclear Mo-enzyme. The soluble NarGH shows a similar active site structure with two pterin molecules but, in contrast, the coordination with aspartic acid is through only one oxygen with the sixth coordination position being occupied by an oxo group at 1.8 Å (Figure I.6) [59]. These differences cannot be attributed to the redox state of the sample since both NarGHI and NarGH were crystallized in aerobic conditions and therefore the reported structures must represent oxidized forms of the enzymes. Another novel aspect of Nar is the unusual coordination of FeS0 by one histidine and three cysteines, which was found only once before in Ni-Fe Hydrogenase from *Desulfovibrio gigas* [59, 60, 62].

The redox and EPR properties of Nar from several sources have been the subject of several studies [52, 54, 58, 63-65]. Nars show two types of pH-dependent Mo(V) ion EPR signals, which show, in addition, resonance lines split by a solvent exchangeable proton. The Mo(V) ion species associated with these signals were named the low-pH (g_{av}=1.984, A_{av}=9.3G) and the high-pH (g_{av}=1.977, A_{av}=3.4 G) forms. The molecular structure of the active site of NarGHI does not show an hydroxyl/water ligand [60], as one would expect from the EPR data, and the coordination of the Mo site in NarGH presents an Oxo ligand and one oxygen from a carboxylate (Figure I.6) [59]. These results indicate that the bidentate coordination is open upon reduction to Mo(V) giving rise to the solvent exchangeable low- and high-pH forms of the enzymes. Recent studies performed in *Pn* NarGHI shows, besides the low and high pH signals, two novel EPR signals with no differences in D_2O exchanged samples that are obtained upon nitrate oxidation of reduced enzyme (Correia et al, *to be published*). These two species might be associated, in principle, with Mo(V) species having the molecular structure seen in both crystal structures of *Ec* Nar. The catalytic involvement of all these Mo(V) species is far from being elucidated and additional work is necessary to clarify their roles [52, 63].

EPR studies in *Ec* Nar detected the presence of only four FeS centers while the structures of NarGH and NarGHI demonstrated the existence of five FeS centers. The EPR signal of the [3Fe-4S] cluster (g_{av}=2.00) and one additional signal with two components (major and minor) was attributed to a single [4Fe-4S] center in different conformations (major, g_1=2.049, g_2=1.947, g_3=1.870 and minor, g_1=2.010, g_2=1.885, g_3=1.871) [64-66]. The EPR properties of the remaining EPR-detected two centers could not be determined precisely because of magnetic interaction between centers, which broaden the spectra making their deconvolution unfeasible. Recently, EPR studies by Rothery *et al*. performed in a NarG mutant that lacks the molybdenum site showed that the fifth FeS (FeS0) center is a [4Fe-4S] cluster in a high-spin configuration (g_1=5.556, g_2=5.023) [67].

I.5.1.2 Gene organization, expression control, and mechanism of action. In *E. coli*, the genes that code nitrate reductase are grouped in the operon *narGHJI* , which is located in the *chlC* locus of the chromosome. NarJ is a polypeptide that participates in NarGH assembly prior to its attachment to NarI in the membrane [68]. The expression of *nar* genes are nitrate/nitrite regulated by a signal transduction system of kinases-phosphatases, involving the operons *narXL* and *narQP*, (Figure I.8) [69]. The operon *narXL* is located in the *chlC* locus but *narQP* is coded out. NarX and NarQ are homologous membrane proteins that detect periplasmic nitrate and nitrite and then activate the NarL and NarP regulators by phosphorylation [70-73]. In this conformation, the regulators bind specific DNA consensus sequences called NarL heptamers [74]. The operons *narGHJI* (respiratory nitrate reductase), *frdABCD* (fumarate reductase) and *narK* are only under the control of NarL, while both NarL and NarP regulate *nrfABCDEFG* (nitrite reductase) and *napFDAGHBC* (periplasmic nitrate reductase) [71]. This is consequently, a complex regulatory system that detects the nitrate:nitrite ratio, inactivating NarL when nitrate is in low levels, and favoring nitrite consumption.

E. coli shows an additional Nar coded in the *narZWYV* operon in the *chlZ* locus, which is expressed constitutively at low levels, and its proposed role is to cushion the bacterium respiration to switch from oxygen to nitrate respiration [69].

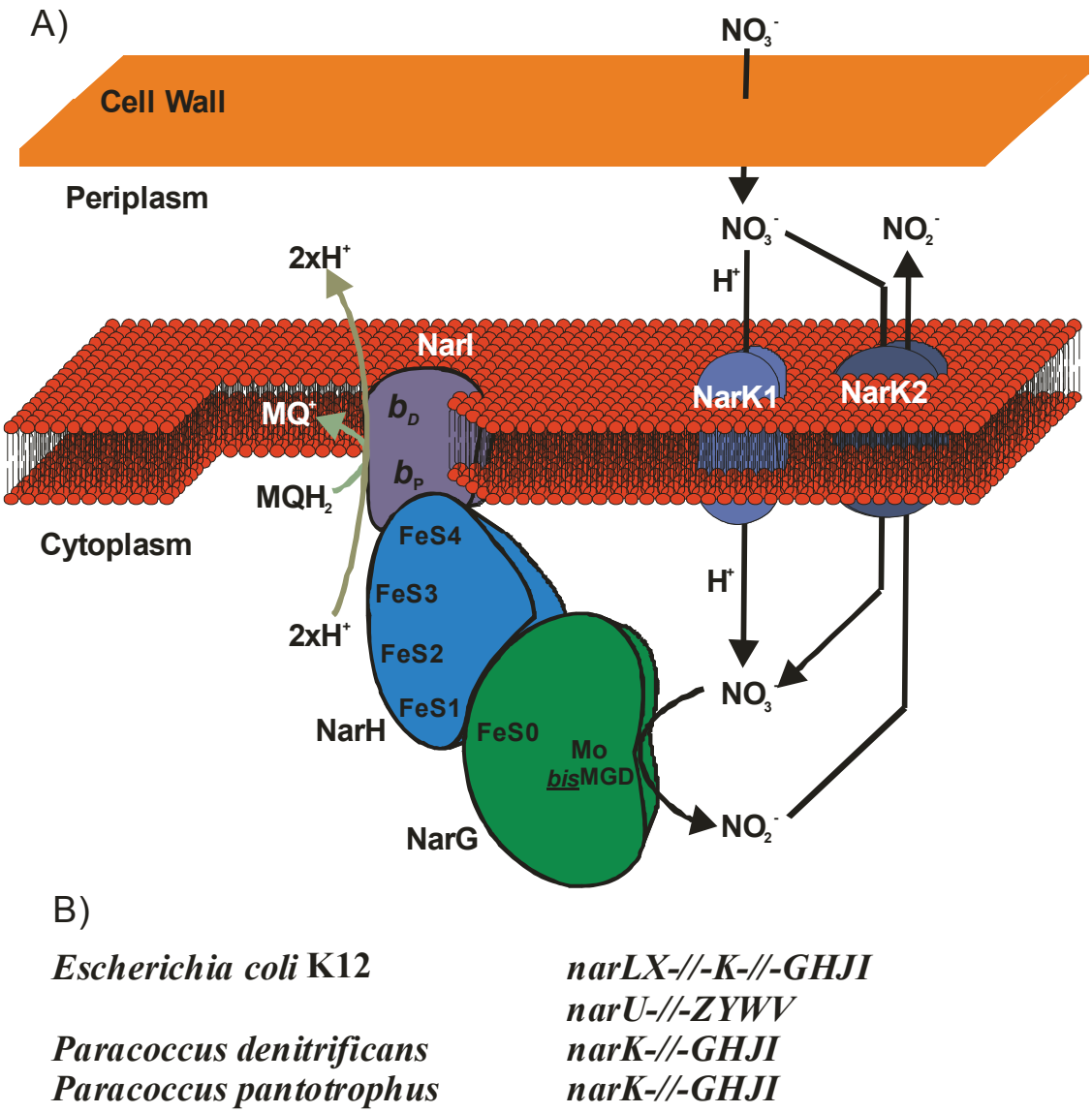

Figure I.8: A) Respiratory nitrate reduction by Nar enzymes. B) Gene organization of the *nar* gene clusters. Note the symbols "-" (short distance in the DNA sequence) and "-//-" (long distance in the DNA sequence). Reproduced from reference [17].

Nars in other bacteria such as *Paracoccus denitrificans* and *Paracoccus pantotrophus* are coded by operons with the same composition (Figure I.8). These operons code a Nar having basically the same molecular structure, but that differ in respect to those in *E. coli* in

how they control the expression system, with the transcription being under the control of the FNR-like regulator NarR [75].

The proposed mechanism for the reduction of nitrate to nitrite in *E. coli* K12 is schematized in Figure I.8. The MQH_2 situated in the outer part of the cytoplasmic membrane are oxidized by NarI translocating 2 protons into the periplasm. The two electrons are conducted through the electron transfer pathway of the NarGHI complex to the Mo-*bis*MGD site, where nitrate is reduced consuming two cytoplasmic protons. As the catalytic subunit of Nar is cytoplasmic, nitrate must be introduced into the cell. This is performed by two transporters. The proton:nitrate symporter NarK1 is activated at the beginning of the nitrate respiration and the co-transported protons are consumed in the nitrate reduction. Once the reaction accumulates nitrite, the function of NarK1 is substituted by NarK2, which acts as nitrate:nitrite antiporter, allowing the maintenance of the steady state [76]. This membrane process, when coupled to formate oxidation by the Fdh-N, generates the proton motive force (PMF) necessary for ATP synthesis [11, 77].

I.5.2 Periplasmic Nitrate Reductases

I.5.2.1 Molecular and spectroscopic properties. NapA from *D. desulfuricans* (*Dd* NapA) was the first reported structure for a periplasmic nitrate reductase (Figure I.9) [78, 79]. *Dd* NapA is a monomeric protein of ellipsoidal shape with an α/β type fold organized in four domains, all involved in cofactor binding. The active site is a hexa-coordinated Mo ion with four sulfur atoms from two pterin ligands, one hydroxo/water group and sulfur from a cysteine as ligands (Figure I.6). In addition, the protein has an iron-sulfur cluster of the type [4Fe-4S], which is supposed to be involved in electron transfer.

A funnel-like cavity is formed from the surface to the catalytic site (~15 Å) due to the spatial arrangement of domains II and III. The hydroxo/water ligand of the molybdenum atom, which is supposed to be in the position where the substrate binds the active site, points into

this channel, suggesting that nitrate entrance and nitrite exit would be via this channel. In contrast, Naps obtained from other sources such as *Rhodobacter sphaeroides* (*Rs* Nap) [80], *Cupriavidus necator* (*Cn* Nap, formerly *Alcaligenes eutrophus*, *Ralstonia eutropha*, *Wautersia eutropha*) [50] and *Paracoccus pantotrophus* (*Pp* Nap) [81, 82] are heterodimeric proteins with a large (80-90 kDa) and small (~15-17 kDa) subunits.

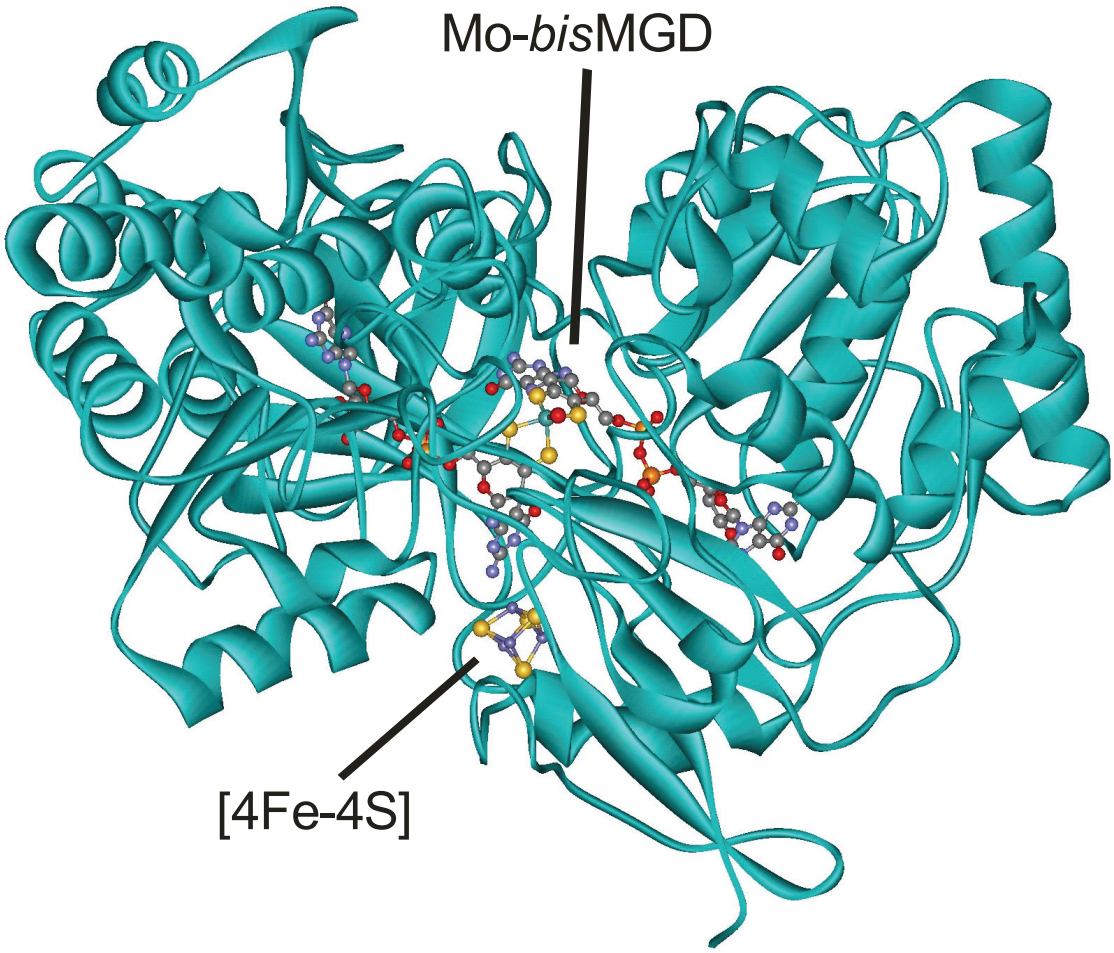

Figure I.9: Overall three-dimensional structure of NapA from *Desulfovibrio desulfuricans* ATCC 27774. Reproduced from reference [17].

The only crystal structure reported for an heterodimeric Nap belongs to *Rs* NapAB which was determined at a resolution of 3.2 Å [83, 84]. The arrangement of the catalytic subunits of *Dd* NapA and *Rs* NapA are very similar in terms of metal cofactor content, global fold and domain organization, with a RMSD of 1.26 Å for the 683 Cα atoms. However, their primary sequences reveal a low identity (~35%), although the Mo-*bis*MGD catalytic site and

[4Fe-4S] cluster binding residues are conserved along with the amino acids proposed to mediate the electron flow from the [4Fe-4S] center to the molybdenum [85, 86]. The structural comparison between all these proteins was recently reported by Moura *et al*. [61]. The small subunit NapB, which is present in most Naps but absent in *Dd* Nap, was recently determined at a higher resolution (1.25 Å) using the recombinant NapB protein from *Haemophilus influenzae* through MAD (multiwavelenght anomalous dispersion) methods [87].

EPR studies performed in *Dd* NapA and *Pp* NapAB indicate a Mo-site with high coordination flexibility as shown by the different EPR active species obtained with the enzymes poised at different redox potentials and in the presence of different inhibitors [88-93]. The *Pp* NapA enzyme in the as-prepared form shows a Mo(V) EPR signal (high g *resting*) typical of Mo(V) ion species (g_1=1.998, g_2=1.990, g_3=1.981) split by two non exchangeable species with nuclear spin I=1/2, presumed to be the β-methylene protons from the coordinated cysteine seen in the crystal structure of *Dd* NapA (A_{av}^1= 5.5 G, A_{av}^2=2.8 G). A similar resting EPR signal was detected in *Rs* NapAB [83]. Under slow-turnover conditions, the resting signal is replaced with a new Mo(V) ion signal (high g [nitrate]) showing a hyperfine split with a single non exchangeable proton (g_1=1.999, g_2=1.989, g_3=1.981, A_{av}=5.1 G), which was suggested to be a catalytic intermediary. This signal is similar to that obtained in *Dd* NapA when reacted in the same conditions [94]. The results in *Dd* NapA also show similar EPR signal in some cases in the presence of inhibitors [93]. The data obtained in both *Dd* NapA and *Rs* NapAB suggests that the active sites of the three enzymes are similar. Nevertheless, the coordination sphere deduced from EXAFS studies performed in *Pp* NapAB for the several Mo(V) species are in contradiction with the results presented in this work, which indicates that besides the bi-pterin coordination, the active site presents three extra ligands. This point will be discussed in this thesis.

I.5.2.2 Genes organization, expression control, and mechanism of action. The *nap* genes have been identified in several prokaryotic organisms (Figure I.10) [50, 80, 95-99]. In

contrast to the *nar* operon, the *nap* operons present heterogeneity both in gene composition and ordering. Eleven different genes have been identified as components for operons that code Naps in different organisms.

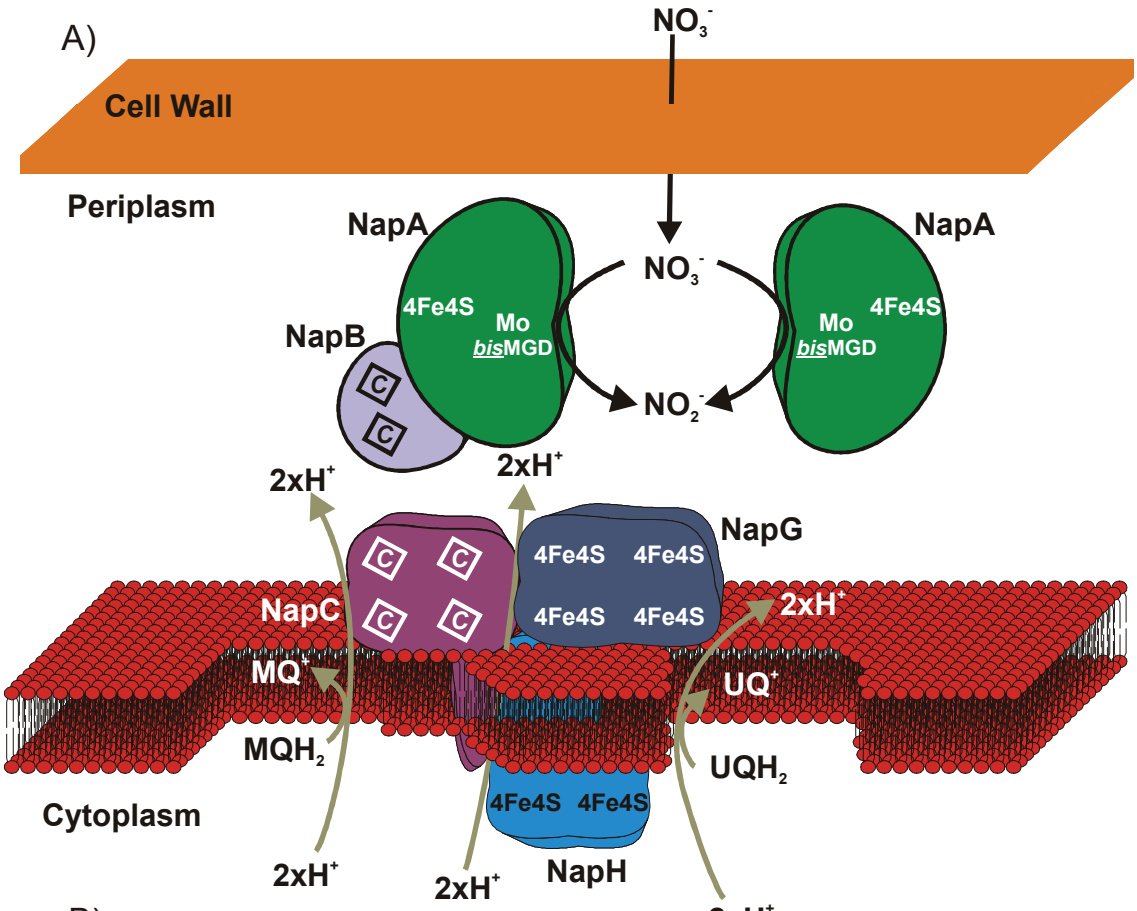

B)

Desulfovibrio desulfuricans	*napCMADGH*
Escherichia coli K12	*napFDAGHBC*
Campylobacter jejunii	*napAGHBLD*
Wollinella succinogenes	*napAGHBFLD*
Haemophylus influenzae	*napFDAGHBC*
Shewanella oneidensis MR1	*napDAGHB*
Desulfitobacterium hafniense	*napDGAH*
Cupriavidus necator	*napEDABC*
Paracoccus pantotrophus	*napEDABC*
Rhodobacter sphaeroides	*napKEFDABC*
Bradyrhizobium japonicum	*napEDABC*
Pseudomonas G-179	*napEFDABC*

Figure I.10: A) Dissimilatory nitrate reduction by Nap enzymes. B) Gene organization of the *nap* gene clusters. Reproduced from reference [17].

The *napA* gene codes the catalytic subunit NapA that contains the Mo-*bis*MGD active site and a FeS center. The assembling of the apo-protein with the metal cofactors is carried out in the cytoplasm. Then, the folded holo-protein is transported to periplasm by the TAT (Twin Arginine Translocator) system by recognizing the signal-peptide present in NapA [100]. However, this is not valid for all the catalytic subunits since although NapA from *Pseudomonas* G-179 is found in the periplasm, it lacks this signal peptide. Once in the periplasm, NapA and the product of *napB* gene are assembled to give the heterodimeric NapAB. NapB is secreted into periplasm by the general secretory pathway Sec [101]. This process occurs for all the Naps except for *Dd* NapA, which is obtained in monomeric form [94]. This should also be the case for *D. hafniense* DCB-2 NapA, whose *nap* operon and whole shotgun genomic sequence does not show the presence of the *napB* gene.

Almost all the *nap* operons code the protein NapC (Figure I.10), which is a *c*-type tetra-hemic membrane-anchored protein (~25 kDa) belonging to the NapC/NirT family [102-104]. This protein is involved in the electron transfer from the quinol pool to periplasmic reductases. When NapC is not coded in the *nap* operon, its function is substituted by another protein of the NapC/NirT family which is coded out of the operon and is expressed under the required conditions. Furthermore, the operons of *E. coli* K12 and *D. desulfuricans* code the ferredoxins NapG and NapH. NapG is a periplasmic protein having 4×[4Fe-4S] clusters. NapH is an integral membrane protein with 2×[4Fe-4S] exposed to the cytoplasm [105, 106]. The *nap* operon of *D. desulfuricans* codes for an additional protein called NapM. This is a putative soluble tetrahemic *c*-type cytochrome with periplasmic localization, and its proposed function is to transfer electrons from NapC to NapA. The remaining genes, *napD*, *napE*, *napF*, *napK* and *napL* code for different proteins that are not directly involved in the nitrate reduction.

NapD is a cytoplasmic protein that belongs to the TorD family, which act as chaperones and are always present in operons that code molybdo-enzymes [107]. NapF is a

cytoplasmic iron-sulfur containing protein with four loosely bound [4Fe-4S] clusters, which is thought to participate in the assembling of the iron-sulfur cluster of NapA [105, 108]. The other genes code for proteins with so far unknown functions.

The high diversity of *nap* operons suggest that nitrate reduction by Naps is not unique as in the case of Nars. Two proposed electron transfer pathways involved in nitrate reduction by periplasmic nitrate reductases are depicted in Figure I.10. One proposed for the Nap complex from *E. coli* K12, is used by the cell to support anaerobic metabolism as an alternative to the Nar pathway when nitrate concentration is low in the culture medium [109-114]. This pathway is used for nitrate respiration in bacteria that lack Nar such as *D. desulfuricans* [94], *Pseudomonas* sp. G-179 [98] and *B. japonicum* [95, 115]. As shown in Figure I.10 (right), the electrons necessary for nitrate reduction are obtained from the QH_2 pool (E^o=+90 mV), and then transferred to NapAB (NapA in enzymes lacking NapB) through an electron transfer chain mediated by the metal centers of NapHGC. This process implies the oxidation of two QH_2 molecules resulting in the translocation of 2H+ to the periplasm. The transport of two electrons from NapG to NapC would also be accompanied with translocation of two additional protons [106], which gives a net balance of 4 translocated protons, of which two are consumed in the nitrate reduction. The energetic balance for each nitrate molecule converted through the Nap complex would be as efficient as the Nar pathway since both systems produce a net gradient of two protons [11, 116]. This proposed mechanism should also occur in *Haemophilus influenzae* and *Shewanella oneidensis* MR-1 since they have the necessary genes to accomplish this function.

The second pathway is operative in organisms that express NapC but lack the *napG* and *napH* genes (*P. pantotrophus*, *C. necator*, *R. sphaeroides* and *R. capsulatus*). The electron transfer pathway between NapAB and the QH_2 pool is similar to the previous pathway, but is mediated only by NapC. The electrons necessary for nitrate reduction are provided by the QH_2 pool (Figure I.10 Left). As the two protons translocated to the periplasm

in the QH_2 oxidation are consumed in the nitrate reduction, this process gives no net proton gradient. Therefore, nitrate reduction is used in these organisms as an electron sink to eliminate an excess of reducing equivalents [50, 117-122] accumulated in the cytoplasm as NADH and $FADH_2$.

The *nap* operons of other bacteria that lack the necessary genes to perform nitrate reduction by any of these two pathways must use an alternative way or a modified mechanism of those proposed above. For instance, the *nap* clusters from *B. japonicum* and *Pseudomonas* sp. G-179 lack the *napGH* genes but are maximally expressed under denitrifying conditions [95, 98]. Another example is the *nap* cluster from *W. succinogenes* that lacks NapC but codes the *nrfH* and *fccC* genes in its genome which codes for proteins of the NapC/NirT family. The knockout of these genes does not abolish nitrate reduction through the Nap complex; suggesting that this bacterium uses an alternative pathway to transfer the electrons to NapAB [123]. The *nap* cluster from *Desulfitobacterium hafniense* DCB-2 lacks both NapB and NapC. However, a protein of the NapC/NirT family but not NapB can be found in the genome sequence. This would indicate that, as in *D. desulfuricans*, the periplasmic protein is a monomer that can receive electrons either directly from the NapC protein or through a periplasmic soluble mediator such as a cytochrome or a ferredoxin. Clearly, the mechanisms involved in the periplasmic nitrate reduction are not general and require additional investigation.

I.5.3 Assimilatory Nitrate Reductases

I.5.3.1 Molecular and spectroscopic properties. Nas is the first enzyme involved in the anabolic pathway of nitrogen assimilation (Figure I.4). These enzymes along with the *nas* genes have been reported from several bacteria. All the Nas isolated so far have an active site containing a Mo-*bis*MGD cofactor but the molecular properties and the number and type of electron transfer centers are diverse and vary in the different organisms. Nas from *Klebsiella*

pneumoniae and *Rhodobacter capsulatus* are heterodimers made up of a large catalytic subunit (90-105 kDa) and a small subunit (~45 KDa). The catalytic subunit contains, besides the active site, two FeS centers; one [4Fe-4S] and one [2Fe-2S], whereas the small subunit contains a FAD cofactor that uses NAD(P)H as an electron donor. In contrast, the catalytic subunit of *Bacillus subtilis* Nas contains the Mo-*bis*MGD cofactor and only one [4Fe-4S] center, whereas the small subunit holds 2×[2Fe-2S] centers and one FAD cofactor. Monomeric Nas has been found in *Azotobacter vinelandii* and Cyanobacteria. These proteins have molecular weights in the range 75-105 kDa and contain a Mo-*bis*MGD cofactor and one [4Fe-4S] center. The physiological electron donor is flavodoxin in *Azotobacter vinelandii* and flavodoxin and ferredoxin in Cyanobacteria [10, 13].

At present, no crystal structure has been reported for any assimilatory nitrate reductase. Monomeric Nas from cyanobacteria is closely related to *Dd* NapA, which is in line with phylogeny calculations that indicate that Nas proteins are more related to Naps than Nars [51].

NarB from the cyanobacteria *Synechococcus* sp. strain PCC 7942 represents the best spectroscopic characterized assimilatory nitrate reductase so far. Note that the notation Nar is used to identify an assimilatory nitrate reductase. EPR studies confirmed the presence of one [4Fe-4S] cluster/molecule having a midpoint redox potential of -190mV (*vs*. normal hydrogen electrode, NHE) for the $[4Fe\text{-}4S]^{2+/1+}$ couple. EPR characterization of the Mo center revealed similar EPR signals to those obtained in periplasmic nitrate reductases but obtained with the samples poised at different redox potentials and conditions. Dithionite reduction of NarB yields a Mo(V) signal similar to the High g [resting] reported for *Pp* NapAB whereas oxidation with air of this sample shows an EPR signal similar to that obtained by treating *Pp* NapAB and *Dd* NapA with cyanide, indicating that despite both enzymes yielding similar Mo species, they have different redox properties. EPR redox titration of the "High g" Mo(V) species reveal midpoint redox potentials of -150mV and <-550mV for the $Mo^{6+/5+}$ and for $Mo^{5+/4+}$ couples, respectively. These values suggest that the Mo center cannot be reduced to

Mo(IV). This reduction should occur only after the nitrate binding to Mo(V), which raises the midpoint redox potential of the $Mo^{5+/4+}$ couple to -350 mV [124]. This increase in the $Mo^{5+/4+}$ redox potential triggers the electron transfer from the reduced iron-sulfur cluster to the molybdenum, providing the two electrons required for nitrate reduction to nitrite.

I.5.3.2 Genes organization, expression control, and mechanism of action. The *nas* genes are clustered in operons with different compositions as observed in Naps (Figure I.11). The expression of this operon in both *K. pneumoniae* and *R. capsulatus* was found to be insensitive to oxygen but induced by nitrate and nitrite, and repressed by the presence of ammonium in the culture medium. For example, in both *K. pneumoniae* and *R. capsulatus*, the *nasR* gene located upstream from the *nasFEDCBA* operon encodes a transcription antiterminator, which is a positive regulator subject to the presence of nitrate and nitrite. The *nasFEDCBA* operon encodes a typical ABC-type nitrate/nitrite transporter in *nasFED*, a siroheme assimilatory nitrite reductase in *nasB*, and the NADH-dependent assimilatory nitrate reductase, where *nasC* encodes the small FAD-containing subunit and *nasA* the catalytic subunit (Figure I.11). In contrast, the catalogue of genes in *Bacillus subtillis* is different (Figure I.11). The *nasBC* genes code the small and the catalytic subunits, respectively, a nitrate transporter is coded in *nasA*, and a soluble NADH-nitrite reductase is expressed from the *nasDE* genes. Furthermore, this cluster has *nasF*, a gene involved in the biosynthesis of heme cofactors. A different situation is found in the genus Cyanobacteria which, as seen above, produce monomeric nitrate reductase NarB. Usually, *narB* gene is co-transcribed with the *nrtABCD* nitrate transport genes and the nitrite reductase *nirA*.

Because of the cytoplasmic localization of the enzyme, nitrate reduction takes place strictly in the cytoplasm and it therefore has to be transported into the cell. The nitrate uptake is performed by specific transporters, which are usually coded, as seen above, in the same genomic region of *nas* genes. Once in the cytoplasm, the nitrate anion is reduced at the catalytic site in Nas releasing nitrite; which is exported to the periplasm and immediately

reduced to ammonium in a six-electron reaction catalyzed by Nir. This ammonium is then transferred to the cytoplasm and incorporated into biomolecules through the Glutamine Synthetase and GOGAT pathways (Figure I.4) [10, 13].

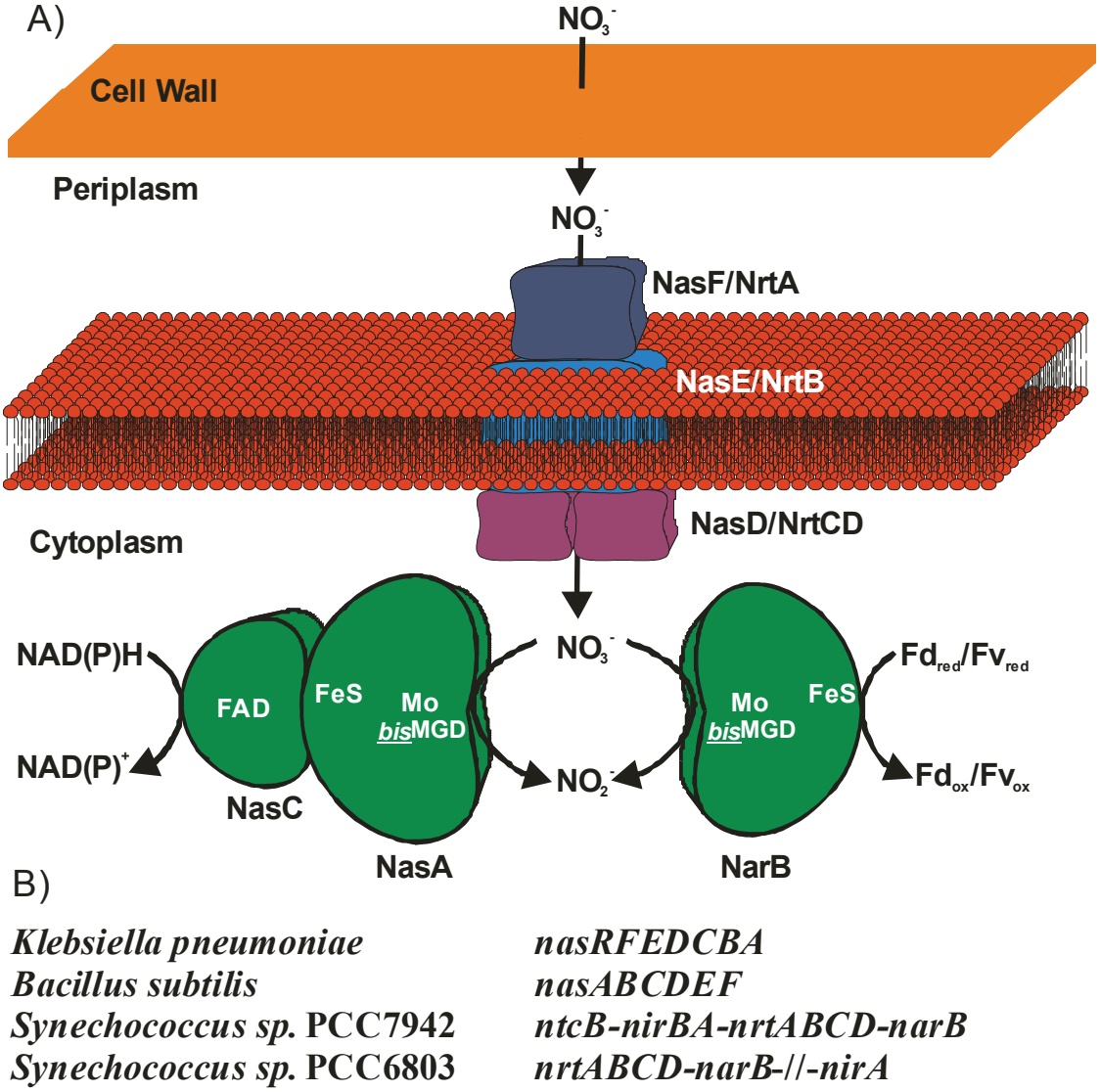

Figure I.11: A) Pathway for nitrate assimilation by Nas enzymes. The figure depicts the enzymes of the *Klebsiella*/*Rhodobacter* (left) and Cyanobacteria (right) groups. B) Organization of the gene clusters from the discussed examples. The meaning of the symbols "-" and "-//-" are given in the caption to Fig. 4. Adapted from reference [17].

I.6 Electronic configuration of the metal cofactors of NapA and its detection by EPR spectroscopy

Two types of metal centers were studied in this work by EPR spectroscopy, Mo and Fe.

I.6.1 Electronic properties of the Mo ions

The electronic configuration of the ground state of the neutral gaseous Molybdenum shown in Figure I.12 indicates that this atom has several oxidation states which might be potentially paramagnetic. However, these configurations cannot be straightly applied to model the properties of the ion in molecules or complexes since in the ground state of an atom (the condition in which it is ordinarily found) the electron configuration generally follows the Aufbau principle corresponding to a spherical geometry.

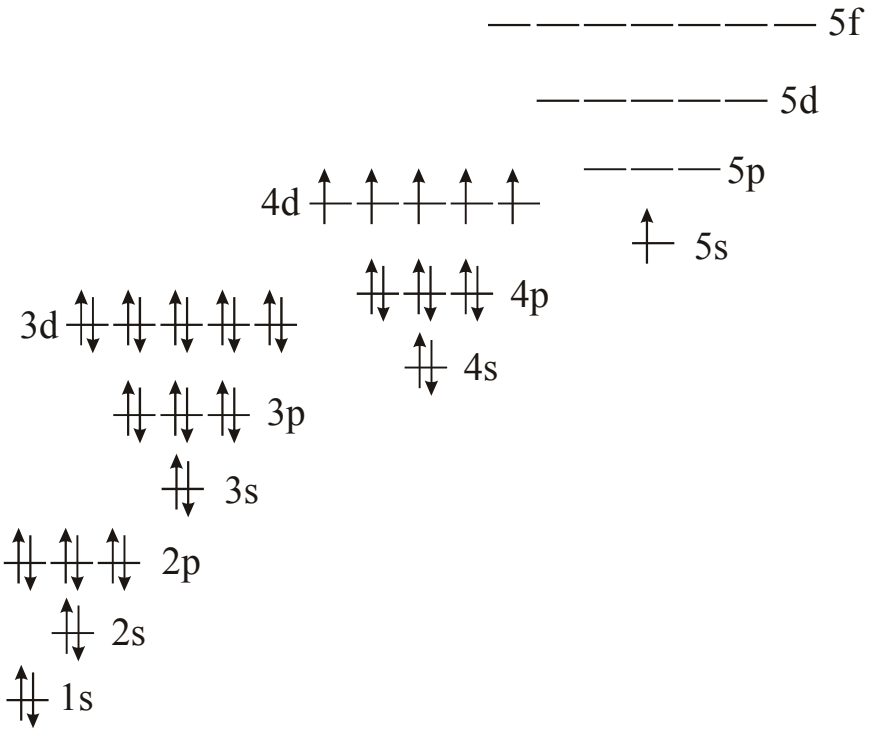

Figure I.12: ground state electronic configuration (^{7}S, Kr: $4d^5\ 5s^1$) of the isolated Mo atom in gaseous state.

For example, one could expect that both the +4 and +5 oxidation states, which are relevant in biology, present paramagnetism, but only the +5 redox state has been detected by EPR spectroscopy until now.

Single crystal EPR spectroscopy and DFT calculations of the model compounds *cis,trans*-(L-N_2S_2)$Mo^{V}OX$ (X= Cl, SCH_2Ph) demonstrated that the five 4d atomic orbitals do not hybridize with the 5s, and the five 4d orbitals were found to have lower energy than the 5s [125], indicating that the electronic configuration of the isolated gaseous atom is not applicable to Mo within molecules or complexes. Furthermore, the 4d orbitals are external enough as to form strong bonds and then the strong crystal field scheme should be used instead of the weak crystal field method usually applied to 3d transition metals. Figure I.13 shows the relative order of energy levels in two hypothetical distorted octahedral Mo complexes, axially elongated and compressed octahedrons.

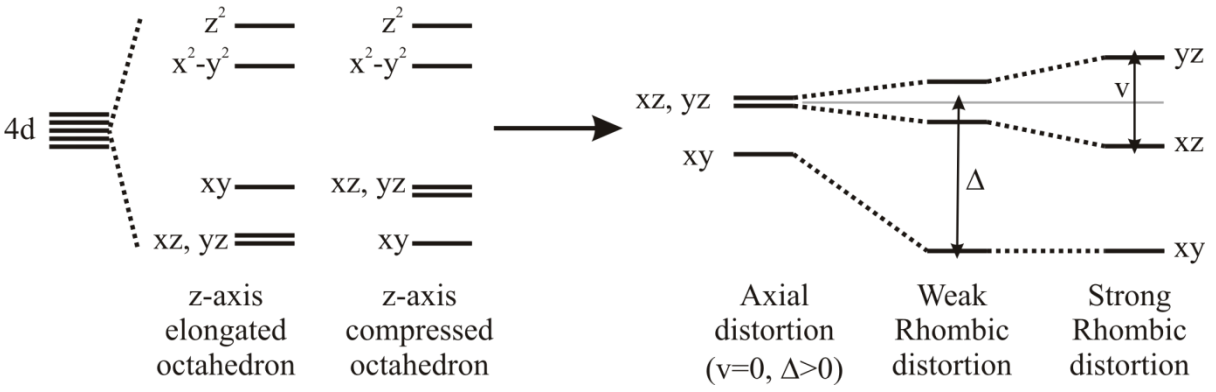

Figure I.13: relative order of the energy levels of, Left: the five 4d orbitals for cubic and two common distorted octahedral geometries, Right: energy levels of the three lowest 4d orbitals under axial and two degrees of rhombic distortions. Energy levels were extrapolated from former calculations of the 3d orbitals of Ni(I), Ni(III) and Cu(II) [126], and DFT calculations of reference [125].

Usually, Mo systems are modelled assuming a z-axis compressed octahedron. Taking this into account, two possibities exist to explain the diamagnetism of the Mo^{4+} ion. One is the pairing of the electrons in the d_{xy} orbital of the Mo(IV) ion which should occur if the energy gap (Δ) between the d_{xy} and d_{xz} (and also d_{yz} if the rhombic distortion is negligible, v~0) orbitals is larger than the energy required to pair the electrons spins. The second possibility should occur if the energy gap (Δ) is small in comparison with the energy needed to pair the

electrons. In such a case, both d_{xy} and d_{xz} (or d_{yz}) orbitals should be occupied by one electron resulting in a triplet state configuration with S=1. This S=1 system could be also split by zero-field splitting (ZFS). In this case, the Hamiltonian of this sytem is given by

$$H = \mu_B \boldsymbol{BgS} + \mathrm{D}\left(S_z^2 - \frac{1}{3}S(S+1)\right) + \mathrm{E}\left(S_x^2 - S_y^2\right)$$

where the different terms have the usual meaning [127].

Figure I.14 shows the energy levels as a function of the intensity of the magnetic field in the case of an S=1 system with ZFS=0 (Figure I.14 a) and ZFS≠0 (Figure I.14 b and c) for the case of an axial distorsion (D>0). The states with m_s=±1 can be additionally split from the state with m_s=0 under the effect of a rhombic component (E ≠0, not shown) [126, 128].

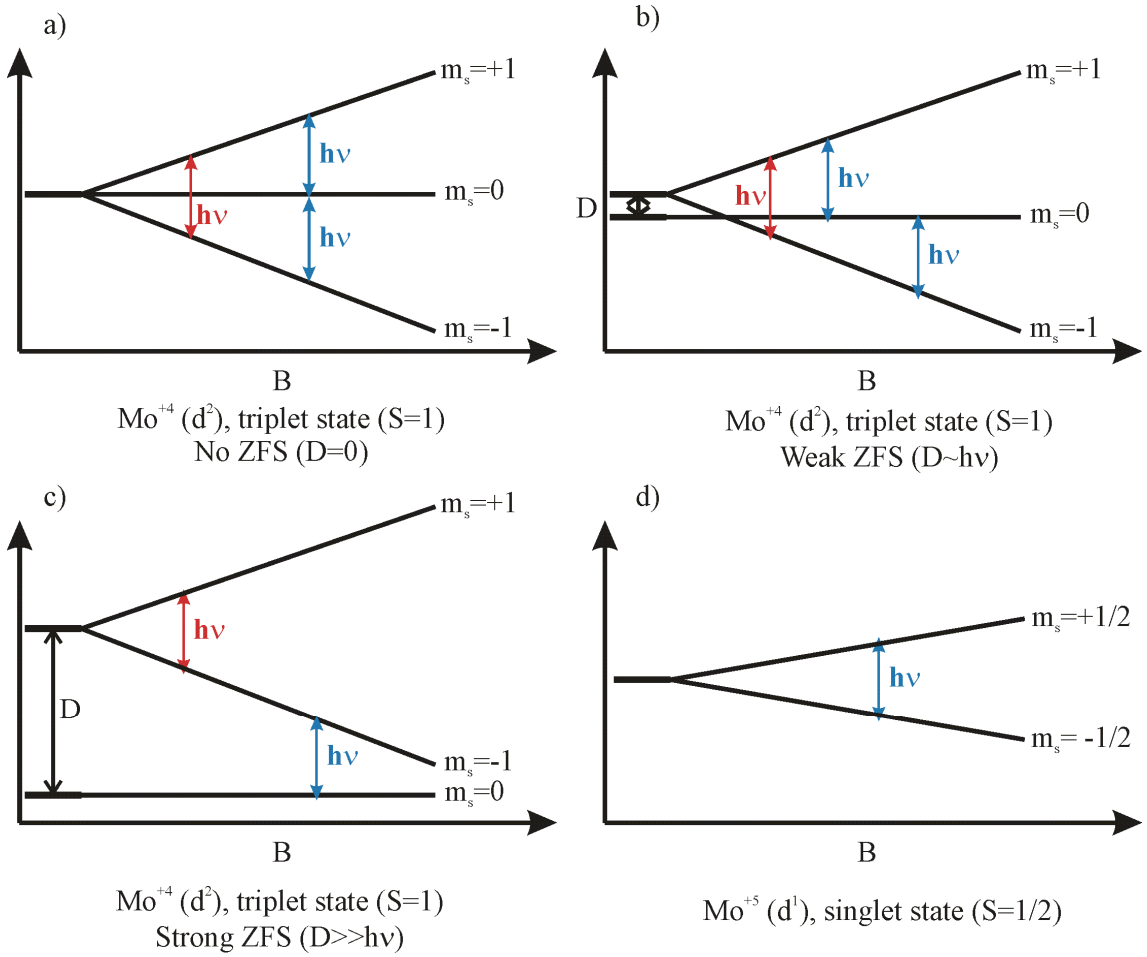

Figure I.14: Electron spin energy levels behavior for S=1 in a tetragonal (a-without ZFS, b-weak ZFS and c-strong ZFS) and S=1/2 with B_L parallel to the *z*-axis. Allowed transitions are depicted in blue. The forbidden

transitions (by the EPR selection rule $\Delta m_s=\pm1$) are in red. Note that a single EPR line should be observed in all cases with the only exception of the triplet state with D~hν.

Zero-field splittings causes magnetic anisotropy, and has deep effects on the magnetic properties. Since the $m_s= 0$ state is non-magnetic and transitions within $m_s= \pm1$ are forbidden by the EPR selection rule $\Delta m_s= \pm1$, Mo(IV) would be EPR active only when the intensity of the magnetic field B is large enough to reduce the energy gap to within hν between the $m_s= 0$ level and one of the $m_s= \pm1$ (Figure I.14 b and c). However, if in addition to the tetragonal distortion the rhombic distortion (E) is also present, the states become admixtures of those $m_s=\pm1$ and $m_s=0$. Consequently, the forbidden transitions become detectable and, qualitatively, the intensities of these will grow up proportional to the rhombic distortion (E).

At present, EPR spectra taken X- and Q-band failed to show any resonance attributable to Mo(IV) species. Thus, the confirmation of the electronic configuration of the Mo(IV) has not been elucidated yet and perhaps EPR experiments at higher frequencies could solve this issue.

In contrast, the EPR active Mo(V) ion was extensively studied through X-band EPR spectroscopy since the year 1959. This ion has a d^1 electronic configuration (singlet state, S= ½, Figure I.14 d) which is EPR detectable at temperatures below 300 K, in a narrow range of *g*-values that varies between ~1.95 and ~2.10, compatible with d_{xy} as ground state as proposed before in Figure I.13.

I.6.2 Electronic properties of the [4Fe-4S] clusters

The two protein studied in this work include as electron transfer centers iron-sulfur clusters of the type 4Fe-4S. These centers have a cubane-type structure with Fe-Fe average distances of ~2.7 Å (Figure I.15), in which sulfido ligands bridge three Fe ions and each Fe iron is coordinated by one cysteine thiolate. The [4Fe-4S] clusters can be obtained in at least three different redox states, but the redox states of the clusters studied here correspond to

$[4Fe\text{-}4S]^{+2}$ and $[4Fe\text{-}4S]^{+1}$. The configuration $[4Fe\text{-}4S]^{+2}$ comprises 2× Fe^{+2} and 2× Fe^{+3} with a ground state with S=0, which is diamagnetic and cannot be detected by EPR. The configuration $[4Fe\text{-}4S]^{+1}$ is composed of 3× Fe^{+2} and one Fe^{+3}, which in all the cases analyzed here gives a paramagnetic ground state with S=1/2.

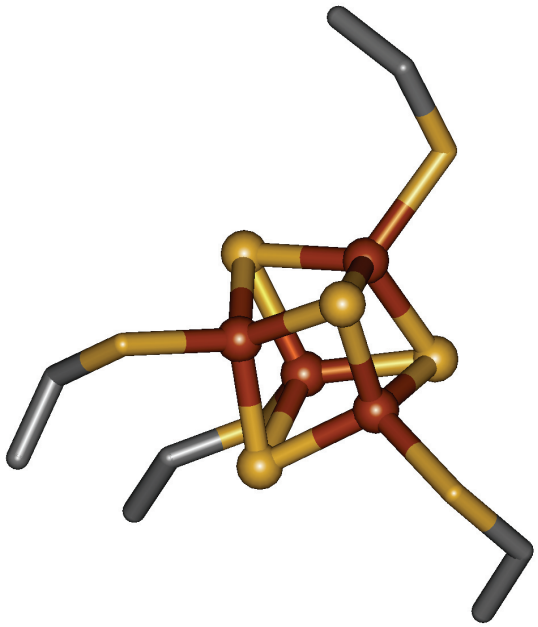

Figure I.15: 3D structure of the 4Fe-4S cluster from *Dd* NapA. Element color code, brown: iron, yellow: sulfur, grey: carbon. Heteroatoms are represented as balls and cysteine sidechains as sticks.

MATERIALS AND METHODS

II.1 *Desulfovibrio desulfuricans* ATCC 27774 cultures conditions and media composition

The composition of the culture medium of *Desulfovibrio desulfuricans* ATCC 27774 for 1 L of medium is:

- Na-lactate 60%: 10 ml
- NH_4Cl: 1.9 g
- K_2HPO_4: 0.47g
- $NaNO_3$: 2.28 g
- $MgCl_2.6H_2O$: 1.55 g
- $CaCl_2.2H_2O$: 0.19 g
- $FeCl_2.4H_2O$: 6.8 mg
- $Na_2S.9H_2O$: 0.2 g pH=7.1
- Yeast-extract: 0.95 g
- Trace elements: 10 ml

The composition of the trace elements solution (labelled as 100X) for 1 L is:

- $FeCl_2.4H_2O$: 0.21 g
- $MnCl_2.4H_2O$: 0.1 g
- $CoCl_2.6H_2O$: 0.17 g
- $ZnCl_2$: 0.1 g
- $CuCl_2.H_2O$: 0.02g
- H_3BO_3: 0.01 g
- Na_2SeO_3: 0.017g
- Na_2MoO_4: 0.01 g
- $NiCl_2.6H_2O$: 0.128 g
- nitrilotriacetic acid : 12.8 g
- (ajusted to pH=6.5 with KOH)

II.2 Cultures and media composition of *Cupriavidus necator* H16

C. necator H16 and HF210 strains were grown in mineral medium for chemolithotrophic growth. The media composition is described in Table 1.

Table 1: Medium composition for chemolithotrophic cultures of *C. necator* under aerobic conditions.

Component	mL added / 1L culture	Stock concentration % P/V	Final concentration % P/V
$MgSO_4.7H_2O$	1	20% in H_2O	0.02%
$CaCl_2.2H_2O$	1	1% in H_2O	0.001%
NH_4Cl	10	20% in H_2O	0.2%
$FeCl_3$	1	0.5% in 0.1N HCl	0.0005%
Fructose	10	40% in H_2O	0.4%
SL6 solution	5	see [85, 86]	-
H16 buffer	100	see [85, 86]	set the pH 7-8
Tetracycline	1	10 mg/mL	10 mg/L

All the solutions were autoclaved 20 min at 120 ºC, except for the $FeCl_3$ and Fructose solutions that were sterilized using ultrafiltration (0.2 μm pore diameter).

Antibiotic supplemented media was used to culture the *napEDABC* defective strains carrying the pCM62-nap plasmid with a tetracycline resistant cassette coding either the native or mutant *C. necator nap* operon [85, 86].

To start a culture, an aliquot of 20 μL of *C. necator* (ΔpHG1-H210/pNAP62-2 strain) glycerol stock was plaqued in Nutrient Broth Agar plates and incubated overnight at 30ºC. Ten colonies were pick-up and resuspended in 4×100 mL of saline medium and incubated overnight at 30ºC and 190 rpm. The saturated cultures were used to inoculate 18 L of the same medium and incubated at 30ºC and 200 rpm until late death-phase (~45 h).

II.3 *Desulfovibrio desulfuricans* NapA purification protocol

D. desulfuricans ATCC 27774 cultured under anaerobic conditions using nitrate as final electron acceptor express nitrate reductase activity that can be detected in the soluble extract. The cells were grown as described before [129] using the medium described in II.1, harvested in 10 mM Tris-HCl (tris-hydroxymethyl-aminomethane) pH 7.60, and passed through a Manton-Gaulin press at 9,000 psi. The cell debris was centrifuged at 16,000g for 30 min. In order to obtain the soluble fraction, the supernatant was ultracentrifuged at 180,000g for 1 h.

Purification of *Dd* NapA up to electrophoretic grade was carried out at 277 K under aerobic conditions through a four-step protocol summarized in Figure II.1 [93], which has some modifications with respect to the previous ones [94, 130].

The soluble extract was loaded into a DEAE-cellulose (-diethylaminoethyl-cellulose) column equilibrated with 10 mM Tris-HCl pH 7.6. The different proteins are separated in bands according to their charges. Cytochromes c_3 (tetrahemic) and c_{553} (monohemic) do not bind and elute as the flowthrough together with many other proteins so far uncharacterized. If column loading capacity is not saturated, all the other proteins remain bound. Adenylate kinase and hemic proteins are eluted during the first gradient (10-250 mM Tris-HCl), followed by most of the ATP sulfurylase. At 75-100 mM buffer molarity, an intense red band starts eluting from the upper part of the column. This fraction contains all the nitrate reductase and formate dehydrogenase activities, which are accompanied by ATP sulfurylase, Fuscoredoxin (prismane protein), Split Soret (the protein responsible of the intense red color), Desulforedoxin and some flavoproteins. At the final of the first gradient, the periplasmic Ni-Fe Hydrogenase is eluted. When the second gradient is started (250-500 mM buffer molarity), APS reductase is eluted overlapping the hydrogenase containing fraction. The subsequent four eluted fractions contain mainly Desulfoviridin, Rubredoxin, Flavodoxin and Ferredoxin, respectively.

Remarkably, when the column loading capacity is saturated, all the proteins less acidic than APS reductase or Desulfoviridin (depending on the saturation level) are eluted as the flowthrough. However and in contrast with that expected, no nitrate reductase and/or formate dehydrogenase activities are detected in the flowthrough fraction. Interestingly, at the 75-100 mM buffer molarity, the intense red band elutes from the upper part of the column as in non-saturating conditions carrying the whole NR and Fdh activities, as well as the other proteins that usually co-purify with them. This suggests that the proteins that comprise this fraction interact with very acidic proteins (probably ferredoxins) and unbind when the 75-100 mM buffer molarity is achieved. This observation could indicate that both NapA and FdhABC interact with very acidic proteins *in vivo*, and these complexes are disrupted by increasing the ionic stength in aerobic conditions. However, this could be an artifact produced by mixing cytoplasmic and periplasmic proteins in low salt concentration.

The fractions containing nitrate reductase activity were pooled, dialyzed against 10 mM Tris-HCl pH 7.6, and loaded into a Q-Sepharose column. NapA is eluted at ~100 mM buffer molarity, after hemic proteins and a large amount of ATPs. The remaining APS reductase is eluted at higher ionic strength and is fully resolved. At this point, NapA co-purify with FdhABC, Fuscoredoxin and ATPs.

After elution, fractions containing nitrate reductase activity were pooled and loaded into a Hydroxyapatite column equilibrated with 100 mM Tris-HCl pH 7.6 and were eluted with a potassium phosphate linear gradient. The Hydroxyapatite column resolves a Fuscoredoxin-containing fraction, followed by NapA together with ATPs, and finally FdhABC.

The pool containing *Dd* NapA was dialyzed against 5 mM phosphate buffer pH 8.0, and was loaded into a Resource Q (Pharmacia) column. *Dd* NapA was eluted with a linear gradient in the 15–20 mM buffer molarity. NapA is purified from ATPs with high efficiency.

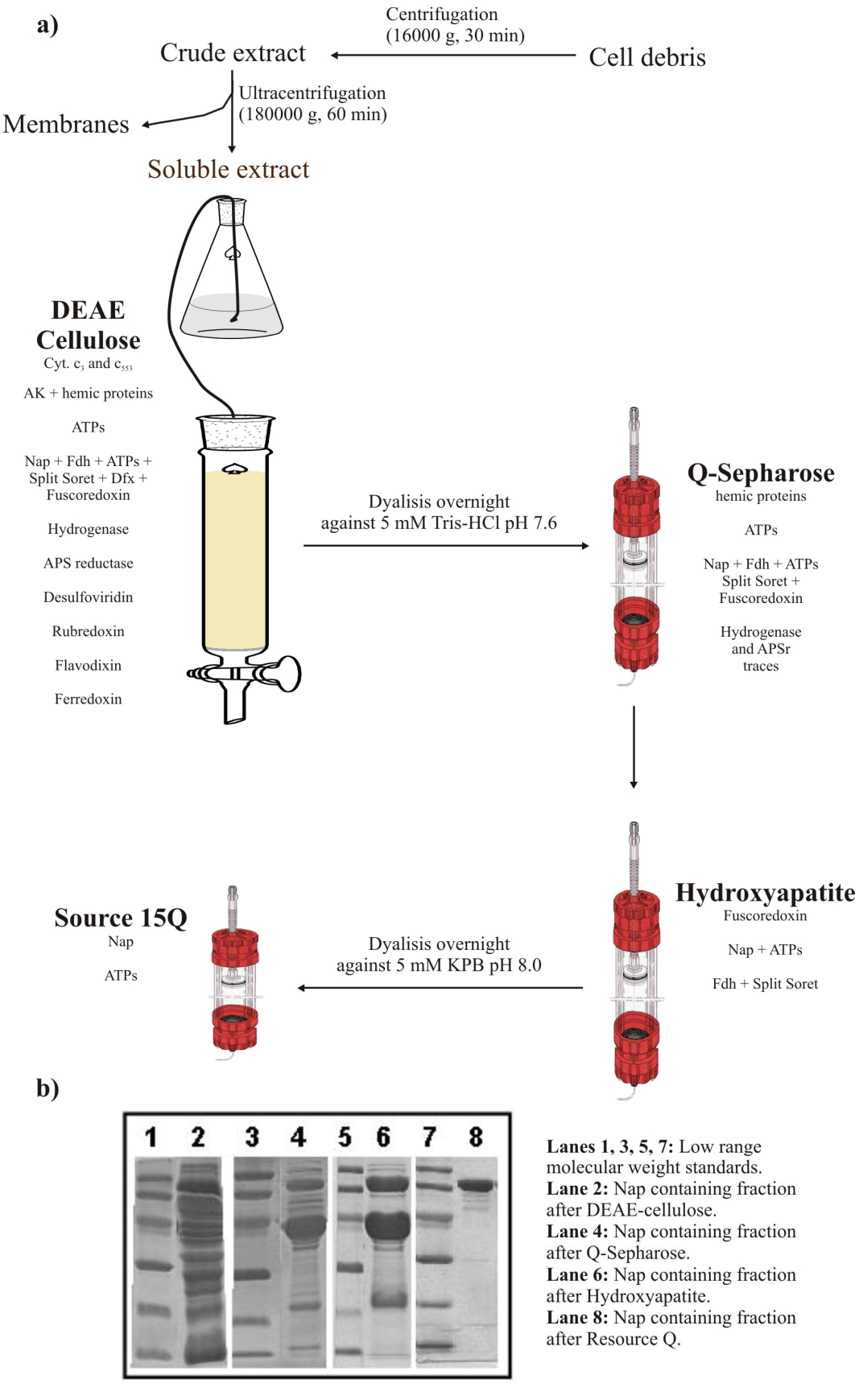

Figure II.1: a) Purification flowchart and elution order of known proteins. b) SDS-PAGE of the pools having nitrate reductase activity after each chromatographic step.

II.4 Preparation of periplasmic extract from *C. necator*

The culture was centrifuged (20 min at 5000g) and the supernatant was discarded. The pellet was carefully resuspended in 50 mM Tris-HCl pH 7.6, centrifuged again for 20 min at 5000g, and the supernatant was discarded. The washed cells were resuspended in lysis solution (10 mM Tris-HCl pH 7.6 + 0.5 M Sucrose) using 5 mL of the solution for each gram of pellet. An EDTA solution was added to a final concentration of 1 mM and the cells were stirred softly for 10 min at 30 ºC. Then, Lysozyme (20 mg/gram of pellet) was added and the cells were stirred vigorously for further 30 min at room temperature. The resulting suspension was centrifuged for 20 min at 5000g. The pellet comprised the spheroplast fraction and the supernatant the periplasmic extract, which was clear and had a faint pink colour.

II.5 *Cupriavidus necator* NapAB purification protocol

Periplasmic nitrate reductase from *C. necator* H210-pNAP62-2 was purified to homogeneity through a four step protocol. The periplasmic extract was dialyzed overnight against 10 mM MES pH 5.5 and loaded into a source 15S. A sodium chloride gradient (50 column volumes) was used, and nitrate reductase was eluted at 200-250 mM NaCl. The protein was concentrated and injected in a Superdex 200 column equilibrated with 100 mM Tris-HCl pH 7.6. This step removes all the lysozyme added for periplasmic extract preparation. The pool having nitrate reductase activity was dialyzed against 10 mM MES pH 5.5 and loaded into a source15S using the same running conditions of the first step.

As shown in Figure II.2, after these three chromatographic steps the enzyme was not 100% pure as judged by SDS-PAGE. The pure enzyme was obtained after crystallization, as described for few other proteins.

Lanes 2, 4, 6: Low range molecular weight standards.
Lane 1: Periplasmic extract.
Lane 3: Nap containing fraction after Source 15S column.
Lane 5: Nap containing fraction after Superdex 200 column.
Lane 7: Nap containing fraction after second Source 15S column.

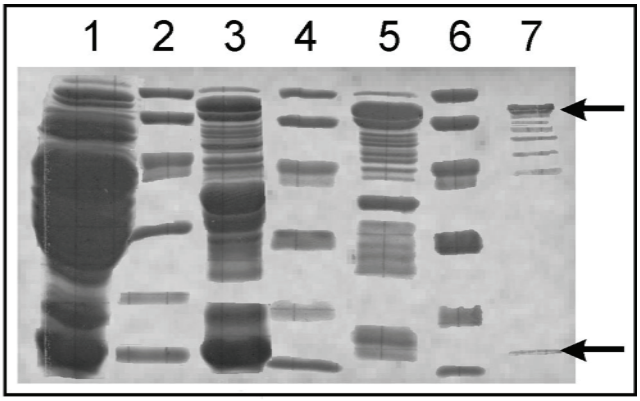

Figure II.2: SDS-PAGE of the pools having nitrate reductase activity after each chromatographic step.

II.6 Enzyme activity assays

II.6.1 Discontinuous method. The accumulated nitrite was determined as previously described [130], but with some modifications [93]. Enzyme (50 nM) was preincubated for 10 minutes at 30ºC with a solution containing 100 mM Tris-HCl pH 7.6, 5 mM methyl viologen and 5 mM sodium dithionite under aerobic conditions. Final volume of the reaction mixture was 500 µL. The reaction was started by the addition of the substrate (5 µM to 100 mM) and was allowed to proceed for 30 seconds. Reaction was then stopped oxidizing the methyl viologen by vigorous vortexing. The solution was reacted with 500 µL of sulphonic acid (0.12 %) and 500 µL of naphtyl-ethylendiamine (0.6 %) for 10 min to fully develop a pink color. Absorbance was recorded at 540 nm. One unit of nitrate reductase activity (U) corresponds to one µmol of nitrite formed *per* minute.

II.6.2 Continuous method. Enzyme (100 nM) was pre-incubated for 10 min at 37ºC with a solution containing 100 mM Tris-HCl pH 7.6, 200 µM methyl viologen and 130 mM β-mercaptoethanol under strictly anaerobic conditions. A previously degassed sodium dithionite solution (5 mg/mL) was added under anaerobic conditions until reach $A_{(600nm)}$= 1.5 and incubated for 10 min. The reaction was started when $A_{(600nm)}$= 1.0 by adding the substrate. Stoppered quartz cells (1 mL) provided with magnetic stirrers were used for the assay.

The nitrate reduction was measured indirectly following the oxidation of the methyl viologen at 600 nm (ε_{600nm}= 12 mM^{-1} cm^{-1}). Taking into account that two molecules of methyl viologen are oxidized *per* each nitrate reduced, one unit of nitrate reductase activity (U= μmol nitrite formed *per* minute) corresponds to 2 μmol of MV oxidized *per* minute.

II.7 Protein quantification

The total protein concentration was determined using both the Bicinchoninic acid kit from Sigma and for *Dd* NapA the extinction coefficient at 400 nm ($\varepsilon_{(400nm)}$= 24 mM^{-1} cm^{-1}).

II.8 Metal quantification

Both molybdenum and iron contents were determined through Inductively Coupled Plasma (ICP) Emission in a Jobin-Yvon (Ultima) instrument using the Reagecon 23 ICP multielements as standard solution in a concentration range of 0.05-1.5 ppm.

II.9 UV-Vis spectroscopy

Routine UV-Vis spectra and photometric measurements were recorded with a Shimadzu UV-160A spectrometer provided with a double-holder for sample and reference, which has a wavelength resolution of 0.5 nm in the range of 200 - 1100 nm.

Continuous kinetic assays were recorded in an Agilent 8453 diode array spectroscopy system (sampling interval 0.9 nm between 190 – 1100 nm), provided with a single-cell thermosettable holder in an open sample compartment.

II.10 EPR spectroscopy

X-band spectra were recorded with a Bruker EMX spectrometer equipped with a dual-mode cavity (model ER4116DM) and an Oxford Instruments continuous-flow cryostat. Simulations were performed using the WIN-EPR Simfonia V1.2 software from Bruker

Instruments. All the samples were prepared in 100 mM N-tris (hydroxymethyl)methylglycine (Tricine) pH 8.0 with a protein concentration of 200 μM. All the spectra were obtained in nonsaturating conditions at 25 and 100 K. For the spectra taken at 25 K, the experimental conditions were as follows: microwave power, 0.6 mW; modulation amplitude, 5 G. For the spectra taken at 100 K, unless otherwise stated, the conditions were the same except for a microwave power of 2 mW. Spin quantification of the Mo(V) and FeS signals was estimated by double integration and comparison with a 1 mM Cu-EDTA standard.

II.11 Spectro-potentiometric redox titrations

Redox titrations were carried out in an anaerobic chamber at room temperature working at an oxygen concentration below 1 ppm. A platinum–silver/silver chloride combined electrode (Crison) was used to determine the electrochemical potential. The samples were incubated with the mediators methyl viologen (-440 mV), neutral red (-325 mV), anthroquinone (-225 mV), fenazine (-125 mV), indigotetrasulfonic acid (-46 mV), duroquinone (5 mV), galocyanine (30 mV), fenazine etasulfate (55 mV), fenazine metasulfate (80 mV), 2,5-dimethyl benzoquinone (180 mV), and 2,6-dichlorophenol indophenol (217 mV). The electrochemical potential was dropped using a sodium dithionite (40 mg/ml) solution dissolved in 100 mM Tricine pH 8.0. Samples for EPR spectroscopy were taken after equilibration at each potential and were frozen in liquid nitrogen. EPR spectra were recorded at 25 and 100 K as described already in II.10.

II.12 Crystallization of native and reacted *Dd* NapA samples

Crystals of *Dd* NapA were obtained using 20-30 mg/mL pure protein solution with the hanging-drop and sitting-drop vapour-diffusion methods. 6% Polyethylene glycol (PEG) 8K in 100 mM MES pH=6.5 was used as precipitant [78]. The crystals grow overnight at room temperature (~295 K) both in aerobic and anaerobic conditions reaching the maximum size in

2 or 3 days. The crystals are very sensitive to handling and to radiation, losing its diffraction power in ~3 hours at 277 K with cryoprotecting solution (25% glycerol, 8% PEG 8K, 100 mM MES pH=6.5).

II.13 Data collection and processing of crystallized samples of *Dd* NapA

All crystallizations of *Dd* NapA were set up 1-2 days before data collection. They were stabilized by adding the crystallization buffer containing either 15-30% (v/v) ethylene glycol for the native or 10 mM of the various ligand soaks (nitrate, perchlorate, cyanide) to the drop over a period of 10 minutes to two hours. The crystals were flash-frozen in liquid nitrogen after soaking in fresh mother liquor containing 15-30% (v/v) ethylene glycol (plus the appropriate ligand) as cryoprotectant for a few seconds. The data were collected at beamlines id14-eh1, id14-eh3, id14-eh4 and id23-eh1 at the ESRF (Grenoble, France) using a Quantum 4 charge-coupled device detector (ADSC). 100-180º of data were collected with a phi rotation, $\Delta\Phi$=1.0º, to give complete datasets for the data collected on the ID14 beamlines and 720 images for the SAD data on ID23 (collected above the iron edge with λ=1.77 Å) to give a highly redundant dataset (multiplicity 34.5). All data were processed using the programs MOSFLM [131] and SCALA [132] from the CCP4 suite (Collaborative Computational Project 4, 1994). The crystals belong to the trigonal space group $P3_121$ with cell constants (105-106) × (105-106) × (130-135) Å, with a single molecule in the asymmetric unit. Data collection and processing statistics are presented in Table III.2a.

For model building and refinement, the native structure of *Dd* NapA (pdb accession number 2NAP) was used to fit into each dataset after rigid-body refinement in REFMAC5 [133], treating each domain (Domain I: amino acid residues 4-61, 464-492 and 517-561; Domain II: 62-135, 347-463 and 493-516; Domain III: 134-346; and Domain IV: 562-723) as a rigid body. Iterative model building with O [134] and/or COOT [135] together with restrained refinement in REFMAC5 [133] initially and then with restrained refinement

including TLS (with each of the four domains treated as separate TLS entities) resulted in good final models as judged by the validation tools in COOT. These final models include amino acid residues 4-723 with their respective side chains, the catalytic molybdenum coordinated to two MGD cofactors, the [4Fe-4S] cluster, the water molecules, and ligands in the cases of cyanide and perchlorate. None of the above structures are thought to have the MES molecule in the solvent channel as depicted in the original native structure (2NAP). There is no anomalous sulfur signal for it in the SAD structure.

The three residues in the N-terminal (Ala, Asp and Asn) are highly disordered and were not included in the final models. Refinement statistics are presented in Table III.2b.

The determination of the sixth ligand (proposed to be a OH/OH_2 group in the reported structure of *Dd* NapA [79]) was carried out towards the end of refinement. The B-factor analysis is shown in table III.2c.

II.14 *Cupriavidus necator* NapAB Crystallization

Because of the small amount of pure protein available, crystallization conditions were explored by high-throughput crystallization screening using an automated TECAN crystallization robot (HTX Lab-EMBL, Grenoble, France). The conditions in which crystals were obtained are summarized below:

1. 0.1M acetate pH 4.5, 25% PEG 3350
2. 0.1M ammonium acetate, 0.1M bis-Tris pH 5.5, 17% PEG 3350
3. 0.1M succinate pH 7.0, 25% PEG 3350
4. 0.1M bis-Tris pH 5.5, 25% PEG 3350
5. 0.1M bis-Tris pH 5.5, 0.12M $MgCl_2$, 25% PEG 3350
6. 0.2M sodium formate, 20% PEG 3350
7. 0.1M bis-Tris pH 6.5, 25% PEG 3350
8. 0.1M bis-Tris pH 6.5,0.2M $MgCl_2$, 25% PEG 3350

9. 0.1M malic acid pH 7.0, 20% PEG 3350
10. 0.1M HEPES pH 7.5, 0.2M $MgCl_2$, 25% PEG 3350
11. 0.1M Tris-HCl ph 8.5, 25% PEG 3350
12. 0.05M zinc acetate pH , 20% PEG 3350
13. 0.1M bis-Tris pH 6.5, 20% PEG 5K MME
14. 0.1M bis-Tris pH 5.5, 0.2M ammonium acetate, 25% PEG 3350
15. 0.2M sodium/potassium tartrate, 20% PEG 3350
16. 0.1M HEPES pH 7.5, 30% Jeffamine ED 2001
17. 0.1M bis-Tris pH 6.5, 28% PEG 2K MME
18. 0.1M bis-Tris pH 6.5, 0.2M NaCl, 25% PEG 3350
19. 0.2M sodium malonate pH , 20% PEG 3350
20. 0.2 ammonium citrate pH , 20% PEG 3350

Best crystals were obtained under conditions 3, 4 and 7.

RESULTS

III.1.1 UV-Vis spectroscopy in *Dd* NapA: electronic spectrum and epsilons

Figure III.1 shows the UV-Vis spectrum of a pure protein solution (electrophoretic grade) of *Dd* NapA. The absorption spectrum is typical of a non-hemic iron-sulfur cluster containing protein exhibiting only shoulders at 320 nm and a broad absorbance band centered at around 400 nm. The extinction coefficient at 400 nm is 24 mM^{-1} cm^{-1}. Taking into account that the extinction coefficient of each [4Fe-4S] is expected to be around 16 mM^{-1} cm^{-1}, the ε_{400nm}=24 mM^{-1} cm^{-1} of *Dd* NapA suggests that the Mo*bis*-MGD has at least one electronic transition in this spectral region, likely a sulfur-to-molybdenum charge transfer band [136].

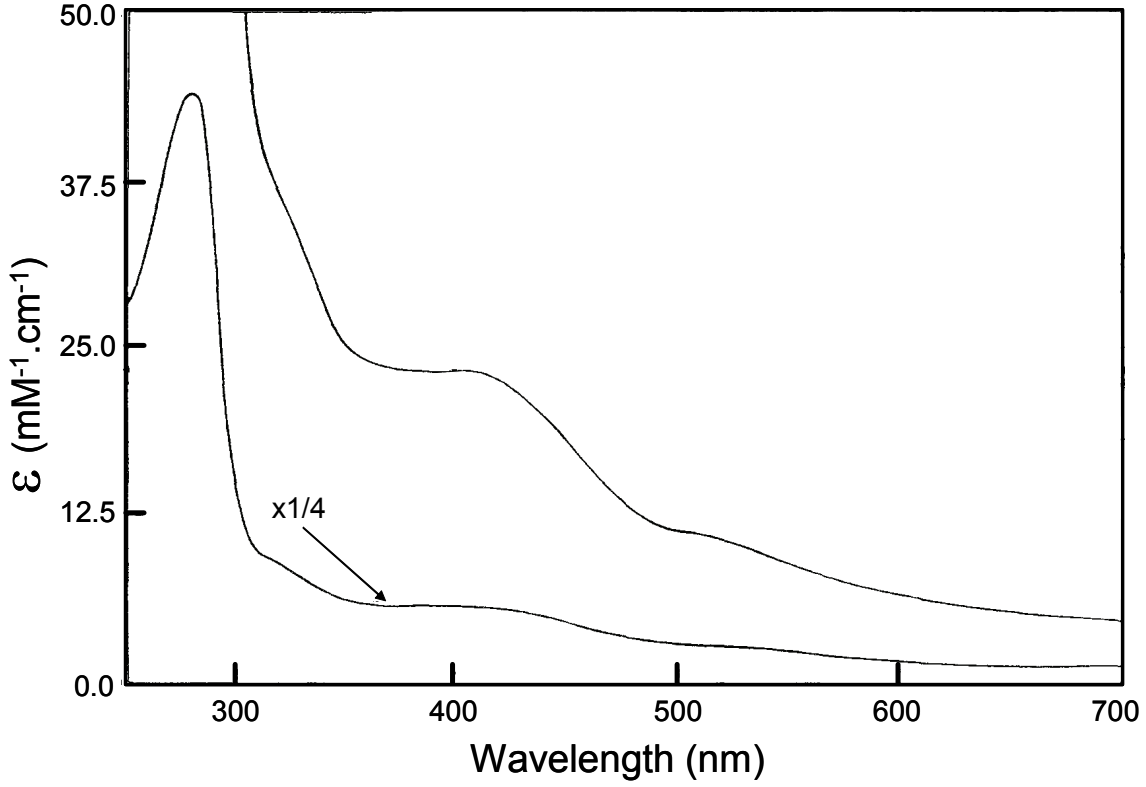

Figure III.1: UV-Vis absorption spectrum of pure *Dd* NapA.

The absorbance ratio $R_{400nm/280nm}$ of pure protein solution was found to be 0.12 for the purest samples.

III.1.2 Kinetic studies of *Dd* NapA

Nitrate reductase activity (right axis of Figure III.2) was found to be linear in a wide range of enzyme concentrations working in substrate saturating conditions (500 μM Nitrate and 5 mM methyl viologen) using the discontinuous method described in II.6.1. As seen in Figure III.2, the linearity extents until an enzyme concentration up to 500 nM, where the specific activity remains constant (left axis of Figure III.2).

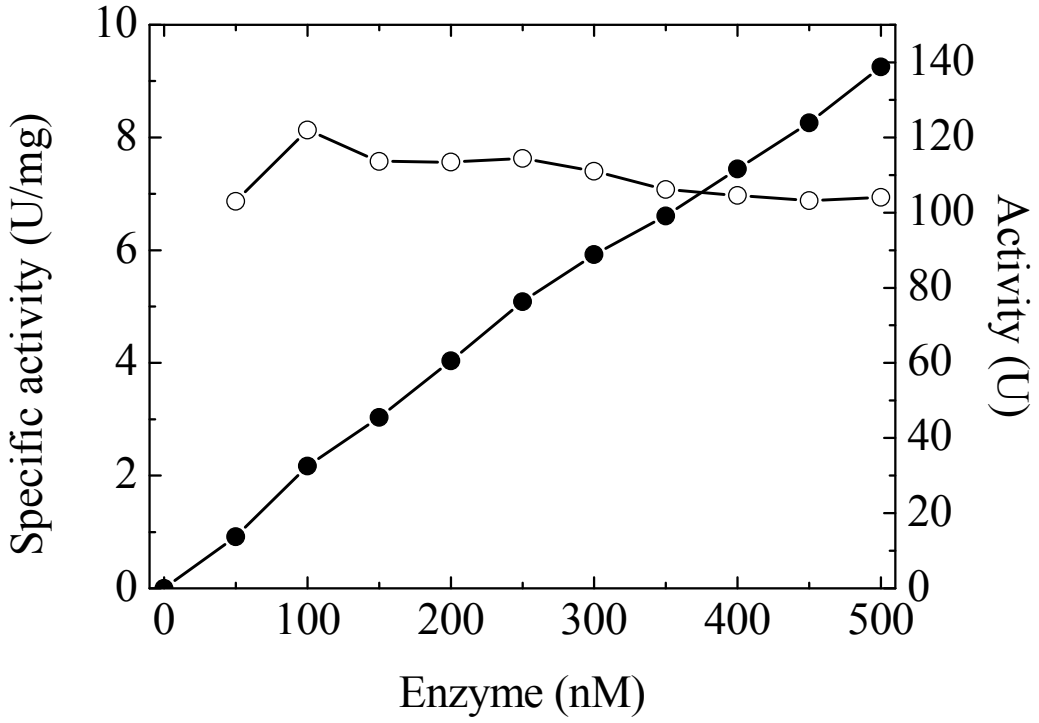

Figure III.2: Plot of specific activity (left axis, open circles) and total units (right axis, filled circles) as a function of the enzyme concentration. One unit of nitrate reductase activity (U) corresponds to one μmol of nitrite formed *per* minute.

The activity *versus* pH plot (Figure III.3) shows a typical assymetric bell-shaped behavior in which the optimal activity occurs at pH 7-8. The decays of the activity at high pH could be attributed not only to the typical enzyme denaturation but also to the low concentration of protons in solution, which are needed to complete the catalytic cycle (see scheme in section I.5). Similarly, the activity drops at low pH but this effect is ruled mainly by the instability (disproportionation) of the sodium dithionite in this pH region.

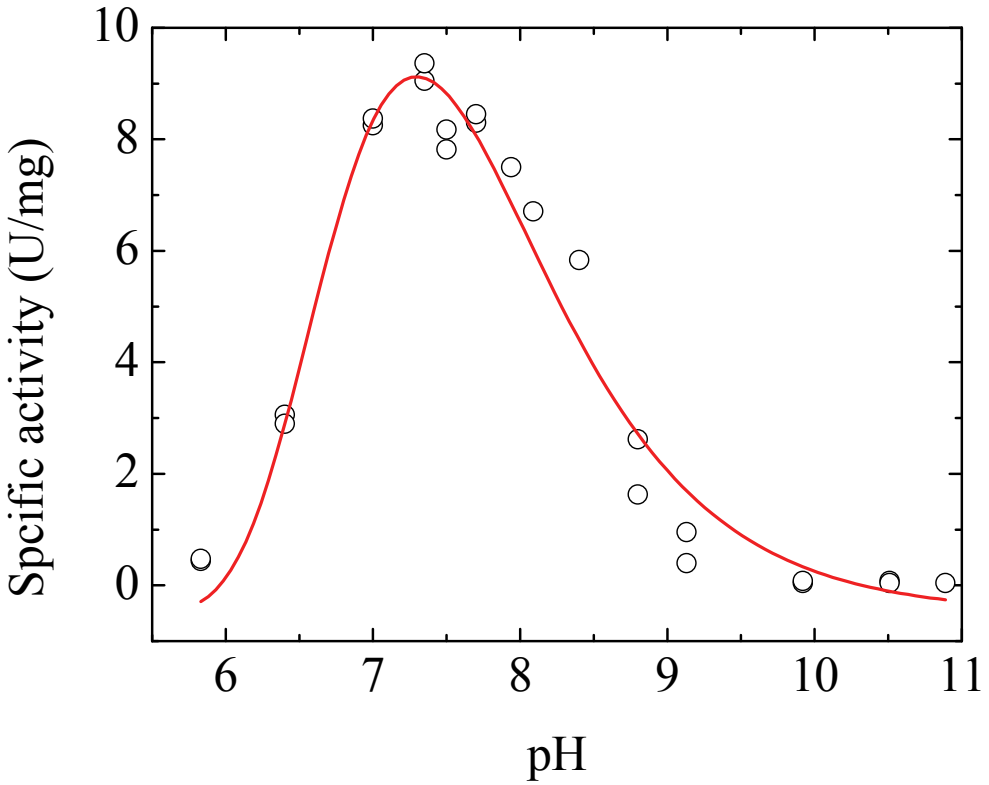

Figure III.3: Plot of specific activity as a function of the pH.

Steady-state studies were performed in several *Dd* NapA preparations purified from different batches. The kinetic behaviour of *Dd* NapA shows a large variability in terms of specific activity and K_m in the different batches, which did not allow a precise determination of properties such as substrate affinity and turn-over number. Therefore, a deep analysis of the kinetic properties of *Dd* NapA was not performed in the present thesis work.

The inhibitory effect of cyanide, azide, perchlorate and tiocyanate was studied varying the inhibitor concentration at constant substrate concentration. In contrast to that reported before [130], no differences were found in the assays performed either with Tris-HCl or with Phosphate Buffer.

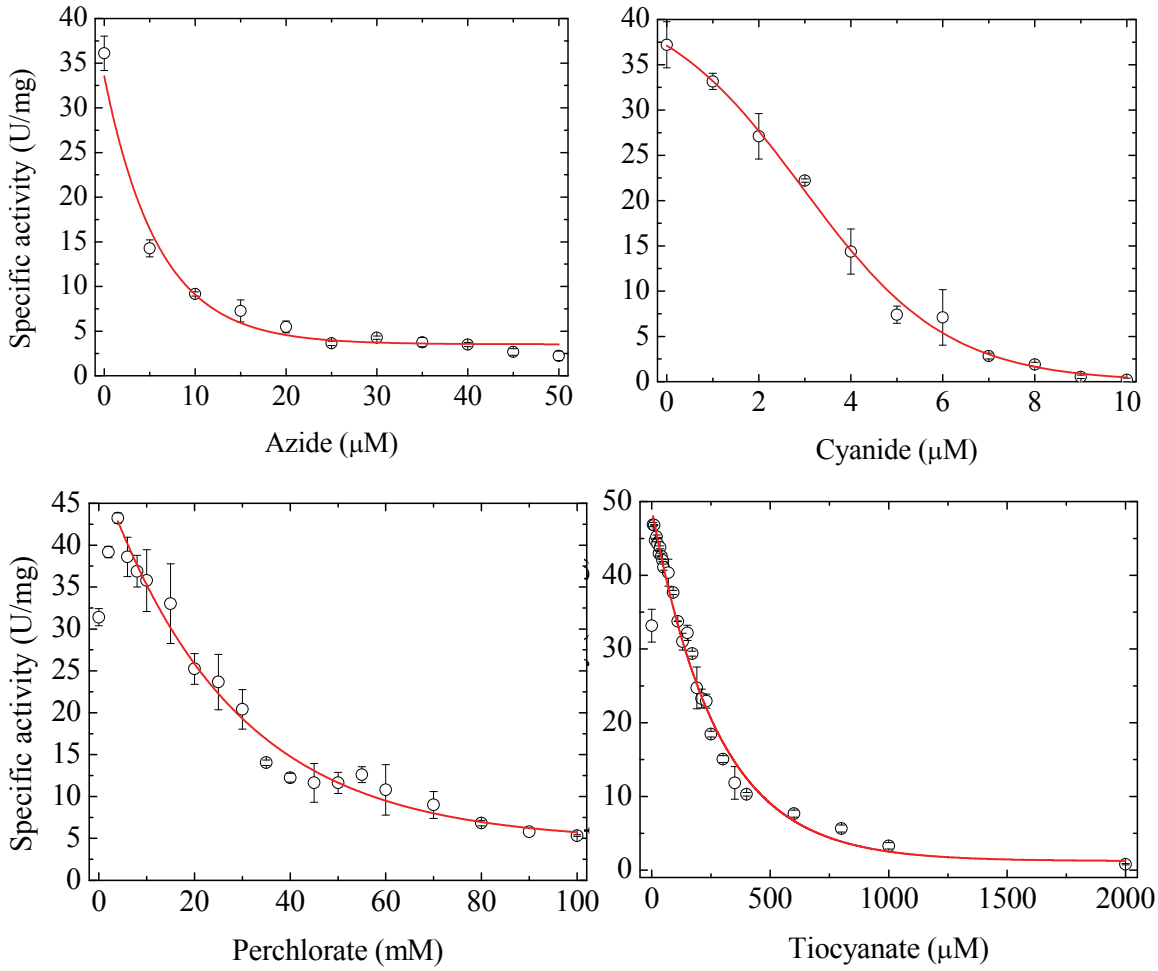

Figure III.4: Plot of enzyme inhibition by azide (up-left panel) and cyanide (up-right panel), perchlorate (down-left panel) and tiocyanate (down-right panel). The red lines are arbitrary fittings included to guide the eye.

As seen in many other nitrate reductases, both cyanide and azide are strong inhibitors and fully inhibit the activity at 10 μM and 30 μM, respectively (Figure III.4). Perchlorate and tiocyanate were found to be weaker inhibitors in comparison with cyanide and azide. As seen in figure III.4, both inhibitors display an activator effect at low concentration and fully inhibit the enzyme at concentration around 200 μM. Nevertheless, due to the impossibility of a complete steady-state analysis of the enzyme in the presence of inhibitors, no conclusions can be drawn with the present results.

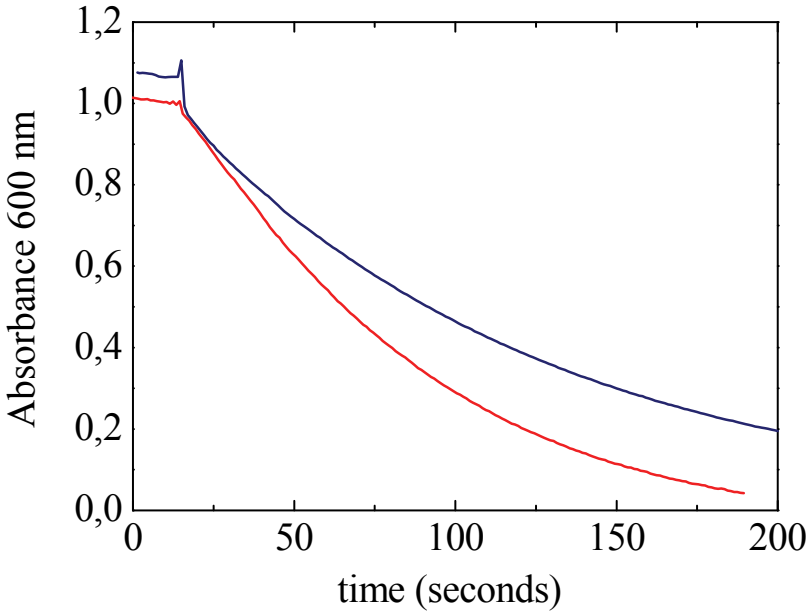

Figure III.5: Time-scan of methyl viologen oxidation recorded at 600 nm. Red and blue lines correspond to nitrate and chlorate reductase activity, respectively.

The ability of *Dd* NapA to reduce substrates other than nitrate was also tested using the continuous method. Surprisingly, the enzyme shows chlorate and bromate reductase activity which is not characteristic in periplasmic nitrate reductases but that has been widely described in the membrane bound nitrate reductases (Nar). Activities towards iodate, perchlorate, sulfite, arsenite, selenite or chromate were not detected. Other common substrate of Nars like arsenate, selenate and tellurate were not tested.

III.1.3 X-band Electron paramagnetic resonance of the Mo(V) species

EPR spectroscopy of as-prepared, dithionite-reduced and nitrate-oxidized samples. The EPR spectrum taken of the as-prepared enzyme (Figure III.6, spectrum a) shows a signal observable with no significant broadening up to 150 K (*resting* signal). Both temperature variation and *g*-values are compatible with Mo(V) ions (less than 0.05 spins *per* molecule). The broad component in the g_1 region suggests the presence of unresolved splitting(s) by non-exchangeable protons with solvent, likely from backbone or amino acid side chains, since this

signal does not alter upon D_2O exchange. This signal disappears after reduction with dithionite and cannot be restored after air oxidation.

Figures III.6, spectrum b and III.7, spectrum a show the spectra obtained after anaerobic reduction with dithionite (20-fold molar excess). The low-temperature spectrum (Figure III.7, spectrum a) is the superposition of the EPR signal associated with the [4Fe–4S]$^{1+}$ cluster and a less intense rhombic signal due to Mo(V) ions, which is observed without broadening up to 150 K and accounts for 0.15 spins *per* molecule (Figure III.6, spectrum b), which corresponds to the maximum value found in samples from several purification batches. This Mo(V) species (hereafter named *low potential* species) has a lower midpoint redox potential (less than -500 mV *vs*. the normal hydrogen electrode, NHE, see later) than the *resting* species. The *low potential* signal shows no significant differences when D_2O-exchanged samples are used but, in contrast to the *resting* signal and other EPR signals discussed later, no evidence for hyperfine coupling with nuclei with I=1/2 can be found. This signal has not been observed in other nitrate reductase and resembles the one called rhombic II in *Dd* Fdh (*g*-values in Table III.1), which is also obtained upon dithionite reduction [137].

Table III.1: EPR parameters of the Mo(V) species found in *Dd* NapA and related mononuclear molybdenum-containing enzymes. The values between parentheses for *Dd* NapA are the linewidths used in the simulation of the spectra shown in Fig. III.6. The hyperfine parameters (A) and linewidths are in Gauss. a) [93], b) [90], c) [137], d) [138], e) [124].

Enzyme	EPR signal	g_1	g_2	g_3	A_1	A_2	A_3
Dd NapA[a)]	*Low potential*	2.016 (5.5)	1.987 (5.5)	1.964 (5.5)	-	-	-
	High potential	2.019 (5.5)	1.988 (5.5)	1.960 (5.5)	-	-	-
	Nitrate	2.000 (4.4)	1.990 (3.6)	1.981 (3.4)	4.6	5.0	4.6
	Turn-over H / D	1.999 (4.5/11)	1.992 (5.0/7.0)	1.982 (6.0/8.0)	5.8/ -	6.5/ -	5.5/ -
	Cyanide	2.024 (4.5)	2.001 (4.0)	1.995 (4.0)	8.0	7.5	6.0
Pp NapAB[b)]	*High g [Resting]*	1.999	1.989	1.982	6.4/3.2	4.3	4.6
	High g [Nitrate]	1.997	1.990	1.982	6.5/2.2	6.0	5.0
	Very High g [Cyanide]	2.022	1.999	1.994	7.4	7.4	6.6
Dd Fdh[c)]	*Rhombic I*	2.019	1.988	1.963	-	-	-
	Rhombic II	2.009	1.984	1.951	-	-	-
Mf Fdh[d)]	*Reduced*	2.005	1.998	1.989	10.5	8.5	8.8
Ssp. NarB[e)]	*Air oxidized*	2.023	1.998	1.993	6.8	7.5	6.8

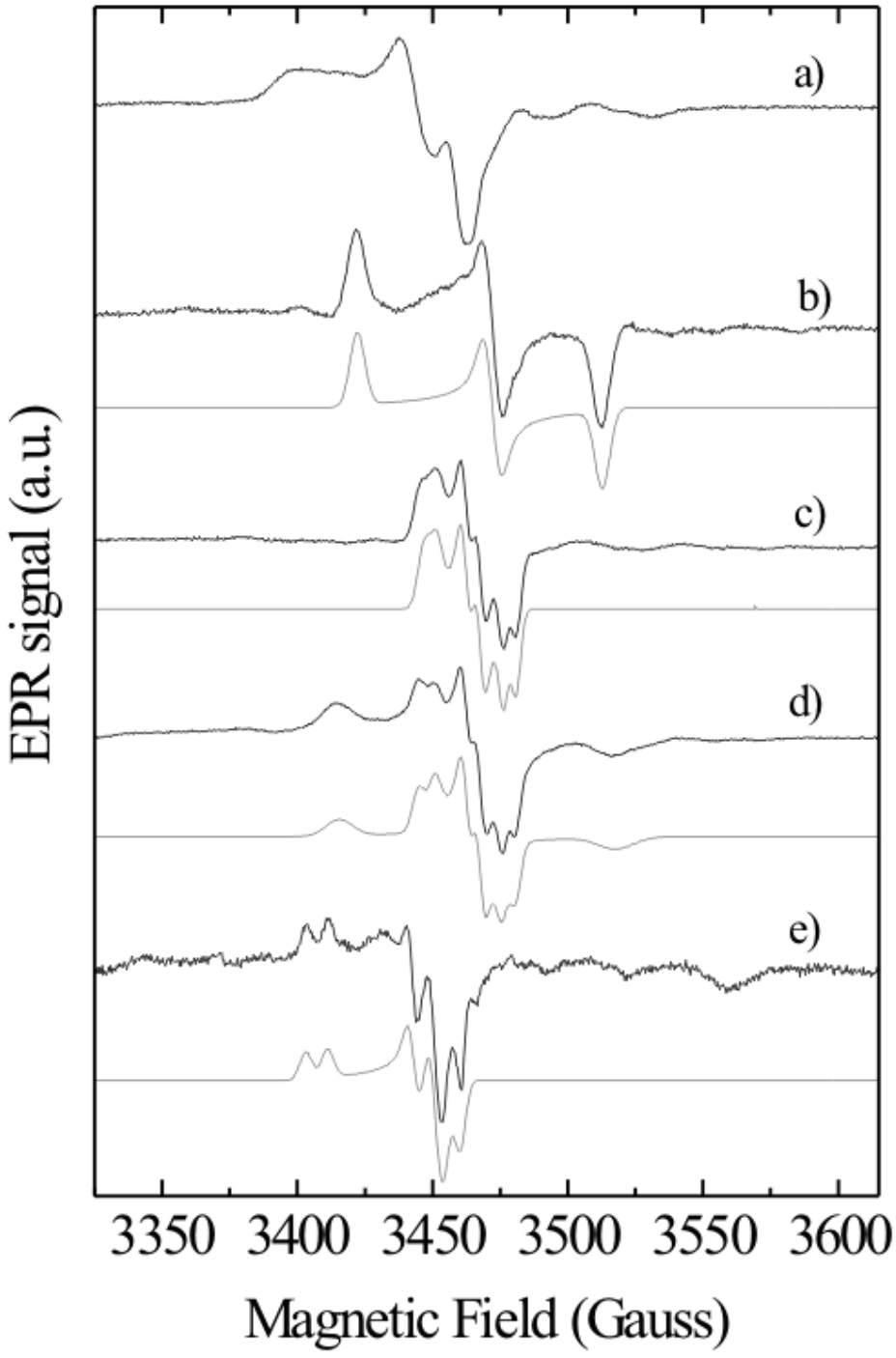

Figure III.6: Mo(V) EPR spectra obtained in *Dd* NapA at 100 K [93] together with simulation (grey lines). a) as-prepared sample, b) as-prepared sample reduced with 5 mM sodium dithionite, 4 c) idem b but after addition of 100 mM sodium nitrate, d) idem c but oxidized with air, and 5 e) idem b but added 20 mM cyanide and followed by air oxidation. EPR parameters used in simulations are given in Table III.1.

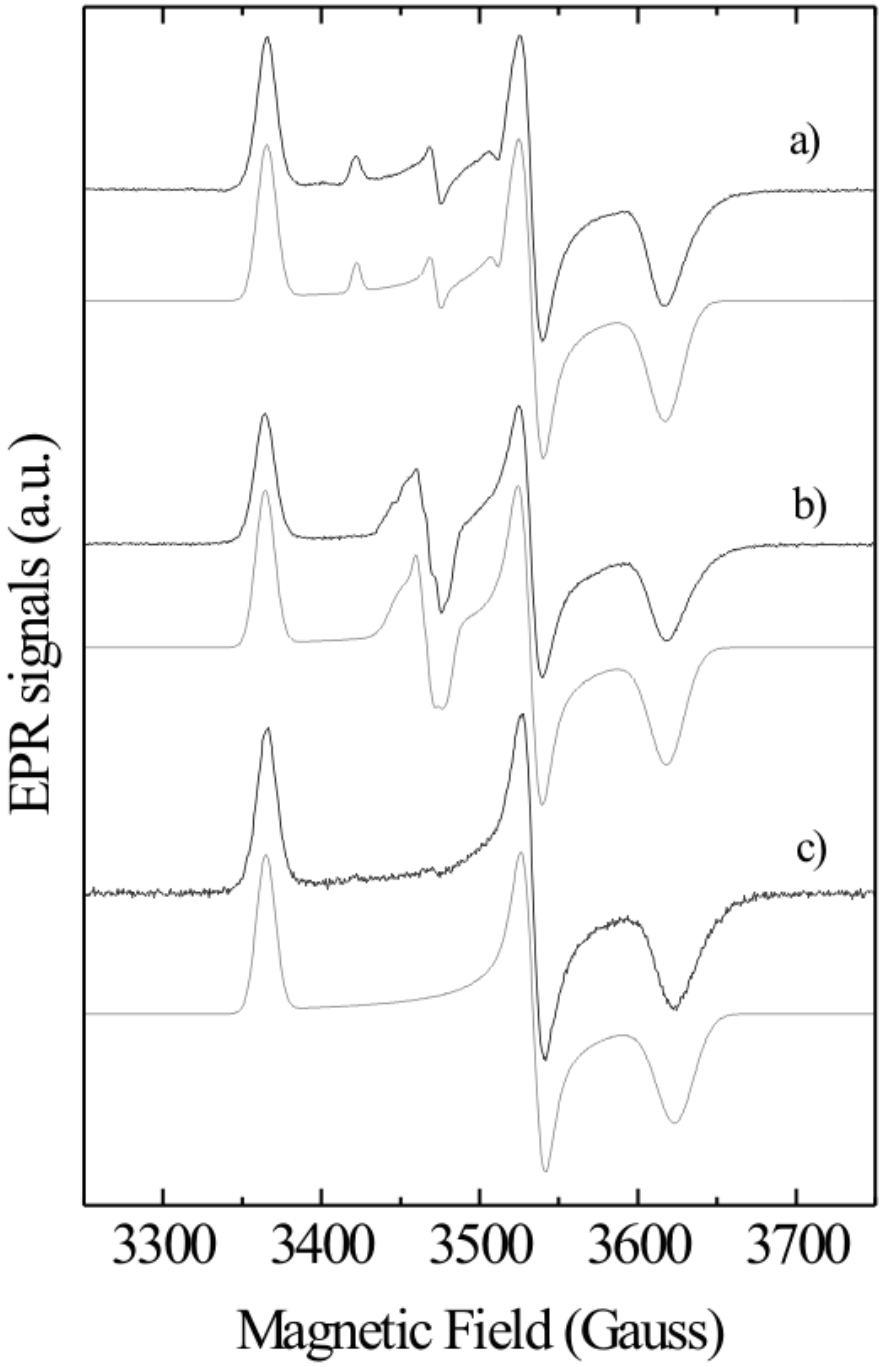

Figure III.7: Low temperature (25 K) EPR spectra of *Dd* NapA [93] samples together with simulation (grey lines) a) sample reduced with 5 mM sodium dithionite, b) idem a after adding 100 mM sodium nitrate, and c) idem a but containing 20 mM cyanide. The EPR parameters used in simulation of the FeS center signal were g_1=2.049 (12), g_2=1.952 (12) and g_3=1.906 (21) for spectra a and b (Linewidths in Gauss between parenthesis). The parameters for spectrum c were the same except g_3=1.903 (23). The parameters used for Mo(V) signals are given in Table III.1.

Addition of nitrate (500-fold molar excess) to the dithionite-reduced sample does not affect the FeS signal (Figure III.7, spectrum b), which is consistent with the fact that this cofactor acts as an electron transfer center. However, as reported before [41], nitrate addition in anaerobic conditions to dithionite-reduced samples of *Dd* NapA yields the Mo(V) EPR signal of Figure III.6, spectrum c. This signal shows hyperfine splitting with a species with nuclear spin I=1/2, which is not exchangeable with solvent.

The intensity of the nitrate signal increases with both the nitrate concentration and the incubation time, reaching a maximum of 40% of the total molybdenum after 40 min at a nitrate concentration of 100 mM. The same spectrum was also obtained using chlorate instead of nitrate and after air oxidation of a dithionite-reduced sample. The latter has a lower intensity compared with that obtained with nitrate oxidation (less than 10%). Although nitrate is not essential to produce this signal, it will be called the *nitrate* signal (EPR parameters in Table III.1).

Exposure to air of a sample showing the *nitrate* signal oxidizes the FeS center to the diamagnetic state $[4Fe–4S]^{2+}$ but leaves the intensity of the *nitrate* signal unaffected, suggesting that the resulting Mo(V) species is stabilized after nitrate addition. As seen in Figure III.6 spectrum d, this procedure also produces an additional rhombic Mo(V) signal, which will be named *high potential* as it is produced in the presence of oxygen (redox potential approximately +200 mV *vs*. NHE), and is identical to the rhombic I signal reported in *Dd* Fdh (*g*-values in Table III.1) [137]. However, this signal was not observed in all the cases analyzed and its observation depends on the batch of enzyme utilized in each experiment.

EPR properties of inhibited Dd NapA. The EPR properties of *Dd* NapA were evaluated in the presence of cyanide, azide, and perchlorate. The inhibitory effect of cyanide and azide was reported in [130], whereas perchlorate is a weak inhibitor (this work). Cyanide addition to as-prepared samples of *Dd* NapA does not produce visible changes in the *resting*

Mo(V) (not shown). In contrast, cyanide addition to dithionite-reduced samples followed by reoxidation in air led to the nearly axial signal shown in Figure III.6 spectrum e, which accounts for less than 0.03 spins *per* molecule. The same signal was obtained when the sample was exchanged into D_2O, and in samples treated with $KC^{15}N$ (I_N=1/2) and $K^{13}CN$ (I_C=1/2). Furthermore, cyanide addition (KCN, $KC^{15}N$, and $K^{13}CN$) produces only a slight shift to the right of the g_3 value of the FeS signal (Figure III.7, spectrum c), which could be originated from indirect conformational changes induced by the cyanide molecule since the EPR data suggest that cyanide is not coordinated to the FeS cluster. Attempts to develop a Mo(V) EPR signal by treating both as-prepared and dithionite-reduced samples with 100-fold molar excess of either sodium azide or potassium perchlorate and followed by air oxidation failed to show an EPR signal associated with Mo(V) species.

III.1.4 Spectropotentiometric redox titration

In order to evaluate the redox properties of the different Mo(V) species and the FeS center, EPR-mediated redox titrations were performed in the potential range from 150 mV (a value where the electrochemical potential stabilizes without dithionite addition) to -500 mV. Figure III.8 shows the relative intensity of the *low potential* species and the FeS center EPR signal as a function of the electrochemical potential of the solution. The *resting* signal, which is detected in the as prepared samples, is not observed in this experiment. A least-squares fit to the data of the FeS signal with a Nernstian function (n=1) yielded E=-390 mV (*vs*. NHE). This value is unusually low for Naps, which usually have FeS centers with redox potentials around -200 mV [83, 90, 124]. The redox potentials of the *low potential* species could not be precisely determined owing to the lack of data below -500 mV (Figure III.8).

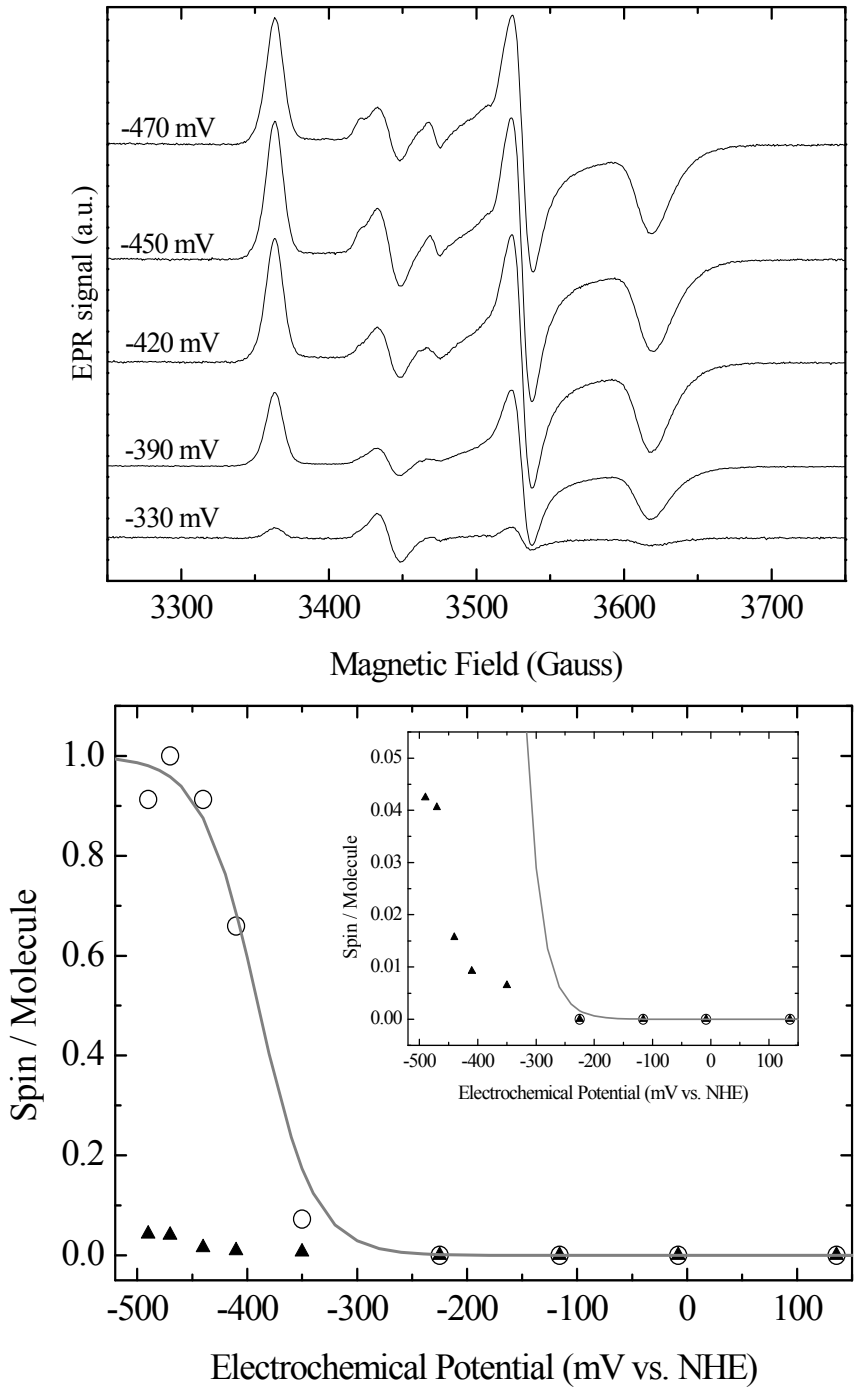

Figure III.8: Redox titrations of *Dd* NapA at room temperature monitored by EPR. Upper panel: low temperature spectra recorded at the different electrochemical potentials. Lower panel: Circles: FeS signal; Triangles: *low potential* Mo(V) signal. See II.11 for details. In the lower panel, the inset shows the same data but in a different scale.

The intensity of the *low potential* signal accounted for approximately 0.05 spins *per* molecule at the lowest potential reached in this experiment. This value is far from the value of

approximately 0.3 spins *per* molecule that should be obtained in the hypothetical situation of identical midpoint redox potentials for the couples Mo(VI)/Mo(V) and Mo(V)/Mo(IV) (it was assumed to be -500 mV for both redox couples). This indicates that the Mo(V)/Mo(IV) redox pair has an even more negative redox potential, which confirms that the molybdenum cannot be completely reduced to Mo(IV) on dithionite reduction.

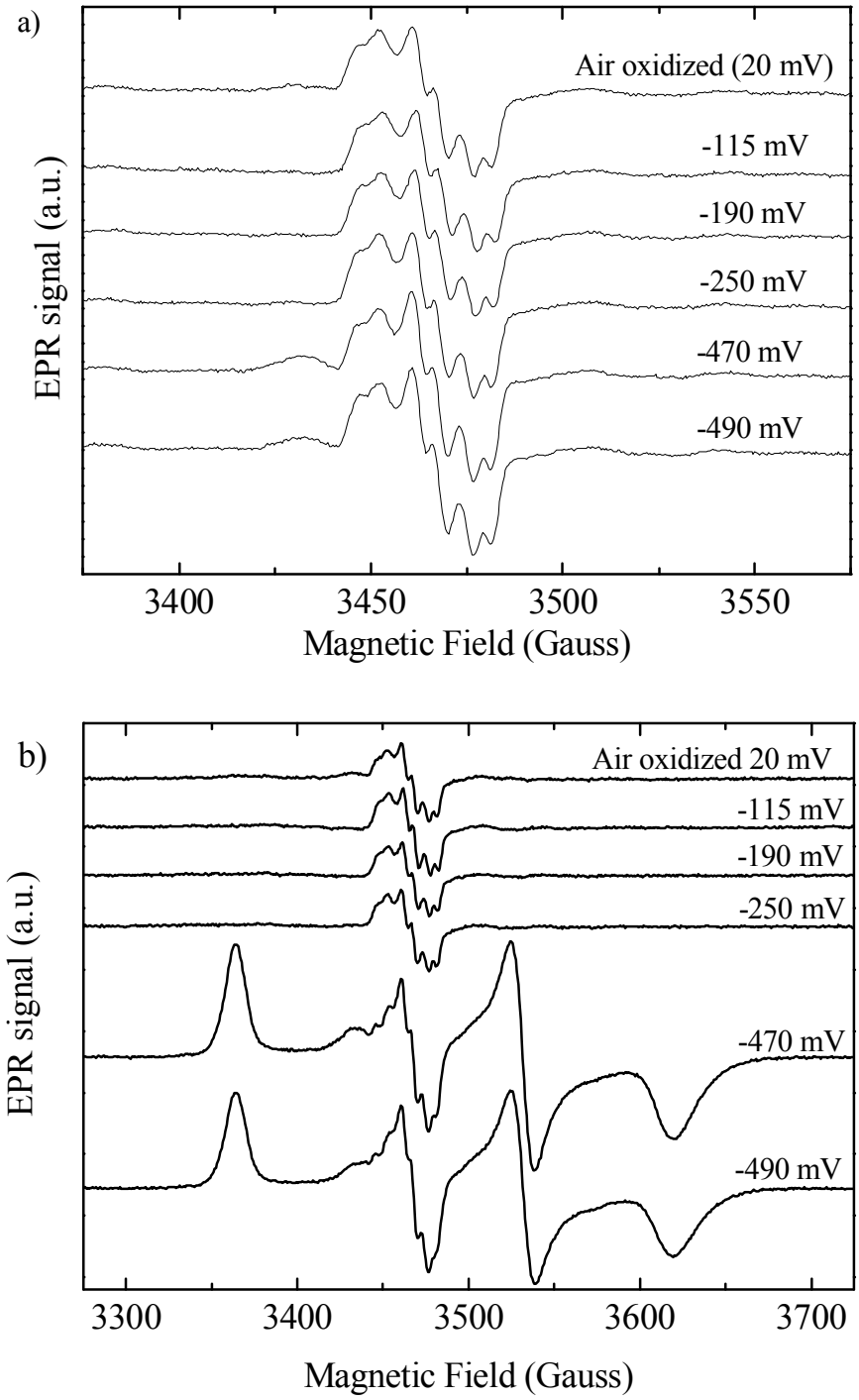

Figure III.9: EPR spectra obtained at different redox potential of a *Dd* NapA sample containing 100 mM of potassium nitrate. Panel a) and b) show the spectra recorded at 100 K and 25 K, respectively.

In order to evaluate the redox potential of the *nitrate* species, the redox titration was carried out on a sample containing a 500-fold molar excess of nitrate. Previously, the sample was reduced to a potential of approximately -500 mV, and was then incubated with nitrate for 40 min to produce the *nitrate* signal with its higher intensity, and was then reoxidized with air. This sample, which shows the *nitrate* signal, was titrated again with dithionite as explained before. Again, the same redox potential was obtained for the FeS center (Figure III.9), but the *nitrate* signal showed no significant changes either in intensity or lineshape at 100 K in the range of electrochemical potentials evaluated, which indicates that the *nitrate* signal is not associated with a redox-active species in the range from 200 to -500 mV. A similar conclusion can be obtained from the analysis of the intensity of the Mo(V) signals at 25 K. Note that the spectra at the potentials where the FeS centers are paramagnetic (e.g., -490 mV) show a slight change in the lineshape of the *nitrate* signal with respect to those obtained at higher potentials (e.g., 20 mV), indicating a weak magnetic coupling between Mo(V) and $[4Fe\text{-}4S]^{1+}$, never reported before in a nitrate reductase.

III.1.5 The *Turnover* signal

In contrast to *Pp* NapAB [90], *Dd* NapA has no activity when incubated in the presence of dithionite as the sole electron donor and the enzyme needs reduced MV to be catalytically competent [93]. As explained in section II.6.2, in a typical kinetic experiment the enzyme is reacted with MV reduced with sodium dithionite and then, the reaction is started by adding nitrate. Since the reduction of MV can be alternatively made by adding Zn(0) stones, the EPR experiment was performed by reducing *Dd* NapA with Zn(0)-reduced MV to avoid the reaction of the metal centers with the excess of dithionite or their oxidation products. Figure III.10 shows the spectra obtained after redox-cycling the enzyme using this procedure.

The EPR spectrum of the MV-reduced sample is dominated by a reduced dye radical signal with g=2.004 (Figure III.10, spectrum a). Addition of a 500-fold molar excess of nitrate

oxidizes the MV, which becomes colorless, and yields the EPR spectrum shown in Figure III.10, spectrum b, which accounts for 0.5-0.6 spins/protein molecule. This spectrum is obtained by freezing the sample immediately after nitrate consumes all the reduced-MV. It shows *g*-values and temperature variation typical of Mo(V) ions and the signal could be reasonably well simulated assuming hyperfine coupling with a ^{14}N nucleus (I=1, not shown).

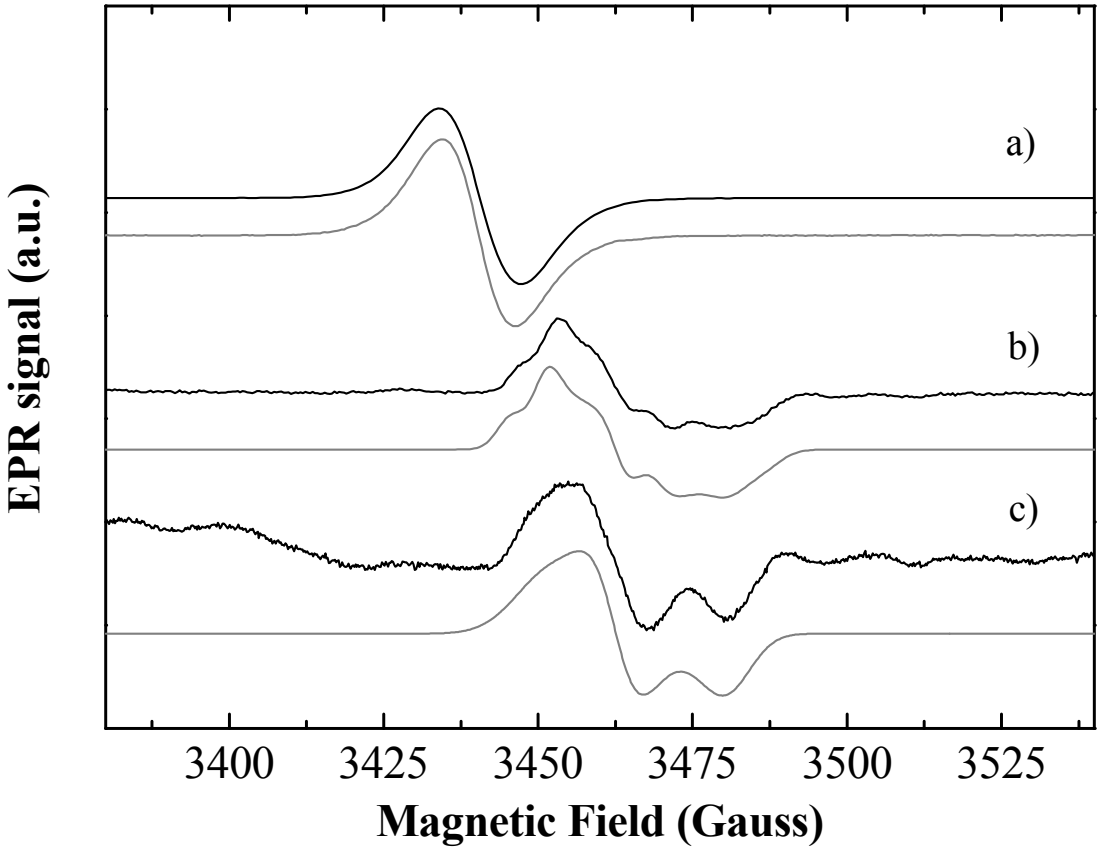

Figure III.10: Mo(V) species obtained in turnover conditions. a) Enzyme solution with 5 mM Zn-reduced methyl viologen, b) idem a) reacted with 100 mM potassium nitrate, c) idem b) but in D_2O exchanged solutions.

Air oxidation of this sample led to the disappearance of the EPR signal, indicating that this Mo(V) species is redox active, in contrast to the *nitrate* signal. Re-reduction of the MV with dithionite in a substoichiometric amount with respect to MV yields again the same signal, because of the excess of nitrate present in the mixture. As this signal is obtained under catalytic conditions, it will be called the *turnover* signal. Furthermore, no signals attributable to the paramagnetic $[4Fe–4S]^{+1}$ were detected in this redox cycle of the enzyme.

In order to confirm whether the splitting of the *turnover* signal corresponds to the N atom of the nitrate molecule, the same experiment was conducted with ^{15}N labeled sodium nitrate (I_N=1/2). No differences were found between the spectrum obtained with $K^{14}NO_3$ (potassium nitrate with natural abundance isotope composition 99.64% ^{14}N) and spectrum obtained with $K^{15}NO_3$ (^{15}N enriched potassium nitrate; 99%) discarding the possibility that these signals are associated with a Mo(V)–nitrate complex (not shown). As *Dd* NapA shows a significant chlorate reductase activity the same experiment was conducted using potassium chlorate ($KClO_3$) instead of the nitrate. Again, the same spectrum was obtained (Figure III.10, spectrum b), supporting the fact that the *turnover* signal is not produced by a Mo(V)-nitrate complex. This is also supported by the fact that no hyperfine splitting with the Cl nucleus (I=3/2) was detected.

When the same experiment was conducted with D_2O-exchanged samples using $K^{14}NO_3$ (Figure III.10, spectrum c) the Mo(V) signal shows larger linewidths and non solved hyperfine structure. The *g*-values used to simulate this signal are given in Table III.1. These *g*-values were used to simulate the spectrum b of Figure III.10, considering in addition isotropic hyperfine splitting produced by two interacting nucleus with I=1/2. This experiment confirms that the *turnover* species does not correspond to a Mo(V)-substrate complex, and suggest that one of the ligands to Mo(V) ion is a water molecule.

III.1.6 Spectropotentiometric redox titration using Zn-reduced Methyl Viologen as reducing agent

The experiment described above do not showed the presence of the paramagnetic $[4Fe\text{-}4S]^{1+}$ cluster. To study the redox behavior of both Mo-*bis*MGD and FeS cofactors in turnover conditions, a redox titration was conducted using Zn-reduced MV as reductant instead of dithionite. Since the solution of reduced methyl viologen is more reactive towards oxygen than sodium dithionite solutions, all buffers, including the enzyme solution, were

oxygen-degassed with argon and introduced into the anaerobic chamber overnight to ensure that all solutions are oxygen-free. The methyl viologen solution (25 mM) was reduced with Zn(0) stones, which was used to drop the electrochemical potential.

Dd NapA samples (200 μL) were taken for EPR spectroscopy in the potential range of +100 to -400 mV (*vs*. NHE), where the latter value was the lowest potential reached under this experimental conditions. EPR spectra recorded in the temperature range 4-100 K revealed no EPR signal attributable to neither the FeS cluster nor the Mo(V) ion, indicating that Zn-reduced MV do not reduce the metal cofactors of *Dd* NapA.

The addition of nitrate to the sample poised at -400 mV lead to the concomitant oxidation of the methyl viologen, and the electrochemical potential of the solution rises up to -150 mV, value where the *turnover* signal is developed. The additions of higher excess of nitrate do not change the electrochemical potential significantly.

III.1.7 X-ray crystallography studies in *Dd* NapA

Single crystals for X-ray crystallography were prepared from as-prepared samples and from the EPR samples giving the *nitrate* and *cyanide* signals and the sample incubated with perchlorate. Although several datasets were obtained for each sample, only the best in terms of resolution and quality were fully analyzed and are discussed here. The arrangement of the several molybdenum environments were determined and correlated with their respective EPR spectrum.

The crystals were obtained using the vapor diffusion hanging drops method using the same conditions as for the as-prepared protein structure [78, 79]. The structures of crystals thus obtained were labeled according to the Mo(V) species detected by EPR, except for the perchlorate sample that did not yield any Mo(V) signal. The habits of the crystals show cubic shapes instead of the needles obtained in the original report of the structure [78, 79].

Table III.2: Statistics on a) data collection statistics, b) structure refinement and c) analysis of the sixth ligand of the molybdenum ion. Values between parentheses in a) correspond to the highest resolution shell. $R_{merge}= \Sigma_h \Sigma_i |I(h,i) - <I(j)>| / \Sigma_h \Sigma_i I(i,h)$, where I(i,h) is the intensity of the i^{th} measurement of reflection h and <I(h)> is the mean value of I(h,i) for all I measurements. $R_{work} = \Sigma||F_{calc}| - |F_{obs}|| / \Sigma|F_{obs}| \times 100$, where F_{calc} and F_{obs} are the calculated and observed structure factor amplitudes, respectively. R_{free} is calculated for a randomly chosen 5% of the reflections for each dataset.

a) Data collection statistics						
Dataset		**Native**	**Nitrate**	**Cyanide**	**Perchlorate**	**Native 2**
Resolution range (Å)			53.00-2.4	54.3-2.4	46.1-1.9	76.0-2.3
Wavelentgh (Å)			0.934	0.934	0.931	1.771
Space group		$P3_121$	$P3_121$	$P3_121$	$P3_121$	$P3_121$
Cell parameters	*a* (Å)	106.26	105.21	106.24	106.57	106.19
	b (Å)	106.26	105.21	106.24	106.57	106.19
	c (Å)	134.90	130.68	134.63	135.48	135.10
Reflections	Total		151758 (16057)	227703 (32970)	454081 (15580)	1453461 (211083)
	Unique	66804	31747 (4320)	37165 (5344)	65218 (6059)	42181 (6032)
Multiplicity			4.8 (3.7)	6.1 (6.2)	7.0 (2.6)	34.5 (35.0)
Completeness (%)			99.0 (93.6)	100 (100)	93.5 (60.4)	99.6 (98.8)
<I/σ(I)>			6.3 (1.0)	13.6 (2.1)	10.0 (0.8)	28.2 (4.0)
R_{merge}			26.7 (113.9)	10.0 (72.1)	24.1 (133.2)	14.7 (98.9)
Wilson B-factor ($Å^2$)			36.63	49.16	16.66	40.35
b) Structure refinement						
Resolution (Å)		1.9	2.4	2.4	2.0	2.2
Reflections used			29497	35628	57324	42713
R_{work} (%)			15.7	17.3	19.2	15.1
R_{free} (%)			25.0	24.6	25.0	21.0
Numbers of waters			705	607	750	813
Number of ligands			0	1	2 LCP	0
c) B-factor analysis on the Mo sixth ligand						
Wilson B-factor ($Å^2$)			36.63	49.16	29.76	40.35
[4Fe-4S] range			24.9-31.5	36.3-40.2	24.2-25.9	30.9-39.8
S_δ Met_{308}			12.5	34.1	18.4	27.7
S_γ Cys_{307}			18.3	33.0	22.9	31.6
S_{12} MGD_{811}			24.6	35.9	22.9	27.9
S_{13} MGD_{811}			19.3	32.5	17.4	25.2
S_{12} MGD_{812}			26.4	37.8	20.6	30.5
S_{13} MGD_{812}			20.6	38.9	25.7	30.3
S_γ Cys_{140}			21.7	40.5	24.6	32.8
Mo			25.9	38.9	24.4	29.4
S				47.6	24.3	24.9
HOH				27.6	4.12	5.5
-C=N				31.3/32.6		
-N=C				29.7/34.2		

This difference cannot be attributed to either the presence of any of the reagents or the purification batch, since the same crystal shapes were obtained in several trials of both as-prepared and reacted enzyme samples from different batches. The statistic of data collection and structure refinement of the best dataset obtained for each sample are summarized in table III.2. Despite the different crystal shapes, it can be seen that the enzyme crystallizes in the same space-group $P3_121$, with nearly identical cell parameters when compared with the ones for the crystals used to solve the as-prepared protein structure (Table III.2a).

The single-crystal structure corresponding to the *nitrate* signal, solved at 2.4 Å resolution, show Mo sites with no significant differences respect to the as-prepared protein structure. The molybdenum core can be reasonably well simulated with five sulfur atoms, four from both dithioline ligands and one Sγ from Cys_{140}, and one hydroxo/water ligand (Figure III.11). This is in disagreement with the coordination sphere deduced from the EPR experiments, which indicates that non solvent-exchangeable groups (*i.e.* OH/OH_2) are coordinated to the Mo(V) ion.

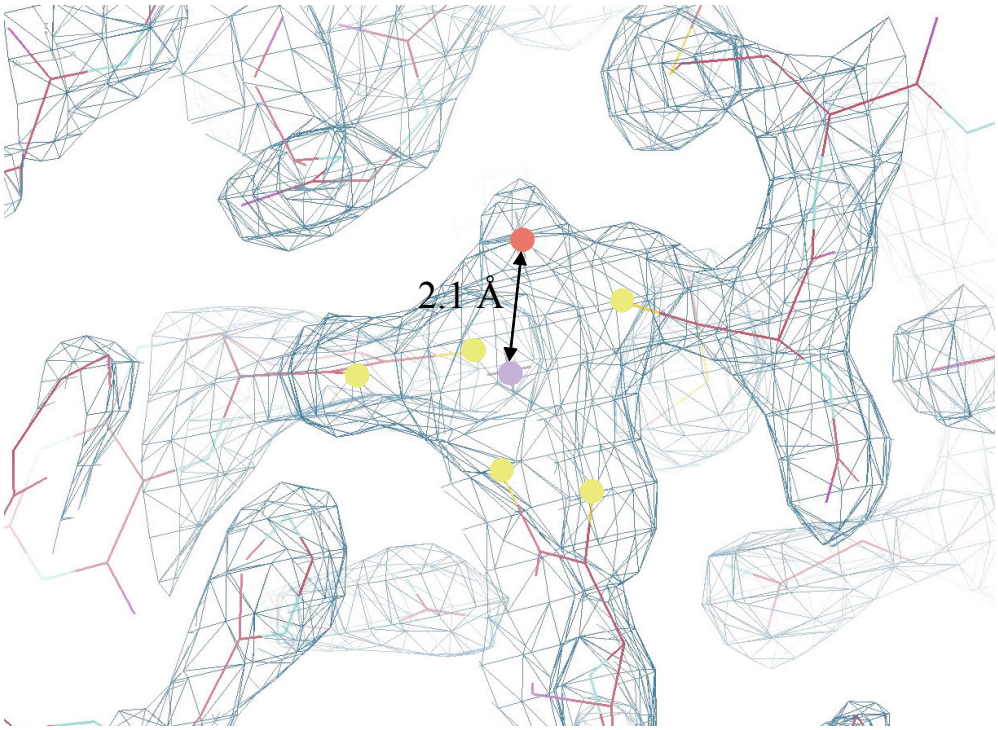

Figure III.11: *nitrate* species 3D representation of the Mo-site of *Dd* NapA superimposed with the electron density map contoured at 3.0 σ.

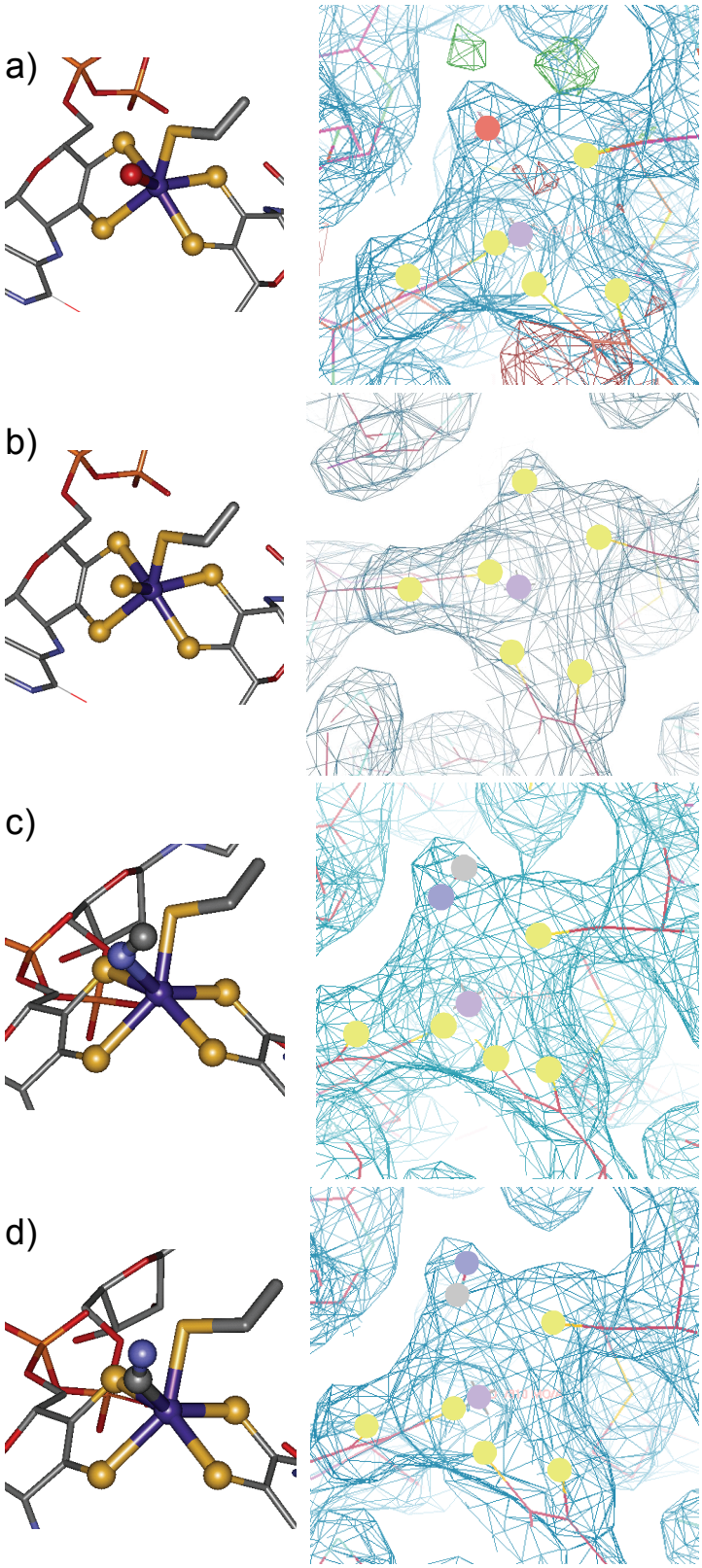

Figure III.12: *cyanide* species 3D representation of the Mo-site of *Dd* NapA as balls and sticks and superimposed with the electron density map contoured at 3.0 σ. The sixth coordination position of the Mo ion was modeled with: a) oxygen, b) sulfur, c) cyanide bound through the nitrogen, and d) cyanide bound through the carbon. Green and red surfaces in a) represent positive and negative F_O-F_C peaks, respectively.

The single-crystal structure corresponding to the *cyanide* signal was solved also at 2.4 Å resolution. No differences in the global fold of the amino acid chain were detected as RMSD is 0.20 Å for 720 C_α atoms and 0.22 Å for 2880 backbone atoms. However, some differences were detected with respect to the *as-prepared* structure at the first coordination sphere of the molybdenum. In this case, the Mo site can be well modeled with four sulfur atoms from the two pterins moieties and Sγ from Cys_{140}, but there is a positive F_O-F_C peak when an OH/OH_2 ligand is placed at the sixth coordination position (Figure III.12a, green surface). This model is improved in terms of fitting of the electronic density when a sulfur atom is placed at the sixth coordination position (Figure III.12b), but results in an increased B-factor (Table III.2c) of the ligand when compared to the B-factor of the Mo ion. The best fitting is obtained when a cyanide molecule is placed at the sixth coordination position and this result does not significantly change by bonding the cyanide molecule to the Mo ion through either the carbon or the nitrogen (Figure III.12c and d). Although the model is improved with respect to the former models, as concluded from the B-factors obtained for both cases (Table III.2c), these results are in disagreement with the EPR results, which suggest that cyanide is not coordinated to the Mo ion. X-ray data taken at better resolutions are necessary to solve these discrepancies.

The sample with perchlorate, which is EPR silent, was crystallized and the structure solved at 2.2 Å resolution and then improved to 2.0 Å through modeling. This dataset is the best one collected for a reacted sample in terms of resolution. The global fold was found to be essentially the same when compared to the as-prepared structure since RMSD is 0.29 Å for 720 C_α atoms and 0.30 for 2880 backbone atoms. Two huge positive F_O-F_C peaks (Figure III.13b) confirm that something is present in the funnel cavity blocking the pathway from surface to the molybdenum active site. The modeling of this electron density with water molecules gives an inappropriate model as judged by the B-factors obtained. However, when

perchlorate ions are placed in these electron densities (Figure III.13a) the model is highly improved as judged by B-factors and F_O-F_C analysis.

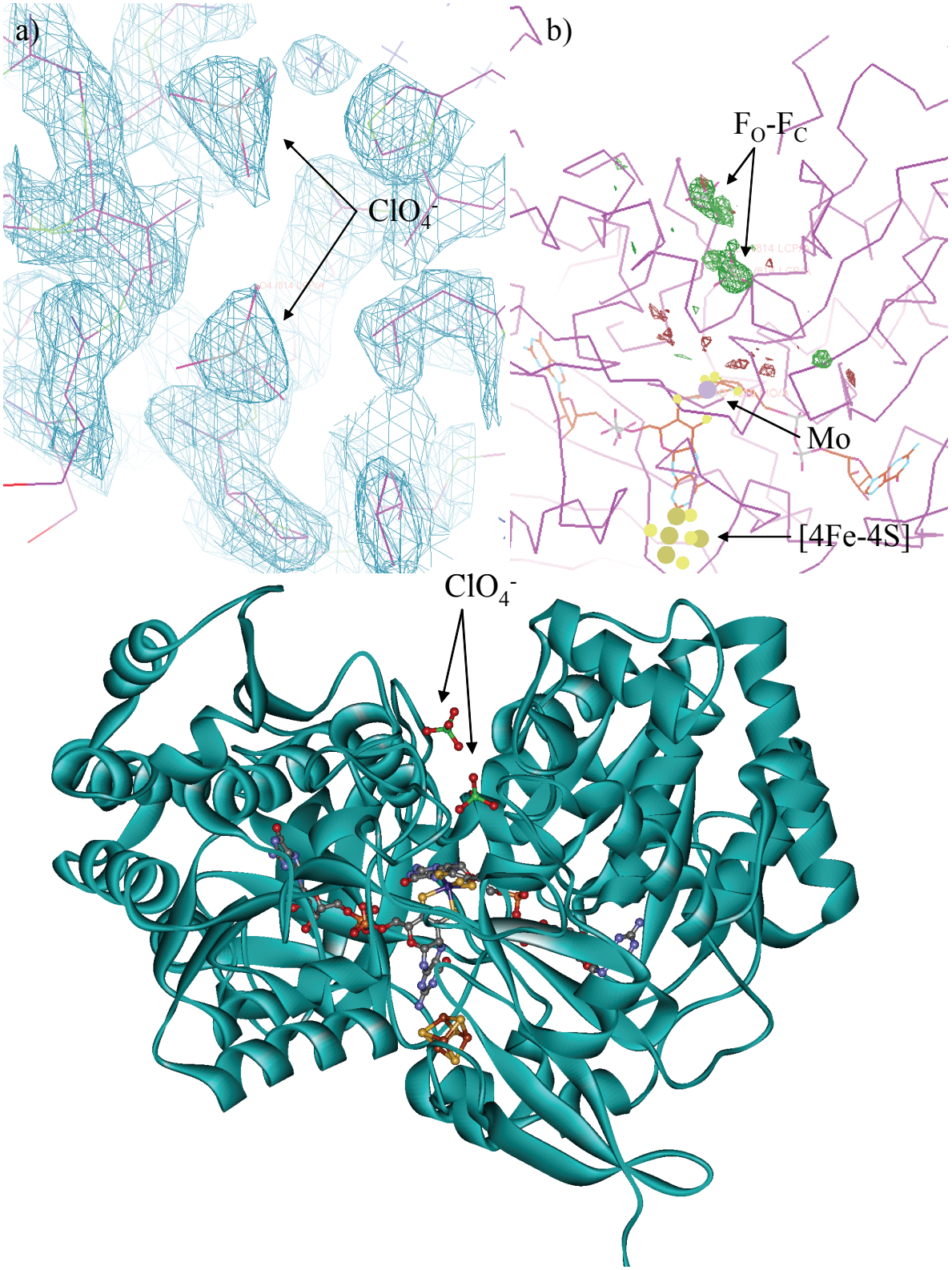

Figure III.13: a) representation of the ClO_4^- anions superimposed with the electron density map contoured at 3.0 σ, b) representation of the ClO_4^- anions superimposed with the F_O-F_C map before modeling the ClO_4^-, and c) representation of the global structure of *Dd* NapA with ClO_4^- anions blocking the funnel-like cavity.

This suggests that the perchlorate molecule cannot enter deeper in this cavity and the inhibition mechanism would take place by blocking the entry of the substrate to the catalytic site (Figure III.13c).

In order to find sulfur SAD (Single-wavelength Anomalous Dispersion) signals, a sample with as-prepared protein was also cristallized and several datasets were collected using a wavelength above the iron-edge (see table III.2a).

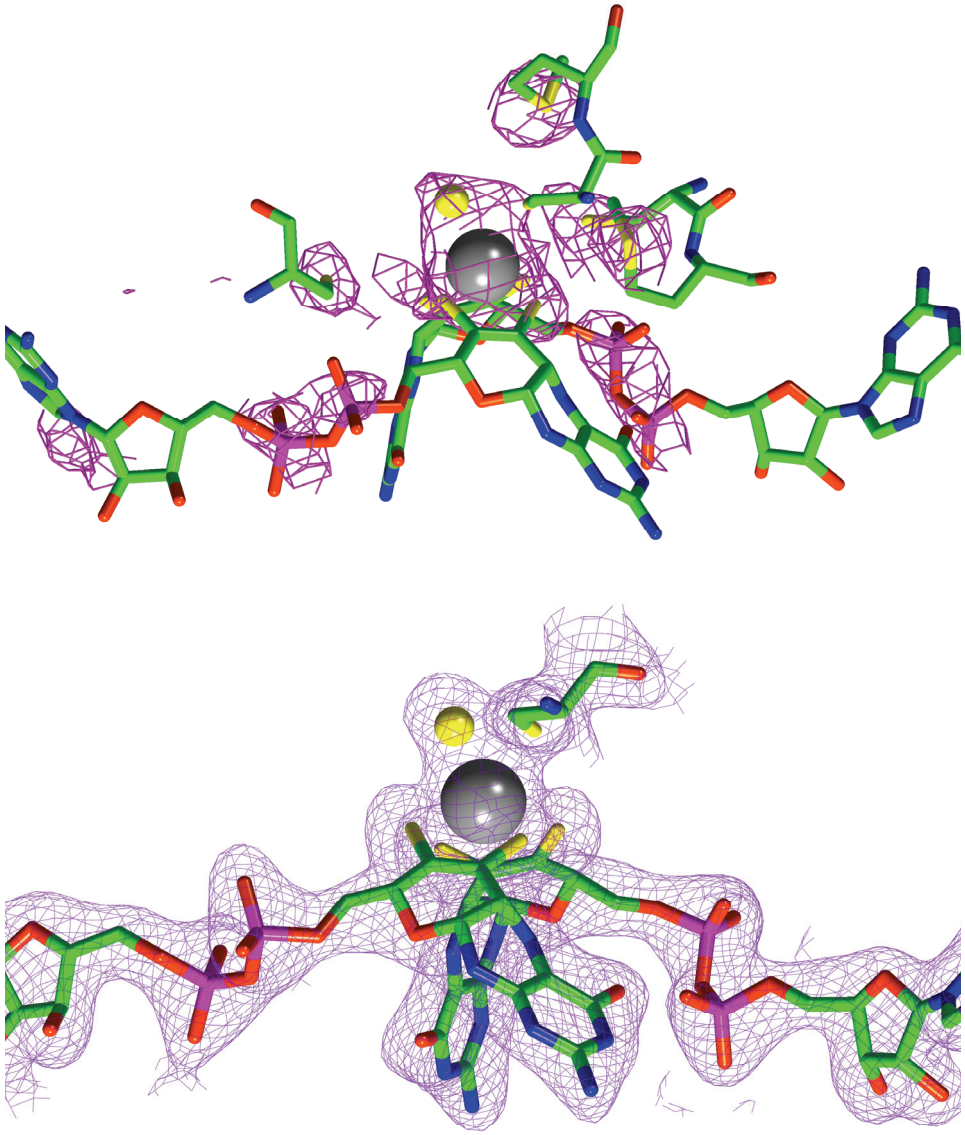

Figure III.14: Three-dimensional representation of the Mo-site of *Dd* NapA superimposed with the sulfur K-edge SAD signals peaks (upper panel) and the final total electron density map (lower panel).

As in the previous cases, no differences between this and the already published structures were detected in terms of the global fold of the amino acid chain since RMSD is 0.17 Å for 720 C_α atoms and 0.18 Å for 2880 backbone atoms. Through this experiment, it was possible to detect the positions of the 4 phosphorous atoms from the pterin cofactors (Figure III.14, upper panel), and the sulfur atoms from both the polypetidic chain and both cofactors (*i.e.* Mo-*bis*MGD and 4Fe-4S). As seen in Figure III.14 (upper panel), the presence of anomalous signals at the six coordination positions suggests that all ligands are sulfur atoms, including the formerly proposed as a water/hydroxo group.

However, due to the L_{III}-edge of the Mo is in the same energy range of the K-edge of the S, it overlaps with the anomalous signal of the sulfur which, with the present resolution, forbids fully resolving the signal of the sulfur atoms coordinated to the Mo ion.

III.2.1 UV-Vis spectroscopy in *Cn* NapAB

The electronic spectrum of *Cupriavidus necator* NapAB is dominated by the hemic components of the cofactors present in the small subunit. As shown in Figure III.15, the as-prepared sample show a Soret peak at 410 nm with a hypothetical extinction coefficient of 200 mM^{-1} cm^{-1} which was used to estimate the protein concentration. The wavelength of the Soret band, the band shape of the α and β region (500-600 nm), and the absence of charge transfer bands in the 630-650 nm region; indicate that both hemes of the air-oxidized sample are in a low-spin configuration. This is in agreement with the *bis*-histidinyl coordination found in the reported structures of *Rhodobacter sphaeroides* NapAB and *Haemophilus influenza* NapB, and in the preliminary structure of *Cn* NapAB.

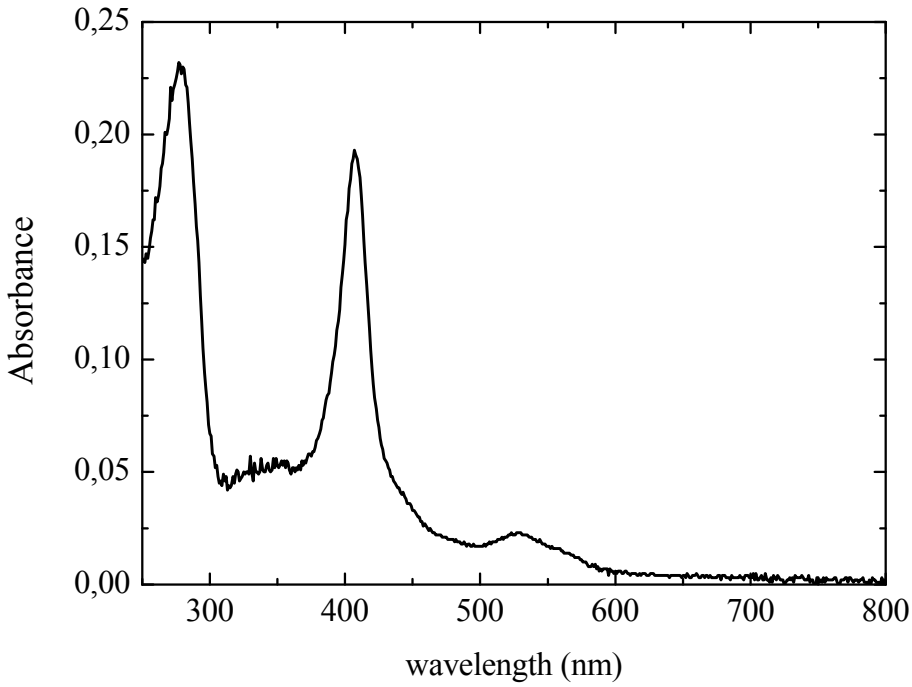

Figure III.15: UV-Vis absorption spectrum of *Cn* NapAB.

Neither a dithionite nor an ascorbate reduced spectra could be recorded owing to the low enzyme yield.

III.2.2 X-ray crystallography studies in *Cn* NapAB

Crystals were obtained using the sitting-drop with the vapor diffusion method in the several conditions listed in II.14. Many red crystals grown within a week with high yields taking into account the number of conditions tested. Best crystals, as judged from the aspect and resolution power, were obtained under the conditions 3 (Figure III.16a), 4 (Figure III.16b) and 7 (Figure III.16c) described in II.14.

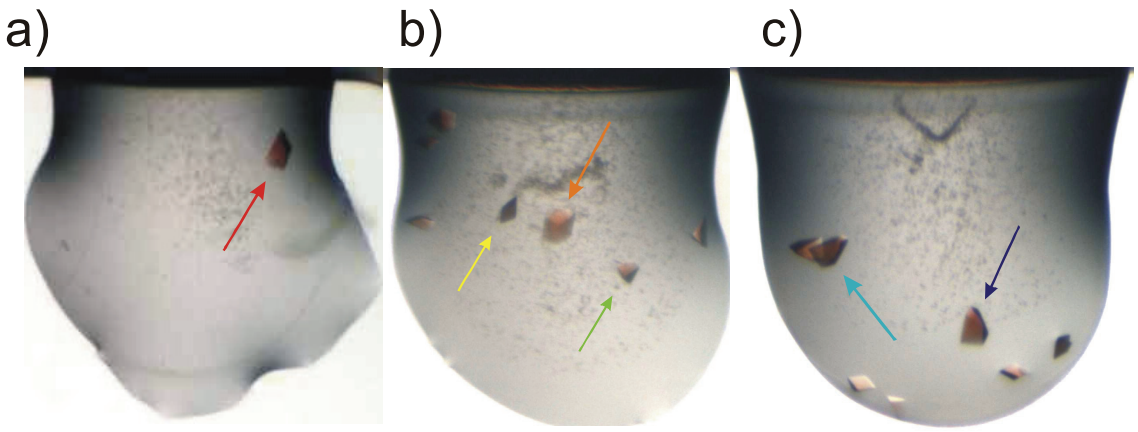

Figure III.16: single-crystals obtained from as-prepared samples of *Cn* NapAB. Arrows indicate crystals that were measured. Crystallization conditions: a) 0.1M succinate pH 7.0, 25% PEG 3350, b) 0.1M bis-Tris pH 5.5, 25% PEG 3350, and c) 0.1M bis-Tris pH 6.5, 25% PEG 3350.

Crystals indicated with arrows were collected. Data collection was carried out at 100 K using paratone oil as the cryo-protecting solution using synchrotron radiation at the ESRF (Grenoble, France). The single-crystal indicated with an orange arrow in Figure III.16b, diffracted beyond 1.6 Å resolution. At present, this dataset is being analyzed and the structure is under refinement. A preliminary representation of the global structure of *Cn* NapAB obtained from this data is shown in Figure III.17.

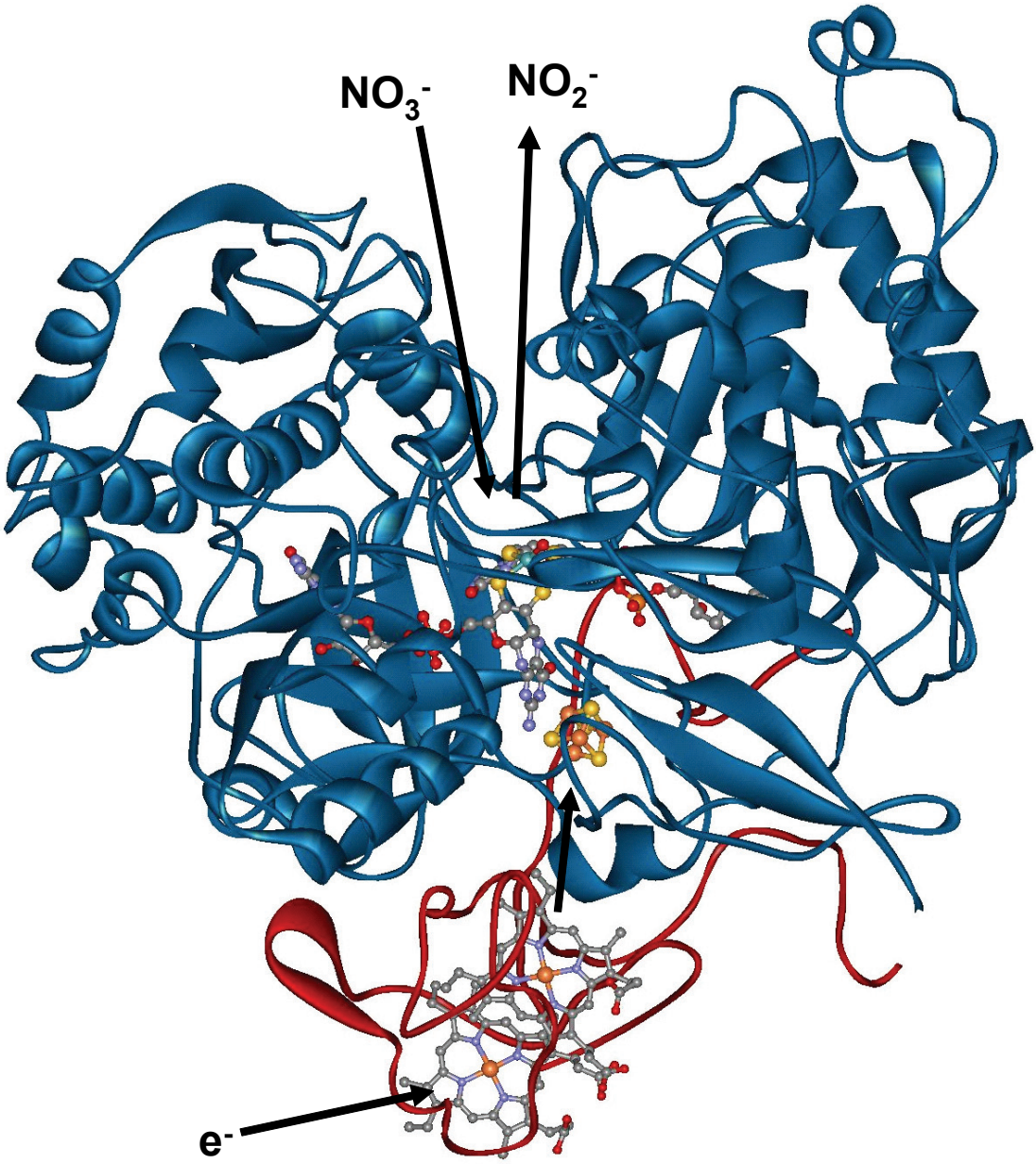

Figure III.17: Overall three-dimensional structure of NapAB from *Cupriavidus necator* H16. The large and small subunits are represented as blue and red ribbons, respectively.

.

DISCUSSION

IV.1 *Dd* NapA presents substrate promiscuity like the membrane bound nitrate reductases.

The two-electron reduction of nitrate to nitrite is a reaction energetically favorable as judged by the redox potential of the half reductive reaction (E^o = +420 mV). However, this reaction does not take place simply by the addition of a solution of a strong reducing agent like sodium dithionite (E^o = -660 mV) or reduced-methyl viologen (E^o = -440 mV). This reaction is driven both in eukaryotes and prokaryotes by the enzyme nitrate reductase (EC 1.7.99.4). Even though all nitrate reductases catalyze a unique reaction, there is a significant diversity in terms of subunits composition, properties of the active site, localization in the cell and cofactors content (Figure I.1 and I.6) [17]. These characteristics are reflected for example in their catalytic properties. Naps are characterized by their high specificity toward nitrate with michaelian constants below 100 μM and are unable to reduce other substrates analogues to nitrate. In contrast, Nars catalyze not only the reduction of nitrate but also that of chlorate, bromate, iodate, selenate, and tellurate, indicating high substrate promiscuity with respect to Naps. From these observations it can be naively concluded that the substrate promiscuity presented by Nars, which is not observed in Naps, should be produced by the different coordination type at the active site (see Figure I.1 and I.6). It was suggested that the carboxyl ligand from aspartate is loosely bound to Mo in comparison with Sγ from cysteine [61]. However, Nap from *D. desulfuricans* also display substrate promiscuity since it can reduce chlorate and bromate. This result indicates that the substrate promiscuity is not derived directly from the first coordination sphere at the active site. As previously stated, primary sequence alignments of the *Ec* NarG, *Dd* NapA, *Cn* NapA and *Rs* NapA reveal that Naps are more closely related proteins. Furthermore, a comparison of the primary sequence between Naps indicates a 35% of identity of the monomeric Nap against heterodimeric Naps, whereas the identity between heterodimeric Naps is much higher (~75%) [124].

Primary sequence alignments reveal many residues highly conserved in dimeric Naps that are different in Nap from *Desulfovibrio desulfuricans* ATCC 27774. These amino acids are highlighted in green in the sequence of *Dd* NapA (Figure IV.1).

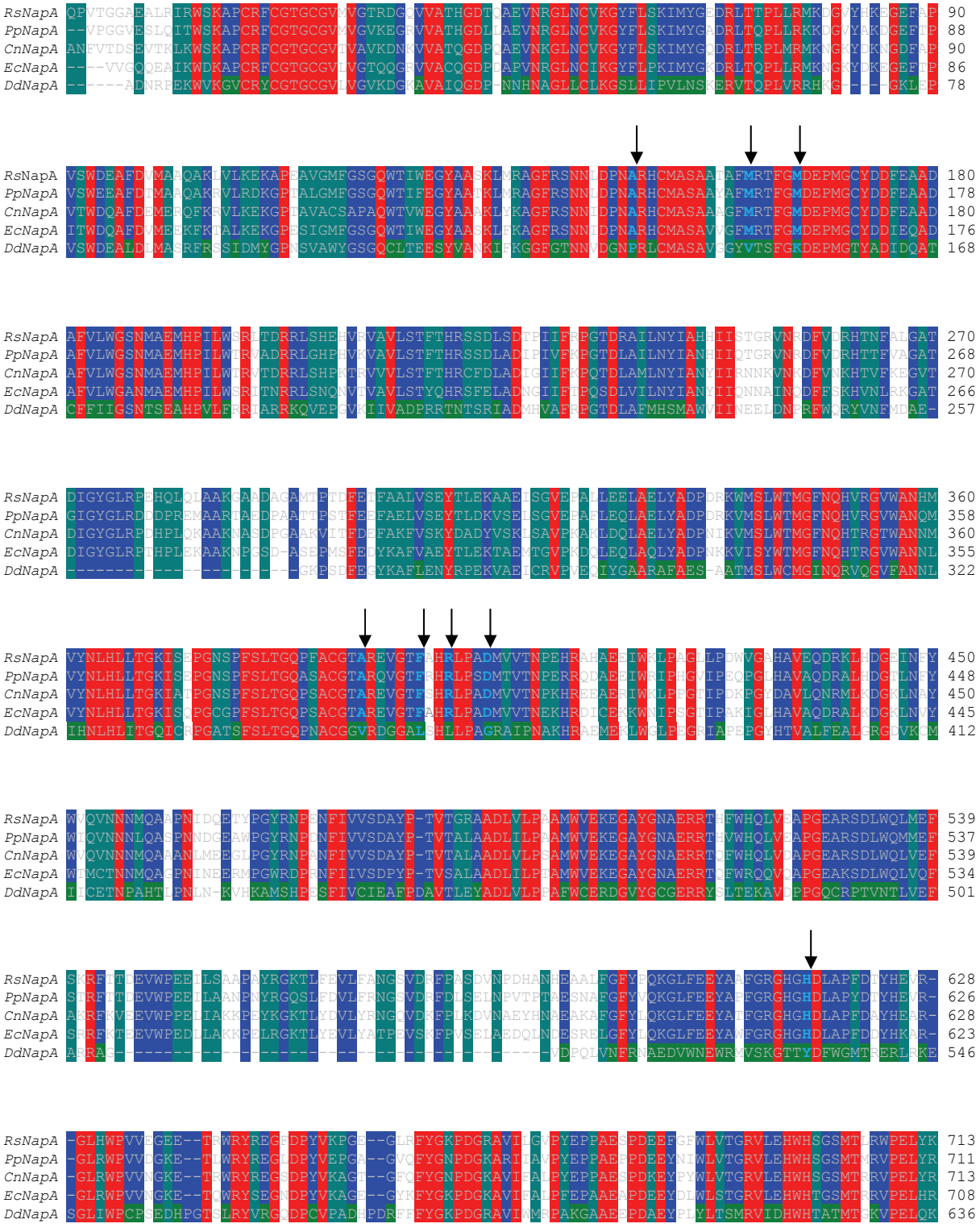

Figure IV.1: primary sequence alignment of periplasmic nitrate reductases from *Rhodobacter sphaeroides* (*Rs*), *Paracoccus pantotrophus* (*Pp*), *Cupriavidus necator* (*Cn*), *Escherichia coli* (*Ec*) and *Desulfovibrio desulfuricans* (*Dd*). Residues conservation: Red: 100%, Blue: 75%, Light green: 50%, Green: not conserved amino acids only in *Dd* NapA. Amino acids indicated with an arrow and colored in cyan are located at the funnel cavity and potentially involved in substrate promiscuity differences.

When all these amino acids are displayed in the 3D structure, it can be seen that many of them are far away from the funnel-like cavity and hence is unlikely they interact with the substrate. Figure IV.2 shows front and top views of all the amino acids that are highly conserved in dimeric Naps and that are different in *Dd* NapA. The amino acids that could potentially interact with the substrate along the path from the surface to the active site are inside the red lines. The eight amino acids that points to the funnel are indicated with arrows and highlighted in cyan in the primary sequence alignment of Figure IV.1 which are Ala_{149}, Met_{161}, Met_{166}, Ala_{391}, Phe_{397}, Arg_{400}, Asp_{404} and His_{616}. As illustrated in the 3D Figure IV.3, which is the superposition of the structures of *Rs* NapA and *Dd* NapA, at least two of the amino acids of *Rs* NapA, Met_{161} and Asp_{404}, have big sidechains in comparison with Val_{149} and Gly_{366} of *Dd* NapA. This suggests that these amino acids are important to influence the substrate accessibility. This sterical hindrance would become more important as the size of the substrate molecule increase. Because of the major differences between Naps and Nars, the 3D alignments of these enzymes cannot give the same information, and hence no definitive conclusions can be drawn using the same analysis. Mutagenesis studies might give some additional information on this point.

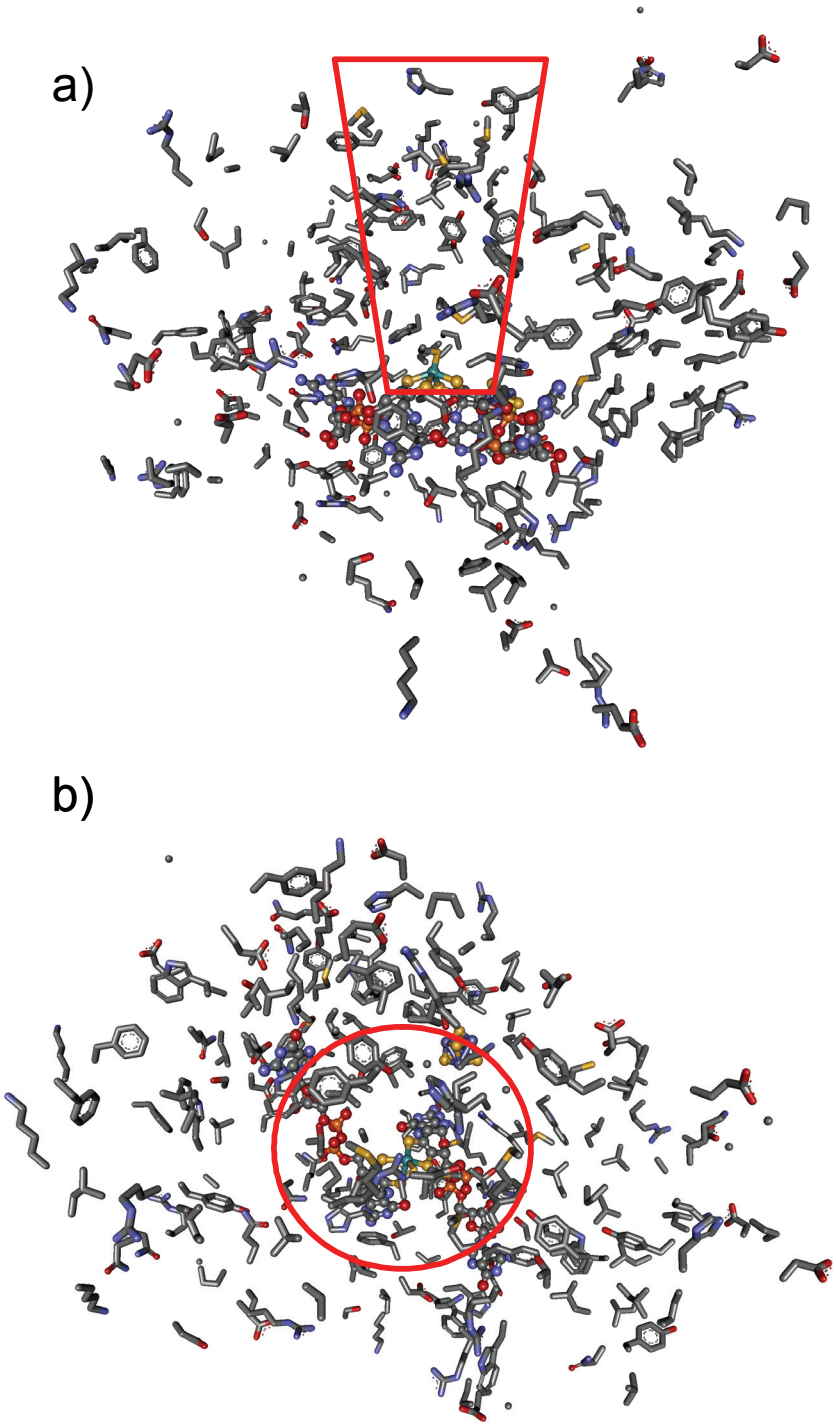

Figure IV.2: a) front and b) top views of the amino acids sidechains from the highly conserved residues of dimeric Naps that are different in *Dd* NapA. Red lines envelop the amino acids that interact directly with the funnel cavity. The 3D coordinates of the sidechains correspond to the structure of *Rs* NapAB [83].

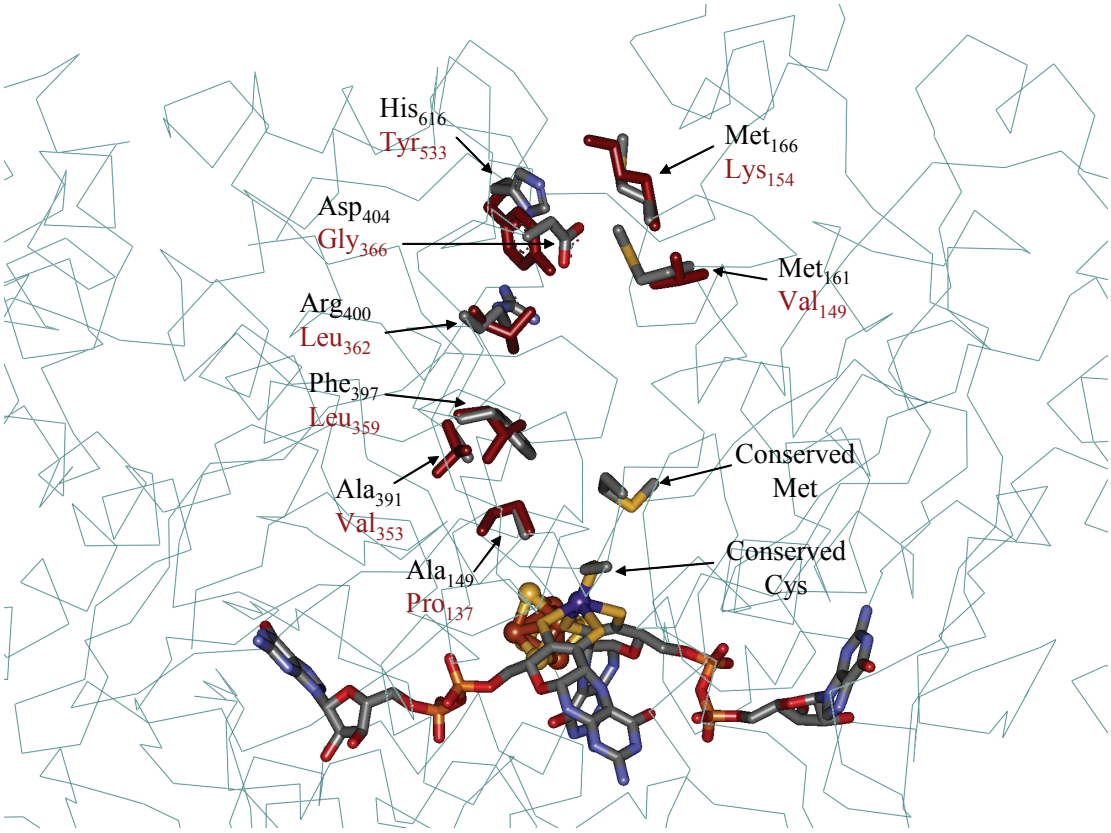

Figure IV.3: superimposition of the amino acids sidechains potentially involved in substrate specificity that are highlighted in cyan in figure IV.1. Color code: sticks in CPK depict the amino acids of *Rs* NapAB and in dark red the amino acids of *Dd* NapA. The conserved cysteine and methionine are also shown sticks in CPK color code. The backbone shown in wires corresponds to *Rs* NapA.

IV.2 The *nitrate*, *low-potential, and high-potential* Mo(V) species

As seen in Naps from *Paracoccus pantotrophus* and *Rhodobacter sphaeroides* [83, 90], *Dd* NapA shows several Mo(V) paramagnetic species: *resting* (Figure III.6, spectrum a), *low-potential* (Figure III.6, spectrum b), *nitrate* (Figure III.6, spectrum c), *high-potential* (Figure III.6, spectrum d), *cyanide* (Figure III.6, spectrum e), and *turnover* signals (Figure III.10, spectrum b and c). The *nitrate* signal is rhombic and shows a well-defined hyperfine coupling with a non solvent-exchangeable nucleus having I=1/2. The rhombic character of this signal excludes Mo(V) ion sites having coordination symmetries such as pyramidal square. On the other hand, on the basis of electron–nuclear double resonance studies of *Pp* NapAB [88] and

the crystal structure of as-purified *Dd* NapA [79], it was suggested that the non solvent-exchangeable hyperfine couplings of the *high g* [resting] and [azide] signals in *Pp* NapAB arise from the protons of the β-methylene carbon of the cysteine coordinated to the oxidized Mo site. Since *Dd* NapA and *Pp* NapAB respectively show *nitrate* and *high g* EPR signals with hyperfine couplings of similar type and magnitude (Table III.1), Cys_{140} should be coordinated to this Mo(V) redox state in *Dd* NapA. Therefore, the current interpretation for the *nitrate* species is a distorted six-coordinated site, in which the Mo(V) ion coordinates the four sulfurs of the two pterin cofactors, Sγ-Cys_{140} and one sixth ligand, presumably an oxo group (Figure I.V, scheme b). This is in contradiction with the structural data taken for the oxidized forms of *Dd* NapA [79] and other closely related enzymes [61], and the structure solved through X-ray crystallography of this sample; which showed a hydroxyl/water ligand in the position of the oxo group (Figure I.V, scheme a). However, the present resolution (2.4 Å) avoids determining the exact Mo-O distance and additional work is necessary to solve this inconsistency.

The *low-potential* and *high-potential* signals are also rhombic but the hyperfine structures are not resolved and have a larger anisotropy than the *nitrate* signal. Given the similarity between these EPR signals and those observed in *Dd* Fdh (Table III.1) [137], it is reasonable to assume that the metal environment of the EPR-detectable Mo(V) species are similar in both enzymes. EXAFS studies of oxidized and dithionite-reduced *Dd* Fdh show a distorted six-coordinated Mo site in both redox states [139], suggesting that Cys_{140} is coordinated to Mo ion in both the *low-potential* and the *high-potential* species. In such a case, the lack of hyperfine structure may be due to larger linewidths and/or noncollinearity of the hyperfine *A*-tensor of the cysteine protons with respect to the Mo(V) *g*-tensor.

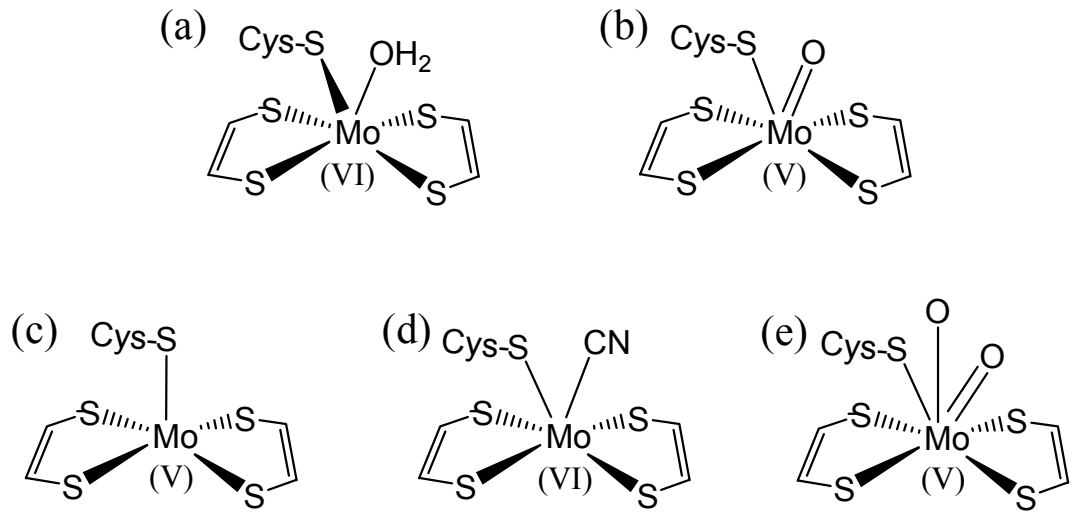

Figure IV.4: Structure of the Mo site of a) as-prepared, b) *nitrate* species, c) *cyanide* species, d) cyanide structure determined through X-ray crystallography, and e) *very high g* [cyanide].

The redox properties of the *low-potential* and *nitrate* species are very different. Although we could not precisely determine the redox potentials for the *low-potential* species, the data suggest that the redox potentials of the Mo(VI)/Mo(V) and Mo(V)/Mo(VI) couples are lower than -500 mV. In contrast, the *nitrate* Mo(V) species is stable in the range from +200 to -500 mV; therefore, it is evident that nitrate addition to the dithionite-reduced *Dd* NapA modifies the redox properties of the Mo center, resulting in the stable Mo(V) ion *nitrate* species.

IV.3 Inhibition of *Dd* NapA by cyanide and perchlorate

Cyanide-treated samples of *Dd* NapA show an EPR signal having nearly axial symmetry (Figure III.6, spectrum e), which suggests a different geometry of coordination for Mo with respect to the previously discussed Mo(V) species. This signal shows a hyperfine splitting with a non-solvent exchangeable proton, which suggests that the cysteine is coordinated to the Mo(V) ion as in the *nitrate* species. Furthermore, EPR experiments using cyanide with a different isotope composition suggest that cyanide is not coordinated to the Mo(V) ion. Mo(V) EPR signals having nearly axial symmetry have been observed in several

Mo enzymes with well-documented crystal structures, such as the members of the XO family [1] and formate-reduced *Ec* Fdh-H [140]. The crystal structures of these proteins show Mo sites in square pyramidal coordination, indicating that the Mo(V) site of the *cyanide* species in *Dd* NapA is more compatible with this coordination than a distorted hexa-coordination (Figure I.V, scheme c). Furthermore, the *cyanide* species has an EPR signal similar to those observed in the Mo-containing enzymes *Pp* NapAB [90], air-oxidized NarB from Cyanobacteria [124], and dithionite-reduced Fdh from *Methanobacterium formicicum* [138] (Table III.1), which suggests similar structures for the Mo sites of these enzymes. The two latter cases do not need cyanide to develop this almost axial signal, which together with the experiments with labeled cyanide support the fact that the cyanide is not bound to the Mo(V) ion.

A similar EPR signal called *very high g* [cyanide] was also observed in *Pp* NapAB [90, 91]. This enzyme shows also another signal developed after nitrate addition called *High g* [nitrate], which is similar to the *nitrate* signal of *Dd* NapA. On the basis of EXAFS data taken in *Pp* NapAB it was proposed hepta-coordinated sites for both species (Figure I.V, scheme e). This is in contrast with the structure of the as-prepared *Dd* NapA [79] and *Rs* NapAB [83], and for the proposed structures of *nitrate* and *cyanide* species in *Dd* NapA, which seems to be associated with a pentacoordinated Mo site. Because of the high similarity between all these enzymes, it is unlikely that they show active sites with different coordination number and type.

To correlate the EPR data with the structure of the Mo site, single-crystals were prepared from a sample containing EPR active *cyanide* species (see II.12 and III.1.7). X-ray data taken on these crystals showed a six-coordinated Mo atom similar to that of the as-prepared structure (Figure I.V, scheme d), which adds even one more conflictive point to this analysis. That cyanide is not bound to Mo(V) ions is clearly demonstrated by the experiment with cyanide labeled with different isotope composition. However, as revealed through spin quantification, *cyanide* species represent only 2.5% of the total Mo in the conditions in which

the sample was crystallized, and hence the *cyanide* species cannot be detected in a typical X-ray experiment. Consequently, the structure determined corresponds mostly to Mo in the +6 redox state. These data seem to indicate that perhaps cyanide is coordinated to Mo. In such a case, the conversion of Mo(VI)-cyanide complex to the redox state Mo(V) would imply the lost of the coordinated cyanide. With the present information no firm conclusions can be obtained and additional work such as resolution improvement of the X-ray data and EPR-mediated redox titration of the *cyanide* species could help to clarify this point.

In contrast to that observed for the experiment with cyanide, perchlorate-added samples shows no detectable Mo(V) EPR signal. As for the *cyanide* and *nitrate* species, the sample incubated with perchlorate in the EPR tube was crystallized and the structure solved at 2.0 Å resolution. The structure obtained in this condition is essentially identical to that of the as-prepared sample [79], but presents two prominent positive F_O-F_C peaks located at the funnel-like cavity, which were modeled as two perchlorate anions (Figure III.13). As discussed before in III.1.2, nitrate reductase from *Desulfovibrio desulfuricans* is unable to reduce perchlorate but can reduce smaller planar molecules such as nitrate, chlorate and bromate anions. This could be attributed not only to the larger size of the perchlorate anion but also to its 3D tetrahedral shape. In such a case, the inhibition with perchlorate should be of competitive nature as the inhibition would be produced by blocking the substrate entrance. This should be confirmed through steady-state kinetic studies.

IV.4 The redox potential modulation of the metal centers in *Dd* NapA

The different types of experiments designed to evaluate the redox behavior of *Dd* NapA show that both substrate and electron donor modulate the redox potential of the Mo site but not that of the [4Fe-4S] center (see section III.1.4 and III.1.5 and Figure III.9). Preliminary studies in this enzyme had suggested that *nitrate* species are associated with a catalytic intermediate of the reaction [94]. However, despite the addition of nitrate to

dithionite-reduced *Dd* NapA changes the *low potential* species to the *nitrate* species, the latter cannot be linked with the catalytic mechanism of the enzyme. Two results support this hypothesis: (1) *Dd* NapA shows no activity when using dithionite as the sole electron donor, and (2) the *nitrate* species is redox inactive in the potential range tested (Figure III.9).

The fact that nitrate modulates the redox potential of the molybdenum is also supported by the experiment with the enzyme in turnover conditions. Titration of the enzyme with Zn-reduced MV (E^0=-440 mV *vs*. NHE) does not reduce either the [4Fe–4S] center or the Mo(VI) ion, as no paramagnetic species were detected in the +100 to -400 mV range. However, nitrate addition to this MV-reacted sample yields the *turnover* species, which is redox active. The *turnover* signal accounts to 0.5-0.6 spins/protein molecule as revealed by the comparison with a Cu-EDTA standard. However, metal quantification of several as-prepared and reacted samples of *Dd* NapA yields 0.5-0.8 Mo ions *per* protein molecule, suggesting that near 100% of the total Mo is present as Mo(V). Therefore, this indicates that the redox chemistry of the enzyme is changed in the presence of the substrate and the electron donor and that a large fraction of the Mo ions are in the +5 redox state when the reduced MV is fully consumed. This point will be analyzed in IV.5.

Substrate-dependent redox potential of the active site have been observed in NarB from *Synechococcus* sp. [124]. EPR-mediated potentiometry of this enzyme showed that Mo(VI) can be easily reduced to Mo(V) (E^o= -150 mV), but Mo cannot be reduced to the +4 redox state even dropping the electrochemical potential until -550 mV. Furthermore, when the enzyme is studied through direct electrochemistry in the presence of limiting amounts of nitrate, catalytic currents centered at -350 mV are developed. These authors concluded that it correspond to the potential at which the catalytic reaction is carried out, indicating that the redox potentials of the Mo couple relevant to catalysis is switched to this value in the presence of the substrate [124].

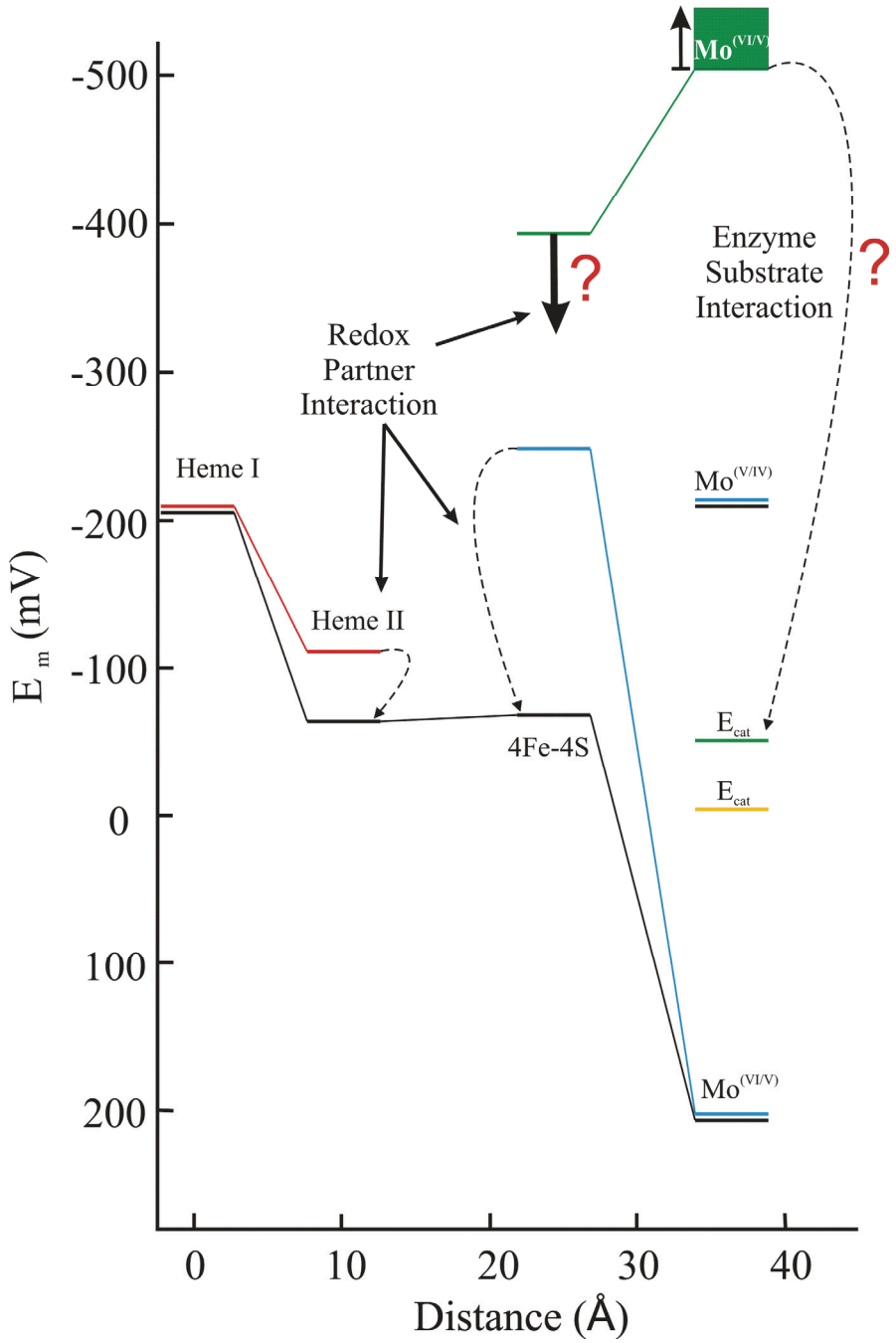

Figure IV.5: representation of the redox modulation observed in *Rs* NapAB cofactors and theorized in *Dd* NapA. Plot adapted from [83] shows the midpoint redox potentials of the metal cofactors in both the free (red and blue are NapB and NapA, respectively) and complexed forms (black). In yellow is the E_{cat} value reported in [141]. In green are represented the potentials of the *Dd* NapA cofactors. Arrows depict the redox potential modulation produced for enzyme- partner and enzyme-substrate interactions.

Similar results were obtained by preliminary protein film voltametry (PFV) studies in *Dd* NapA that show that despite Mo cannot be reduced to the +4 redox state even at -500 mV, the

catalytic currents (E_{cat}) are centered at -60 mV (Moura JJG, personal communication) and in *Rs* NapAB, despite the wide gap between the Mo couples determined by EPR-mediated potentiometry [83] (see Figure IV.5), PFV studies showed E_{cat} centered at -5 mV [141]. All these results indicate that the redox properties of the Mo active site are different in turnover conditions.

Studies performed in *Rs* NapAB showed that the modulation occurs not only at the active site but also with the electron transfer cofactors. The redox potential of the FeS cluster is -250 mV in the *Rs* NapA monomer, but the Eº value rises up to -70 mV when the heterodimer NapAB is regenerated by adding stoichiometric amounts of NapB. The same phenomenon occurs with the heme II at the NapB subunit, which is stabilized by 40 mV with respect to the monomer form [83]. All these results suggest that metallic cofactors in *Rs* NapAB are energetically ordered to favor electron transfer from the redox partner to the substrate. The very negative Eº value determined for the FeS cluster in *Dd* NapA (-390 mV) and the fact that the FeS center cannot be reduced after methyl viologen addition suggest that this is not the case in the *Dd* enzyme, which in turn suggests that a sort of redox modulation should occur. In any case, electron transfer in proteins is in some cases performed against of the energetic barriers as seen for example in *Ec* Nar [60]. The determination of the redox properties of the *Dd* NapA in the presence of the physiological redox partner should be necessary to clarify this point.

As already established, the menaquinone comprises the quinone pool present in the cytoplasmic membrane of *Desulfovibrio* species. The menaquinone/menaquinol couple has a midpoint redox potential of -80 mV. On the basis of the results obtained in the potentiometric titration and the characteristics of the *turnover* signal, clearly, *Dd* NapA would not be able to reduce the Mo to the +4 redox state before nitrate binding due to the lack of driving force. Then, the enzyme cannot operate via the catalytic mechanism proposed by Dias *et al*. (Figure IV.6) [79]. However, under physiological conditions in the absence of unspecific oxidizing

agents like oxygen, Mo remains in the +5 oxidation state which is represented by the *turnover* signal, instead of the fully oxidized +6 state. This +5 state could symbolize the reductively activated form of a nitrate reductase as discussed in the examples of *Pp* NarGH and NarB from *Synechococcus* sp. [142].

IV.5 The *turnover* signal and the mechanism of nitrate reduction.

Figure IV.6 shows the accepted catalytic mechanism of *Dd* NapA, which was postulated on the basis of the X-ray data of the periplasmic nitrate reductase from *D. desulfuricans* [79].

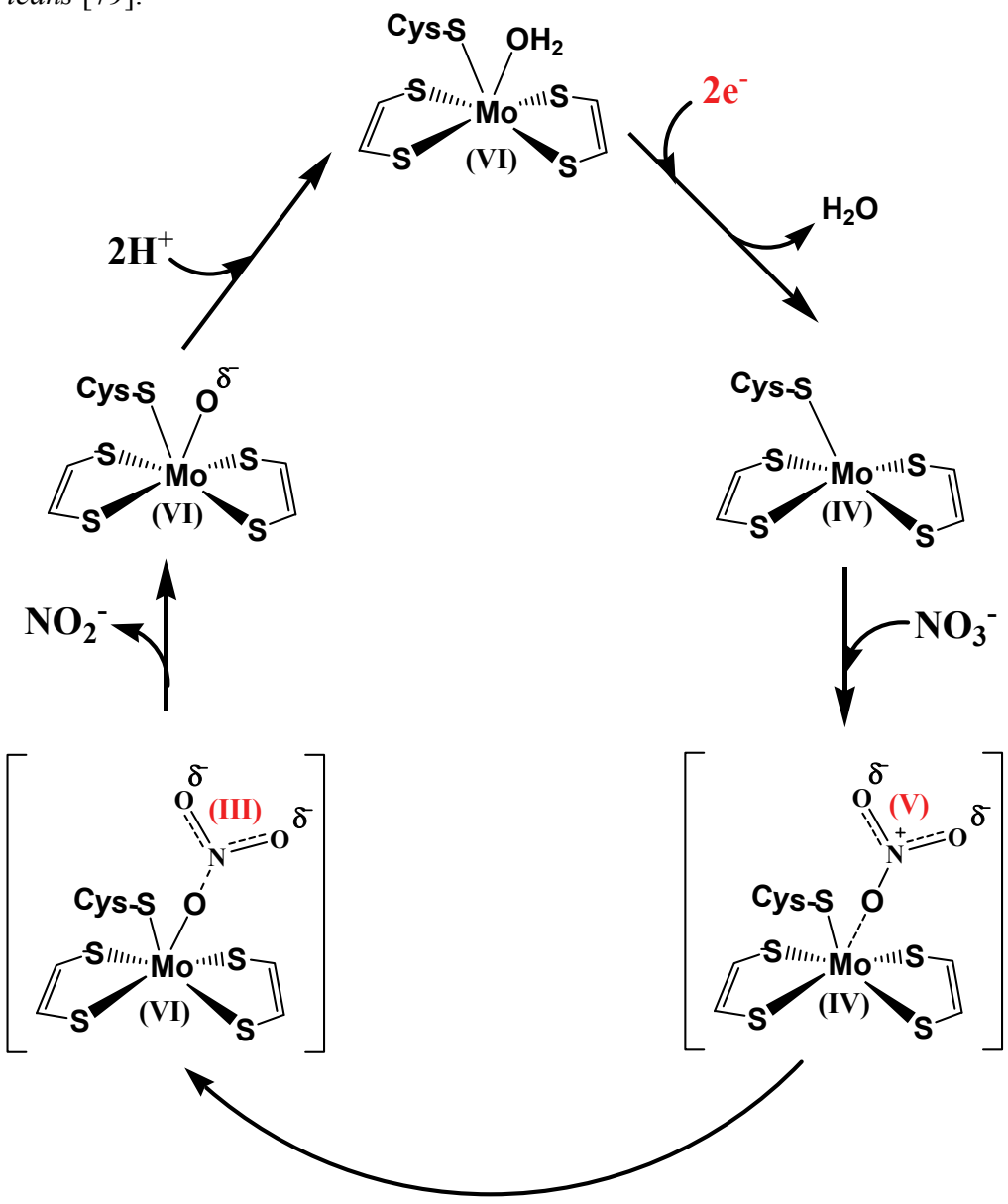

Figure IV.6: mechanism of nitrate reduction proposed on the basis of the 3D crystallographic structure [79].

This mechanism implies that the catalytic reduction of nitrate is carried out through a two-electron process. The first step is the reduction of the oxidized Mo site to the reduced Mo(IV) form. In this process, the coordinated water molecule is released upon reduction of the active site, resulting in a distorted pentacoordinated Mo(IV) site. The proposal of this species was based on X-ray data taken in the reduced form of the closely related Fdh-H from *E. coli* [143]. The reaction of the nitrate with the Mo site occurs in the vacant position left by the water molecule. The two electrons located at the Mo site are transferred to the nitrogen of the nitrate molecule, with the nitrogen atom being reduced from the +V to the +III redox state and with the concomitant oxidation of the Mo ion from the +IV to the +VI redox state. This process should produce the weakening of the O-N bond and nitrite release; leaving an oxo group at the sixth coordination position. This oxo group is very proteophilic [144], and is straight protonated by two protons from the solvent regenerating the original active site and thus completing the mass balance of the half reductive reaction.

As discussed before, studies in *Rs* NapAB and NarB from *Synechococcus* sp. show that enzymatic nitrate reduction can also occur when the substrate binds the Mo ion in the +5 redox state [83, 124]. In line with these results, the *turnover* signal is yielded when a *Dd* NapA sample incubated with reduced methyl viologen is reacted with the substrate. The fact that the same signal was obtained when reacted with $^{14}NO_3^-$, $^{15}NO_3^-$ and ClO_3^-, indicates that it is not associated with an enzyme-substrate intermediate and the experiment performed in a D_2O-exchanged sample suggests that a water molecule is coordinated to the Mo(V) ion. The axial symmetry of the *turnover* signal (Figure III.10) suggest, as for the *cyanide* species, a Mo site in a square-pyramidal geometry with a S_4-Mo-OH_2 coordination. In such a case, one possibility is that the sidechain of the Cys_{140} is not coordinated to the Mo ion, which could explain the lack of hyperfine coupling with non-solvent exchangeable protons. This is in line with the recent re-evaluation of the reduced form of *Ec* Fdh-H, which shows that the Se-Cys

moves away with the apical position being occupied by a ligand presumably to be a sulfur atom [145]. However, the correlation between the EPR properties and the structure of the Mo sites are not well understood yet and therefore, a Mo-S bond with the Cysteine is included in the proposal of Figure IV.7.

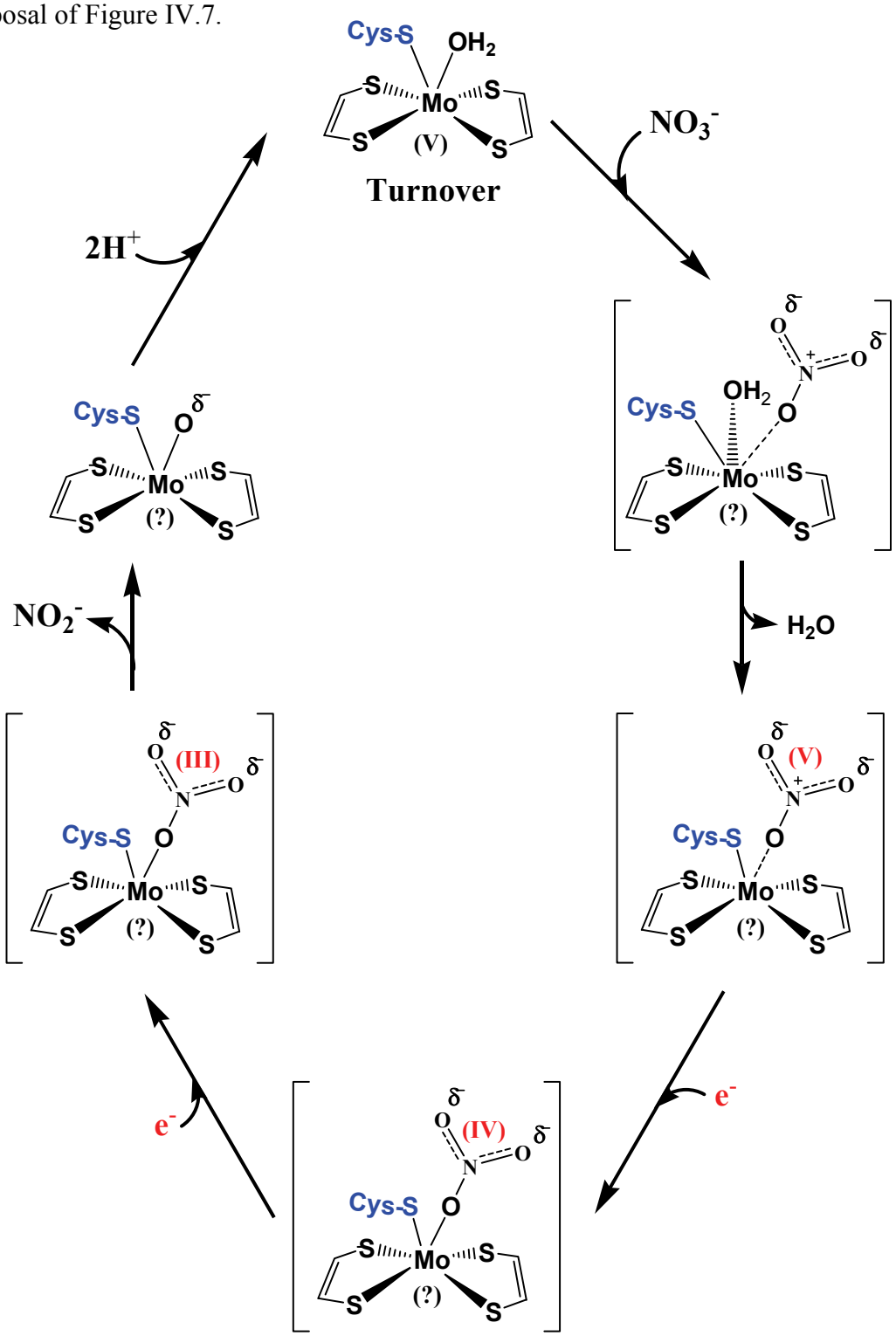

Figure IV.7: new proposal of the mechanism of nitrate reduction on the basis of the EPR results. In red are depicted the oxidation state of the nitrogen atom of nitrate in the two steps of one-electron reduction.

Figure IV.7 displays a tentative proposal of the reaction mechanism of the nitrate reaction which takes into account the new evidences revealed by the *turnover* signal. As said before, spin quantification of this signal reveal that near 100% of the total molybdenum is in the +5 redox state. This indicates that after all the electron donor is oxidized, the enzyme begin a new cycle with the active site in the Mo(V) redox state, which constitutes the main difference with the mechanism of Figure IV.6. Addition of the substrate together with the presence of the reduced electron donor should induce the releasing of the water molecule leaving a vacant position for substrate binding and starting the catalytic cycle.

This redox cycle of the enzyme must necessarely occurs between -400 mV (the lowest potential reached upon addition of and excess of MV) and -150 mV (potential at which after all the reduced MV is consumed). With the present results it can be concluded that Mo ion cannot be present as Mo(VI) during the redox cycle of the enzyme because this redox state is only obtained after air oxidation. The current interpretation is that the adduct Mo-**O**-NO_2^- is sequentially reduced in two steps of one electron each, transferring the electrons to the N atom. Then, the process should end as proposed before, releasing NO_2^- and consuming two protons from the solvent to mass balancing of the half reductive reaction. However, non definitive conclusions can be obtained about the redox state of the Mo ion at the different stages of the cycle proposed in Figure IV.7. Considering that the type of reactions involve electron transfer processes, it could be speculated that perhaps some of the intermediates postulated in Figure IV.7 could correspond to Mo(IV) species, but time-resolved experiments should be necessary to confirm this hypothesis.

IV.6 New structural evidences raise questions about the nature of the OH/OH_2 ligand of *Dd* NapA.

As stated in the results section (III.1.7 and Figure III.14), the presence of anomalous signals at the sixth coordination positions suggests that all ligands around the Mo are sulfur

atoms. This indicates that the ligand proposed to be a water/hydroxo group might be a sulfido ligand. However, as the present resolution and that the L_{III}-edge of the Mo is in the same energy range of the K-edge of the S, the overlap of both anomalous signals forbids formulating a definitive conclusion. Nevertheless, the presence of a sulfur atom at the sixth coordination position would imply major changes in the mechanism proposed in Figure IV.7. Similar conclusions are suggested from the X-ray data taken in the W-Fdh from *D. gigas* [146] and from the re-evaluation of the X-ray data of the *Ec* Fdh-H [145], in which case the mechanism proposed in Figure IV.7 should be reevaluated.

CONCLUDING REMARKS

The present thesis work deals with the biochemical, structural, and spectroscopic characterization of the periplasmic nitrate reductase purified from the sulfate reducing bacterium *D. desulfuricans* ATCC 27774. Furthermore, the purification of the periplasmic nitrate reductase from the chemolitotrophic bacterium *Cupriavidus necator* was optimized and a preliminary X-ray data characterization is reported.

Cells of the SRB *D. desulfuricans* were grown in denitrifying conditions and the purification of the NapA monomer was optimized using a protocol based on ionic exchange chromatography.

EPR data taken in different experimental conditions allowed the characterization of different Mo(V) species. The detected paramagnetic species show different both EPR properties and redox behaviors. These data indicate that the Mo ions show a high flexibility of coordination and that the redox properties of the Mo ions can be tunable to perform the catalysis.

The experiments performed in inhibiting conditions suggest that enzyme inhibition occurs at different levels. For the case of cyanide, EPR data suggest that cyanide is not bound the Mo ion and, in addition, the cyanide molecule induces structural changes at the Mo site giving a pentacoordinated Mo ion. This result is apparently in contradiction with those obtained from the X-ray data, which show a hexacoordinated Mo site. One possible explanation for this contradiction is that Mo(V) and Mo(VI) ions have different coordination geometries as has been observed in the closely related *Dd* Fdh [143, 145]. In contrast, for the case of perchlorate, the X-ray structure solved from samples incubated with perchlorate suggests that this anion inhibits *Dd* NapA by blocking the funnel-like cavity. X-ray data taken at higher resolution together with additional EPR experiments are necessary to solve all these discrepancies. More important even, the conditions of the kinetic assay should be standarized. This is essential to confirm the different inhibition mechanisms proposed on the basis of the X-ray and EPR results.

Another important result, which could have implications from a physiological point of view, is that *Dd* NapA is able to reduce anions other than nitrate. This characteristic, which is well-documented for membrane bound nitrate reductases, has not been observed for the periplasmic enzymes. Although the molecular basis of the substrate promiscuity in NRs is not understood at present, this study allows concluding that the different coordinations around Mo ion in these two groups of nitrate reductases is not the cause for this peculiarity.

A key point of the present thesis work lies in the finding of the *turnover* signal. EPR-mediated potentiometric titrations with both dithionite and Zn-reduced MV indicate that catalysis by *Dd* NapA is carried out via a redox modulation of the Mo-site when the substrate interacts with it. Furthermore, the facts that: a) the same *turnover* species is yielded using either nitrate or chlorate, b) the spin quantification is near to 100%, and c) two solvent-exchangeable protons are detected, let concluding that the *turnover* signal is not given by a substrate–Mo(V) complex and that this might correspond to a *resting* state of the enzyme before starting a new cycle in the mechanism. Furthermore, although with no firm confirmation yet, several evidences suggest that the ligand identified as OH/OH_2 in several members of the DMSO reductase family could be a sulfur atom, in which case all the mechanisms proposed for these enzymes should be reevaluated.

After several years of investigation on nitrates reductases, several points remain enigmatic. It is evident that important progresses have been achieved with the X-ray and spectroscopic characterization of these enzymes. However, as discussed in this work, the exact nature of the molecular processes that occur during catalysis are not elucidated yet. This constitutes one of the most important challenges and the characterization of a large number of these proteins, *e.g.* the determination of the 3D crystallographic structure of *Cn* NapAB, and additional studies on the best characterized examples will undoubtedly contribute to a better understanding of these enzymes.

BIBLIOGRAPHY

1. Hille R. *The Mononuclear Molybdenum Enzymes.* Chem Rev, **1996**. 96(7): 2757-2816.

2. Hille R. *Molybdenum and tungsten in biology.* Trends Biochem Sci, **2002**. 27(7): 360-7.

3. Dos Santos P, Igarashi R, Lee H, Hoffmann B, Seefeldt L, and Dean D. *Substrate interactions with the nitrogenase active site.* Acc Chem Res, **2005**. 38(3): 208-214.

4. Dobbek H, Gremer L, Kiefersauer R, Huber R, and Meyer O. *Catalysis at a dinuclear [CuSMo(=O)OH] cluster in a CO dehydrogenase resolved at 1.1-A resolution.* Proc Natl Acad Sci, **2002**. 99: 15971-15976.

5. Brondino CD, Rivas MG, Romao MJ, Moura JJG, and Moura I. *Structural and electron paramagnetic resonance (EPR) studies of mononnuclear molybdenum enzymes from sulfate-reducing bacteria.* Acc Chem Res, **2006**. 39(10): 788-796.

6. Richardson DJ and Watmough NJ. *Inorganic nitrogen metabolism in bacteria.* Curr Opin Chem Biol, **1999**. 3(2): 207-19.

7. Berks BC, Ferguson SJ, Moir JW, and Richardson DJ. *Enzymes and associated electron transport systems that catalyse the respiratory reduction of nitrogen oxides and oxyanions.* Biochim Biophys Acta, **1995**. 1232(3): 97-173.

8. Zumft WG. *Cell biology and molecular basis of denitrification.* Microbiol Mol Biol Rev, **1997**. 61(4): 533-616.

9. Moreno-Vivian C and Ferguson SJ. *Definition and distinction between assimilatory, dissimilatory and respiratory pathways.* Mol Microbiol, **1998**. 29(2): 664-6.

10. Moreno-Vivian C, Cabello P, Martinez-Luque M, Blasco R, and Castillo F. *Prokaryotic Nitrate Reduction: Molecular Properties and Functional Distinction among Bacterial Nitrate Reductases.* J Bacteriol, **1999**. 181(21): 6573-6584.

11. Richardson D and Sawers G. *Structural Biology: PMF Through the Redox Loop.* Science, **2002**. 295(5561): 1842-1843.

12. Lin JT and Stewart V. *Nitrate assimilation by bacteria.* Adv Microb Physiol, **1998**. 39: 1-30, 379.

13. Richardson DJ, Berks BC, Russell DA, Spiro S, and Taylor CJ. *Functional, biochemical and genetic diversity of prokaryotic nitrate reductases.* Cell Mol Life Sci, **2001**. 58(2): 165-78.

14. Cabello P, Roldan MD, and Moreno-Vivian C. *Nitrate reduction and the nitrogen cycle in archaea.* Microbiology, **2004**. 150(11): 3527-3546.

15. Ferguson SJ. *Nitrogen cycle enzymology.* Curr Opin Chem Biol, **1998**. 2(2): 182-93.

16. Richardson DJ. *Bacterial respiration: a flexible process for a changing environment.* Microbiology, **2000**. 146(3): 551-571.

17. Gonzalez PJ, Correia C, Moura I, Brondino CD, and Moura JJG. *Bacterial nitrate reductases: Molecular and biological aspects of nitrate reduction.* J Inorg Biochem, **2006**. 100(5-6): 1015-23.

18. van de Graaf AA, Mulder A, de Bruijn P, Jetten MS, Robertson LA, and Kuenen JG. *Anaerobic oxidation of ammonium is a biologically mediated process.* Appl Envir Microbiol, **1995**. 61(4): 1246-1251.

19. Jetten MS, Strous M, van de Pas-Schoon KT, Schalk J, van Dongen UG, van de Graaf AA, Logemann S, Muyzer G, van Loosdrecht MC, and Kuenen JG. *The anaerobic oxidation of ammonium.* FEMS Microbiol Rev, **1998**. 22(5): 421-37.

20. Friedrich C, Rother D, Bardischewsky F, Quentmeier A, and Fischer J. *Oxidation of Reduced Inorganic Sulfur Compounds by Bacteria: Emergence of a Common Mechanism?* Appl Environ Microbiol, **2001**. 67(7): 2873–2882.

21. Urich T, Gomes CM, Kletzin A, and Frazao C. *X-ray Structure of a Self-Compartmentalizing Sulfur Cycle Metalloenzyme.* Science, **2006**. 311(5763): 996-1000.

22. Schrader N, Fischer K, Theis K, Mendel RR, Schwarz G, and Kisker C. *The crystal structure of plant sulfite oxidase provides insights into sulfite oxidation in plants and animals.* Structure, **2003**. 11(10): 1251-63.

23. Mendel RR. *The role of the molybdenum cofactor in humans.* Biofactors, **2000**. 11(1-2): 147-8.

24. Kappler U and Bailey S. *Molecular Basis of Intramolecular Electron Transfer in Sulfite-oxidizing Enzymes Is Revealed by High Resolution Structure of a Heterodimeric Complex of the Catalytic Molybdopterin Subunit and a c-Type Cytochrome Subunit.* J Biol Chem, **2005**. 280(26): 24999-25007.

25. Kappler U, Bennett B, Rethmeier J, Schwarz G, Deutzmann R, McEwan AG, and Dahl C. *Sulfite:Cytochrome c Oxidoreductase from Thiobacillus novellus. Purification, characterization, and molecular biology of a heterodimeric member of the sulfite oxidase family.* J Biol Chem, **2000**. 275(18): 13202-13212.

26. Moura I, LeGall J, Line AR, Peck Jr HD, Fauque G, Xavier AV, DerVartanian DV, Moura JJG, and Huynh BH. *Characterization of Two Dissimilatory Sulfite Reductases (Desulforubidin and Desulfoviridin) from the Sulfate-Reducing Bacteria. Mossbauer and EPR Studies.* J Am Chem Soc, **1988**. 110: 1075-1082.

27. Moura JJG, González PJ, Moura I, and Fauque G. *Dissimilatory nitrate and nitrite ammonification by sulphate-reducing eubacteria*. Sulphate-Reducing Bacteria: Environmental and Engineered Systems, ed. Barton and Hamilton. **2006**: Cambridge Univ Press.

28. Heidelberg JF, Seshadri R, Haveman SA, Hemme CL, Paulsen IT, Kolonay JF, Eisen JA, Ward N, Methe B, Brinkac LM, Daugherty SC, Deboy RT, Dodson RJ, Durkin AS, Madupu R, Nelson WC, Sullivan SA, Fouts D, Haft DH, Selengut J, Peterson JD, Davidsen TM, Zafar N, Zhou L, Radune D, Dimitrov G, Hance M, Tran K, Khouri H, Gill J, Utterback TR, Feldblyum TV, Wall JD, Voordouw G, and Fraser CM. *The genome sequence of the anaerobic, sulfate-reducing bacterium Desulfovibrio vulgaris Hildenborough.* Nat Biotechnol, **2004**. 22(5): 554-9.

29. Copeland A, Lucas S, Lapidus A, Barry K, Detter JC, Glavina T, Hammon N, Israni S, Pitluck S, Goodwin LA, Schmutz J, Larimer F, Land M, Kyrpides N, Ivanova N, and Richardson P. *Complete sequence of Desulfovibrio desulfuricans G20*. **2005**, US DOE Joint Genome Institute.

30. Gavel O, Bursakov S, Calvete J, George G, Moura J, and Moura I. *ATP sulfurylases from sulfate-reducing bacteria of the genus Desulfovibrio. A novel metalloprotein containing cobalt and zinc.* Biochemistry, **1998**. 37(46): 16225-32.

31. Bramlett R and Peck HJ. *Some Physical and Kinetic Properties of Adenylyl Sulfate Reductase from Desulfovibrio vulgaris.* J Biol Chem, **1975**. 250(8): 2979-2986.

32. Wolfe BM, Lui SM, and Cowan JA. *Desulfoviridin, a multimeric-dissimilatory sulfite reductase from Desulfovibrio vulgaris (Hildenborough). Purification, characterization, kinetics and EPR studies.* Eur J Biochem, **1994**. 223(1): 79-89.

33. Fauque G, LeGall J, and Barton L. *Sulfate-reducing and sulfur-reducing Bacteria*. In Variations in Autotrophic Life, ed. JMSaLL Barton. **1991**, London: Academic Press Limited. 271-337.

34. Fauque G and Ollivier B. *Anaerobes: the sulfate-reducing bacteria as an example of metabolic diversity*. In Microbial Diversity and Bioprospecting, ed. A Bull. **2004**, Washington, DC: ASM Press. 169-176.

35. LeGall J and Fauque G. *Dissimilatory reduction of sulfur compounds*. In Biology of Anaerobic Microorganims, ed. AJB Zehnder. **1988**, New York: John Wiley and Sons, Inc. 587-639.

36. Dalsgaard T and Bak F. *Nitrate reduction in a sulfate-reducing bacterium, Desulfovibrio desulfuricans, isolated from rice paddy soil: sulfide inhibition, kinetics, and regulation.* Appl Environ Microbiol, **1994**. 60: 291-297.

37. Keith S and Herbert R. *Dissimilatory nitrate reduction by a strain of Desulfovibrio desulfuricans.* FEMS Microbiology Letters, **1983**. 18: 55-59.

38. Lopez-Cortes A, Fardeau M-L, Fauque G, Joulian C, and Ollivier B. *Reclassification of the sulfate- and nitrate-reducing bacterium Desulfovibrio vulgaris subsp. oxamicus as Desulfovibrio oxamicus sp. nov., comb. nov.* Int J Syst Evol Microbiol, **2006**. 56(7): 1495-1499.

39. McCready R, Gould W, and Cook F. *Respiratory nitrate reduction by Desulfovibrio sp.* Arch Microbiol, **1983**. 135: 182-185.

40. Mitchell G, Jones J, and Cole J. *Distribution and regulation of nitrate and nitrite reduction by Desulfovibrio and Desulfotomaculum species.* Arch Microbiol, **1986**. 144: 35-40.

41. Moura I, Bursakov S, Costa C, and Moura J. *Nitrate and nitrite utilization in sulfate-reducing bacteria.* Anaerobe, **1997**. 3: 279-290.

42. Seitz H and Cypionka H. *Chemolithotrophic growth of Desulfovibrio desulfuricans with hydrogen coupled to ammonification of nitrate or nitrite.* Arch Microbiol, **1986**. 146: 63-67.

43. Trinkerl M, Breunig A, Schauder R, and Konig H. *Desulfovibrio termitidis sp. nov., a carbohydrate-degrading sulfate-reducing bacterium from the hindgut of a termite.* Syst Appl Microbiol, **1990**. 13: 372-377.

44. Plugge C, Balk M, and Stams A. *Desulfotomaculum thermobenzoicum subsp. thermosyntrophicum subsp. nov., a thermophilic, syntrophic, propionate-oxidizing, spore-forming bacterium.* Int J Syst Evol Microbiol, **2002**. 52: 391-399.

45. Widdel F. *Microbiology and ecology of sulfate- and sulfur-reducing bacteria*. In Biology of Anaerobic Microorganims, ed. A Zehnder. **1988**, New York: John Wiley and Sons, Inc. 469-585.

46. Lie T, Clawson M, Godchaux W, and Leadbetter E. *Sulfdidogenesis from 2-aminoethanesulfonate (taurine) fermentation by a morphologically unusual sulfate-*

reducing bacterium, Desulforhopalus singaporensis sp. nov. Applied and Environ Microbiol, **1999**. 65: 3328-3334.

47. Sonne-Hansen J and Ahring B. *Thermodesulfobacterium hveragerdense sp. nov., and Thermodesulfovibrio islandicus sp. nov., two thermophilic sulfate-reducing bacteria isolated from a Icelandic hot spring.* Syst Appl Microbiol, **1999**. 22: 559-564.
48. Mori K, Kim H, T K, and Hanada S. *A novel lineage of sullate-reducing microorganisms: Thermodesulfobiaceae fam. nov., Thermodesulfobium narugense, gen. nov., sp. nov., a new thermophilic isolate from a hot spring.* Extremophiles, **2003**. 7: 283-290.
49. Parekh M, Drake H, and Daniel S. *Bidirectional transformation of aromatic aldehydes by Desulfovibrio desulfuricans under nitrate-dissimilating conditions.* Lett Appl Microbiol, **1996**. 22: 115-120.
50. Siddiqui R, Warnecke-Eberz U, Hengsberger A, Schneider B, Kostka S, and Friedrich B. *Structure and function of a periplasmic nitrate reductase in Alcaligenes eutrophus H16.* J Bacteriol, **1993**. 175(18): 5867-5876.
51. Stolz JF and Basu P. *Evolution of nitrate reductase: molecular and structural variations on a common function.* Chembiochem, **2002**. 3(2-3): 198-206.
52. Vincent SP and Bray RC. *Electron-paramagnetic-resonance studies on nitrate reductase from Escherichia coli K12.* Biochem J, **1978**. 171(3): 639-47.
53. Chaudhry GR, Chaiken IM, and MacGregor CH. *An activity from Escherichia coli membranes responsible for the modification of nitrate reductase to its precursor form.* J Biol Chem, **1983**. 258(9): 5828-5833.
54. Godfrey C, Greenwood C, Thomson AJ, Bray RC, and George GN. *Electron-paramagnetic-resonance spectroscopy studies on the dissimilatory nitrate reductase from Pseudomonas aeruginosa.* Biochem J, **1984**. 224(2): 601-8.

55. Craske A and Ferguson S. *The respiratory nitrate reductase from Paracoccus denitrificans. Molecular characterisation and kinetic properties.* Eur J Biochem, **1986**. 158(2): 429-436.

56. Ballard A and Ferguson S. *Respiratory nitrate reductase from Paracoccus denitrificans. Evidence for two b-type haems in the gamma subunit and properties of a water- soluble active enzyme containing alpha and beta subunits.* Eur J Biochem, **1988**. 174(1): 207-212.

57. Philippot L and Hojberg O. *Dissimilatory nitrate reductases in bacteria.* Biochim Biophys Acta, **1999**. 1446(1-2): 1-23.

58. Hettmann T, Anemuller S, Borcherding H, Mathe L, Steinrucke P, and Diekmann S. *Pseudomonas stutzeri soluble nitrate reductase alphabeta-subunit is a soluble enzyme with a similar electronic structure at the active site as the inner membrane-bound alphabetagamma holoenzyme.* FEBS Lett, **2003**. 534(1-3): 143-50.

59. Jormakka M, Richardson D, Byrne B, and Iwata S. *Architecture of NarGH reveals a structural classification of Mo-bisMGD enzymes.* Structure (Camb), **2004**. 12(1): 95-104.

60. Bertero M, Rothery R, Palak M, Hou C, Lim D, Blasco F, Weiner J, and Strynadka N. *Insights into the respiratory electron transfer pathway from the structure of nitrate reductase A.* Nat Struct Biol, **2003**. 10(9): 681-7.

61. Moura JJ, Brondino CD, Trincao J, and Romao MJ. *Mo and W bis-MGD enzymes: nitrate reductases and formate dehydrogenases.* J Biol Inorg Chem, **2004**. 9(7): 791-9.

62. Volbeda A, Charon MH, Piras C, Hatchikian EC, Frey M, and Fontecilla-Camps JC. *Crystal structure of the nickel-iron hydrogenase from Desulfovibrio gigas.* Nature, **1995**. 373(6515): 580-7.

63. George GN, Bray RC, Morpeth FF, and Boxer DH. *Complexes with halide and other anions of the molybdenum centre of nitrate reductase from Escherichia coli.* Biochem J, **1985**. 227(3): 925-31.

64. Magalon A, Asso M, Guigliarelli B, Rothery RA, Bertrand P, Giordano G, and Blasco F. *Molybdenum cofactor properties and [Fe-S] cluster coordination in Escherichia coli nitrate reductase A: investigation by site-directed mutagenesis of the conserved his-50 residue in the NarG subunit.* Biochemistry, **1998**. 37(20): 7363-70.

65. Blasco F, Guigliarelli B, Magalon A, Asso M, Giordano G, and Rothery RA. *The coordination and function of the redox centres of the membrane-bound nitrate reductases.* Cell Mol Life Sci, **2001**. 58(2): 179-93.

66. Guigliarelli B, Asso M, More C, Augier V, Blasco F, Pommier J, Giordano G, and Bertrand P. *EPR and redox characterization of iron-sulfur centers in nitrate reductases A and Z from Escherichia coli. Evidence for a high-potential and a low-potential class and their relevance in the electron-transfer mechanism.* Eur J Biochem, **1992**. 207(1): 61-68.

67. Rothery R, Bertero M, Cammack R, Palak M, Blasco F, Strynadka N, and Weiner J. *The catalytic subunit of Escherichia coli nitrate reductase A contains a novel [4Fe-4S] cluster with a high-spin ground state.* Biochemistry, **2004**. 43(18): 5324-33.

68. Blasco F, Dos Santos J, Magalon A, Frixon C, Guigliarelli B, Santini C, and Giordano G. *NarJ is a specific chaperone required for molybdenum cofactor assembly in nitrate reductase A of Escherichia coli.* Mol Microbiol, **1998**. 28(3): 435-47.

69. Bachmann B. *Linkage map of Escherichia coli K-12, edition 8.* Microbiol Mol Biol Rev, **1990**. 54(2): 130-97.

70. Chiang RC, Cavicchioli R, and Gunsalus RP. *'Locked-on' and 'locked-off' signal transduction mutations in the periplasmic domain of the Escherichia coli NarQ and*

NarX sensors affect nitrate- and nitrite-dependent regulation by NarL and NarP. Mol Microbiol, **1997**. 24(5): 1049-60.

71. Darwin AJ and Stewart V. *Nitrate and nitrite regulation of the Fnr-dependent aeg-46.5 promoter of Escherichia coli K-12 is mediated by competition between homologous response regulators (NarL and NarP) for a common DNA-binding site.* J Mol Biol, **1995**. 251(1): 15-29.
72. Darwin AJ and Stewart V. *Expression of the narX, narL, narP, and narQ genes of Escherichia coli K-12: regulation of the regulators.* J Bacteriol, **1995**. 177(13): 3865-3869.
73. Darwin AJ, Tyson KL, Busby SJ, and Stewart V. *Differential regulation by the homologous response regulators NarL and NarP of Escherichia coli K-12 depends on DNA binding site arrangement.* Mol Microbiol, **1997**. 25(3): 583-95.
74. Tyson KL, Cole JA, and Busby SJ. *Nitrite and nitrate regulation at the promoters of two Escherichia coli operons encoding nitrite reductase: identification of common target heptamers for both NarP- and NarL-dependent regulation.* Mol Microbiol, **1994**. 13(6): 1045-55.
75. Wood NJ, Alizadeh T, Bennett S, Pearce J, Ferguson SJ, Richardson DJ, and Moir JWB. *Maximal Expression of Membrane-Bound Nitrate Reductase in Paracoccus Is Induced by Nitrate via a Third FNR-Like Regulator Named NarR.* J Bacteriol, **2001**. 183(12): 3606-3613.
76. Wood NJ, Alizadeh T, Richardson DJ, Ferguson SJ, and Moir JW. *Two domains of a dual-function NarK protein are required for nitrate uptake, the first step of denitrification in Paracoccus pantotrophus.* Mol Microbiol, **2002**. 44(1): 157-70.
77. Jormakka M, Byrne B, and Iwata S. *Protonmotive force generation by a redox loop mechanism.* FEBS Lett, **2003**. 545(1): 25-30.

78. Dias J, Bursakov S, Carneiro C, Moura J, Moura I, and Romao M. *Crystallization and preliminary x-ray analysis of a nitrate reductase from Desulfovibrio desulfuricans ATCC 27774.* Acta Crystallogr D Biol Crystallogr, **1999**. 55 (Pt 4): 877-9.

79. Dias JM, Than ME, Humm A, Huber R, Bourenkov GP, Bartunik HD, Bursakov S, Calvete J, Caldeira J, Carneiro C, Moura JJ, Moura I, and Romao MJ. *Crystal structure of the first dissimilatory nitrate reductase at 1.9 A solved by MAD methods.* Structure Fold Des, **1999**. 7(1): 65-79.

80. Reyes F, Roldan M, Klipp W, Castillo F, and Moreno-Vivian C. *Isolation of periplasmic nitrate reductase genes from Rhodobacter sphaeroides DSM 158: structural and functional differences among prokaryotic nitrate reductases.* Mol Microbiol, **1996**. 19(6): 1307-18.

81. Berks B, Richardson D, Robinson C, Reilly A, Aplin R, and Ferguson S. *Purification and characterization of the periplasmic nitrate reductase from Thiosphaera pantotropha.* Eur J Biochem, **1994**. 220(1): 117-124.

82. Bell L, Richardson D, and Ferguson S. *Periplasmic and membrane-bound respiratory nitrate reductases in Thiosphaera pantotropha. The periplasmic enzyme catalyzes the first step in aerobic denitrification.* FEBS Lett, **1990**. 265(1-2): 85-7.

83. Arnoux P, Sabaty M, Alric J, Frangioni B, Guigliarelli B, Adriano J, and Pignol D. *Structural and redox plasticity in the heterodimeric periplasmic nitrate reductase.* Nat Struct Biol, **2003**. 10(11): 928-34.

84. Pignol D, Adriano J, Fontecilla-Camps J, and Sabaty M. *Crystallization and preliminary X-ray analysis of the periplasmic nitrate reductase (NapA-NapB complex) from Rhodobacter sphaeroides f. sp. denitrificans.* Acta Crystallogr D Biol Crystallogr, **2001**. 57(Pt 12): 1900-2.

85. Hettmann T, Siddiqui R, von Langen J, Frey C, Romao M, and Diekmann S. *Mutagenesis study on the role of a lysine residue highly conserved in formate*

dehydrogenases and periplasmic nitrate reductases. Biochem Biophys Res Commun, **2003**. 310(1): 40-7.

86. Hettmann T, Siddiqui R, Frey C, Santos-Silva T, Romao M, and Diekmann S. *Mutagenesis study on amino acids around the molybdenum centre of the periplasmic nitrate reductase from Ralstonia eutropha.* Biochem Biophys Res Commun, **2004**. 320(4): 1211-9.
87. Brige A, Leys D, Meyer T, Cusanovich M, and Van Beeumen J. *The 1.25 A resolution structure of the diheme NapB subunit of soluble nitrate reductase reveals a novel cytochrome c fold with a stacked heme arrangement.* Biochemistry, **2002**. 41(15): 4827-36.
88. Butler C, Fairhurst S, Ferguson S, Thomson A, Berks B, Richardson D, and Lowe D. *Mo(V) co-ordination in the periplasmic nitrate reductase from Paracoccus pantotrophus probed by electron nuclear double resonance (ENDOR) spectroscopy.* Biochem J, **2002**. 363(Pt 3): 817-23.
89. Butler C, Charnock J, Garner C, Thomson A, Ferguson S, Berks B, and Richardson D. *Thiocyanate binding to the molybdenum centre of the periplasmic nitrate reductase from Paracoccus pantotrophus.* Biochem J, **2000**. 352 Pt 3: 859-64.
90. Butler C, Charnock J, Bennett B, Sears H, Reilly A, Ferguson S, Garner C, Lowe D, Thomson A, Berks B, and Richardson D. *Models for molybdenum coordination during the catalytic cycle of periplasmic nitrate reductase from Paracoccus denitrificans derived from EPR and EXAFS spectroscopy.* Biochemistry, **1999**. 38(28): 9000-12.
91. Bennett B, Charnock J, Sears H, Berks B, Thomson A, Ferguson S, Garner C, and Richardson D. *Structural investigation of the molybdenum site of the periplasmic nitrate reductase from Thiosphaera pantotropha by X-ray absorption spectroscopy.* Biochem J, **1996**. 317 (Pt 2): 557-63.

92. Bennett B, Berks B, Ferguson S, Thomson A, and Richardson D. *Mo(V) electron paramagnetic resonance signals from the periplasmic nitrate reductase of Thiosphaera pantotropha.* Eur J Biochem, **1994**. 226(3): 789-798.

93. Gonzalez PJ, Rivas MG, Brondino CD, Bursakov SA, Moura I, and Moura JJ. *EPR and redox properties of periplasmic nitrate reductase from Desulfovibrio desulfuricans ATCC 27774.* J Biol Inorg Chem, **2006**. 11(5): 609-16.

94. Bursakov S, Liu M, Payne W, LeGall J, Moura I, and Moura J. *Isolation and preliminary characterization of a soluble nitrate reductase from the sulfate reducing organism Desulfovibrio desulfuricans ATCC 27774.* Anaerobe, **1995**. 1(1): 55-60.

95. Delgado MJ, Bonnard N, Tresierra-Ayala A, Bedmar EJ, and Muller P. *The Bradyrhizobium japonicum napEDABC genes encoding the periplasmic nitrate reductase are essential for nitrate respiration.* Microbiology, **2003**. 149(12): 3395-3403.

96. Flanagan D, Gregory L, Carter J, Karakas-Sen A, Richardson D, and Spiro S. *Detection of genes for periplasmic nitrate reductase in nitrate respiring bacteria and in community DNA.* FEMS Microbiol Lett, **1999**. 177(2): 263-70.

97. Berks B, Richardson D, Reilly A, Willis A, and Ferguson S. *The napEDABC gene cluster encoding the periplasmic nitrate reductase system of Thiosphaera pantotropha.* Biochem J, **1995**. 309 (Pt 3): 983-92.

98. Bedzyk L, Wang T, and Ye RW. *The Periplasmic Nitrate Reductase in Pseudomonas sp. Strain G-179 Catalyzes the First Step of Denitrification.* J Bacteriol, **1999**. 181(9): 2802-2806.

99. Grove J, Tanapongpipat S, Thomas G, Griffiths L, Crooke H, and Cole J. *Escherichia coli K-12 genes essential for the synthesis of c-type cytochromes and a third nitrate reductase located in the periplasm.* Mol Microbiol, **1996**. 19(3): 467-81.

100. Thomas G, Potter L, and Cole J. *The periplasmic nitrate reductase from Escherichia coli: a heterodimeric molybdoprotein with a double-arginine signal sequence and an unusual leader peptide cleavage site.* FEMS Microbiol Lett, **1999**. 174(1): 167-71.

101. Pugsley AP. *The complete general secretory pathway in gram-negative bacteria.* Microbiol Rev, **1993**. 57(1): 50-108.

102. Roldan MD, Sears HJ, Cheesman MR, Ferguson SJ, Thomson AJ, Berks BC, and Richardson DJ. *Spectroscopic Characterization of a Novel Multiheme c-Type Cytochrome Widely Implicated in Bacterial Electron Transport.* J Biol Chem, **1998**. 273(44): 28785-28790.

103. Cartron M, Roldan M, Ferguson S, Berks B, and Richardson D. *Identification of two domains and distal histidine ligands to the four haems in the bacterial c-type cytochrome NapC; the prototype connector between quinol/quinone and periplasmic oxido-reductases.* Biochem J, **2002**. 368(Pt 2): 425-32.

104. Zajicek RS, Allen JW, Cartron ML, Richardson DJ, and Ferguson SJ. *Paracoccus pantotrophus NapC can reductively activate cytochrome cd1 nitrite reductase.* FEBS Lett, **2004**. 565(1-3): 48-52.

105. Brondijk T, Fiegen D, Richardson D, and Cole J. *Roles of NapF, NapG and NapH, subunits of the Escherichia coli periplasmic nitrate reductase, in ubiquinol oxidation.* Mol Microbiol, **2002**. 44(1): 245-55.

106. Brondijk T, Nilavongse A, Filenko N, Richardson D, and Cole J. *NapGH components of the periplasmic nitrate reductase of Escherichia coli K-12: location, topology and physiological roles in quinol oxidation and redox balancing.* Biochem J, **2004**. 379(Pt 1): 47-55.

107. Ilbert M, Mejean V, and Iobbi-Nivol C. *Functional and structural analysis of members of the TorD family, a large chaperone family dedicated to molybdoproteins.* Microbiology, **2004**. 150(4): 935-943.

108. Olmo-Mira MF, Gavira M, Richardson DJ, Castillo F, Moreno-Vivian C, and Roldan MD. *NapF Is a Cytoplasmic Iron-Sulfur Protein Required for Fe-S Cluster Assembly in the Periplasmic Nitrate Reductase.* J Biol Chem, **2004**. 279(48): 49727-49735.

109. Wang H, Tseng C-P, and Gunsalus RP. *The napF and narG Nitrate Reductase Operons in Escherichia coli Are Differentially Expressed in Response to Submicromolar Concentrations of Nitrate but Not Nitrite.* J Bacteriol, **1999**. 181(17): 5303-5308.

110. Potter L, Millington P, Thomas G, Rothery R, Giordano G, and Cole J. *Novel growth characteristics and high rates of nitrate reduction of an Escherichia coli strain, LCB2048, that expresses only a periplasmic nitrate reductase.* FEMS Microbiol Lett, **2000**. 185(1): 51-7.

111. Darwin AJ, Ziegelhoffer EC, Kiley PJ, and Stewart V. *Fnr, NarP, and NarL Regulation of Escherichia coli K-12 napF (Periplasmic Nitrate Reductase) Operon Transcription In Vitro.* J Bacteriol, **1998**. 180(16): 4192-4198.

112. Stewart V, Lu Y, and Darwin AJ. *Periplasmic Nitrate Reductase (NapABC Enzyme) Supports Anaerobic Respiration by Escherichia coli K-12.* J Bacteriol, **2002**. 184(5): 1314-1323.

113. Stewart V, Bledsoe PJ, and Williams SB. *Dual Overlapping Promoters Control napF (Periplasmic Nitrate Reductase) Operon Expression in Escherichia coli K-12.* J Bacteriol, **2003**. 185(19): 5862-5870.

114. Potter L, Millington P, Griffiths L, Thomas G, and Cole J. *Competition between Escherichia coli strains expressing either a periplasmic or a membrane-bound nitrate reductase: does Nap confer a selective advantage during nitrate-limited growth?* Biochem J, **1999**. 344 Pt 1: 77-84.

115. Bedmar E, Robles E, and Delgado M. *The complete denitrification pathway of the symbiotic, nitrogen-fixing bacterium Bradyrhizobium japonicum.* Biochem Soc Trans, **2005**. 33(Pt 1): 141-4.

116. Berks BC, Page MD, Richardson DJ, Reilly A, Cavill A, Outen F, and Ferguson SJ. *Sequence analysis of subunits of the membrane-bound nitrate reductase from a denitrifying bacterium: the integral membrane subunit provides a prototype for the dihaem electron-carrying arm of a redox loop.* Mol Microbiol, **1995**. 15(2): 319-31.

117. Liu H, Takio S, Satoh T, and Yamamoto I. *Involvement in denitrification of the napKEFDABC genes encoding the periplasmic nitrate reductase system in the denitrifying phototrophic bacterium Rhodobacter sphaeroides f. sp. denitrificans.* Biosci Biotechnol Biochem, **1999**. 63(3): 530-6.

118. Sears HJ, Sawers G, Berks BC, Ferguson SJ, and Richardson DJ. *Control of periplasmic nitrate reductase gene expression (napEDABC) from Paracoccus pantotrophus in response to oxygen and carbon substrates.* Microbiology, **2000**. 146(11): 2977-2985.

119. Gavira M, Roldan MD, Castillo F, and Moreno-Vivian C. *Regulation of nap Gene Expression and Periplasmic Nitrate Reductase Activity in the Phototrophic Bacterium Rhodobacter sphaeroides DSM158.* J Bacteriol, **2002**. 184(6): 1693-1702.

120. Ellington MJK, Bhakoo KK, Sawers G, Richardson DJ, and Ferguson SJ. *Hierarchy of Carbon Source Selection in Paracoccus pantotrophus: Strict Correlation between Reduction State of the Carbon Substrate and Aerobic Expression of the nap Operon.* J Bacteriol, **2002**. 184(17): 4767-4774.

121. Ellington MJK, Sawers G, Sears HJ, Spiro S, Richardson DJ, and Ferguson SJ. *Characterization of the expression and activity of the periplasmic nitrate reductase of Paracoccus pantotrophus in chemostat cultures.* Microbiology, **2003**. 149(6): 1533-1540.

122. Ellington MJK, Richardson DJ, and Ferguson SJ. *Rhodobacter capsulatus gains a competitive advantage from respiratory nitrate reduction during light-dark transitions.* Microbiology, **2003**. 149(4): 941-948.

123. Simon J, Sanger M, Schuster S, and Gross R. *Electron transport to periplasmic nitrate reductase (NapA) of Wolinella succinogenes is independent of a NapC protein.* Mol Microbiol, **2003**. 49(1): 69-79.

124. Jepson BJN, Anderson LJ, Rubio LM, Taylor CJ, Butler CS, Flores E, Herrero A, Butt JN, and Richardson DJ. *Tuning a Nitrate Reductase for Function: The First Spectropotentiometric Characterization of a Bacterial Assimilatory Nitrate Reductase Reveals Novel Redox Properties.* J Biol Chem, **2004**. 279(31): 32212-32218.

125. Cosper MM, Neese F, Astashkin AV, Carducci MD, Raitsimring AM, and Enemark JH. *Determination of the g-tensors and their orientations for cis,trans-(L-N2S2)Mo(V)OX (X = Cl, SCH2Ph) by single-crystal EPR spectroscopy and molecular orbital calculations.* Inorg Chem, **2005**. 44(5): 1290-301.

126. Palmer G. *Electron Paramagnetic Resonance of Metalloproteins*. Physical Methods in Bioinorganic and Magnetism, ed. L Que. **2000**, Sausalito, CA: University Science Books. 121-186.

127. Wertz JE and Bolton JR. *Electron Spin Resonance: Elementary Theory and Practical Applications*, ed. J Wiley and sons. **1994**, New York.

128. Pilbrow J. *Transition Ion Electron Paramagnetic Resonance*. **1990**, Oxford: Clarendon Press.

129. Liu MC and Peck HD, Jr. *The isolation of a hexaheme cytochrome from Desulfovibrio desulfuricans and its identification as a new type of nitrite reductase.* J Biol Chem, **1981**. 256(24): 13159-13164.

130. Bursakov S, Carneiro C, Almendra M, Duarte R, Caldeira J, Moura I, and Moura J. *Enzymatic properties and effect of ionic strength on periplasmic nitrate reductase (NAP) from Desulfovibrio desulfuricans ATCC 27774.* Biochem Biophys Res Commun, **1997**. 239(3): 816-22.

131. Leslie AGW. *Recent changes to the MOSFLM package for processing film and image plate data.* Joint CCP4+ESF-EAMCB Newsletter on Protein Crystallography, **1992**. 26.

132. Kabsch W. *Evaluation of single-crystal X-ray diffraction data from a position-sensitive detector.* J Appl Cryst, **1988**. 21: 916-924.

133. Murshudov GN, Vagin AA, and Dodson EJ. *Refinement of macromolecular structures by the maximum-likelihood method.* Acta Crystallogr D Biol Crystallogr, **1997**. 53(Pt 3): 240-255.

134. Jones TA, Zou JY, Cowan SW, and Kjeldgaard M. *Improved methods for building protein models in electron density maps and the location of errors in these models.* Acta Crystallogr A, **1991**. 47(Pt 2): 110-119.

135. Emsley P and Cowtan K. *Coot: model-building tools for molecular graphics.* Acta Crystallogr D Biol Crystallogr, **2004**. 60(Pt 12 Pt 1): 2126-2132.

136. Bastian NR, Kay CJ, Barber MJ, and Rajagopalan KV. *Spectroscopic Studies of the Molybdenum-containing Dimethyl Sulfoxide Reductase from Rhodobacter sphaeroides f. sp. denitrificans.* J Biol Chem, **1991**. 266(1): 45-51.

137. Costa C, Teixeira, M., LeGall, J., Moura, J.J.G. and Moura, I. *Formate dehydrogenase from Desulfovibrio desulfuricans ATCC 27774: Isolation and spectroscopic characterization of the active sites (heme, iron-sulfur centers and molybdenum).* J Biol Inorg Chem, **1997**. 2: 198-208.

138. Barber MJ, Siegel LM, Schauer NL, May HD, and Ferry JG. *Formate dehydrogenase from Methanobacterium formicicum. Electron paramagnetic resonance spectroscopy of the molybdenum and iron-sulfur centers.* J Biol Chem, **1983**. 258(18): 10839-10845.

139. George GNC, C.; Moura, J. J. G.; Moura, I. *Observation of Ligand-Based Redox Chemistry at the Active Site of a Molybdenum Enzyme.* J Am Chem Soc, **1999**. 121(11): 2625-2626.

140. Khangulov SV, Gladyshev VN, Dismukes GC, and Stadtman TC. *Selenium-containing formate dehydrogenase H from Escherichia coli: a molybdopterin enzyme that catalyzes formate oxidation without oxygen transfer.* Biochemistry, **1998**. 37(10): 3518-28.

141. Frangioni B, Arnoux P, Sabaty M, Pignol D, Bertrand P, Guigliarelli B, and Leger C. *In Rhodobacter sphaeroides respiratory nitrate reductase, the kinetics of substrate binding favors intramolecular electron transfer.* J Am Chem Soc, **2004**. 126(5): 1328-9.

142. Field SJ, Thornton NP, Anderson LJ, Gates AJ, Reilly A, Jepson BJ, Richardson DJ, George SJ, Cheesman MR, and Butt JN. *Reductive activation of nitrate reductases.* Dalton Trans, **2005**(21): 3580-6.

143. Boyington JC, Gladyshev VN, Khangulov SV, Stadtman TC, and Sun PD. *Crystal Structure of Formate Dehydrogenase H: Catalysis Involving Mo, Molybdopterin, Selenocysteine, and an Fe4S4 Cluster.* Science, **1997**. 275(5304): 1305-1308.

144. Leopoldini M, Russo N, Toscano M, Dulak M, and Wesolowski TA. *Mechanism of nitrate reduction by Desulfovibrio desulfuricans nitrate reductase--a theoretical investigation.* Chemistry, **2006**. 12(9): 2532-41.

145. Raaijmakers H, and Romao MJ. *Formate-reduced E. coli formate dehydrogenase H: the reinterpretation of the crystal structure suggests a new reaction mechanism.* J Biol Inorg Chem, **2006**. 11(7): 849-854.

146. Raaijmakers H, Macieira S, Dias JM, Teixeira S, Bursakov S, Huber R, Moura JJ, Moura I, and Romao MJ. *Gene sequence and the 1.8 A crystal structure of the tungsten-containing formate dehydrogenase from Desulfovibrio gigas.* Structure (Camb), **2002**. 10(9): 1261-72.